



Jürgen Baumgartner, BSc

MCF in-silico: modelling of the potassium current in human breast cancer cells

MASTER'S THESIS

to achieve the university degree of

Diplom-Ingenieur

Master's degree programme: Biomedical Engineering

submitted to

Graz University of Technology

Supervisor

Univ.-Prof. Dipl.-Ing. Dr.techn. Christian Baumgartner

Institute of Health Care Engineering with European Testing Center of Medical Devices

Second Supervisor

Dipl.-Ing. Dr.techn. Sonja Langthaler BSc

Graz, December 2022

EIDESSTATTLICHE ERKLÄRUNG

AFFIDAVIT

Ich erkläre an Eides statt, dass ich die vorliegende Arbeit selbstständig verfasst, andere als die angegebenen Quellen/Hilfsmittel nicht benutzt, und die den benutzten Quellen wörtlich und inhaltlich entnommenen Stellen als solche kenntlich gemacht habe. Das in TUGRAZonline hochgeladene Textdokument ist mit der vorliegenden Masterarbeit/Diplomarbeit/Dissertation identisch.

I declare that I have authored this thesis independently, that I have not used other than the declared sources/resources, and that I have explicitly indicated all material which has been quoted either literally or by content from the sources used. The text document uploaded to TUGRAZonline is identical to the present master's thesis/diploma thesis/doctoral dissertation.

Datum / Date

Unterschrift / Signature

Die Technische Universität Graz übernimmt mit der Betreuung und Bewertung einer Masterarbeit keine Haftung für die erarbeiteten Ergebnisse: Eine positive Bewertung und Anerkennung (Approbation) einer Arbeit bescheinigt nicht notwendigerweise die vollständige Richtigkeit der Ergebnisse.

MCF in-silico: Modellierung des Kaliumstroms in menschlichen Brustkrebszellen

Krebs ist eine komplexe Krankheit, an der umfangreich geforscht wird. Eine Vielzahl an Studien berichtete über Zusammenhänge zwischen den elektrophysiologischen Eigenschaften von Krebszellen und der Entstehung und dem Verlauf dieser Krankheit. Markov Modelle können für die in-silico Modellierung von Ionenkanälen verwendet werden und erst kürzlich wurde der Ionenstrom einer ganzen Krebszelle mit diesem Modellierungsansatz abgebildet. In diesem Zusammenhang wurde die maligne Brustkrebszelllinie MCF-7 im Rahmen dieser Arbeit behandelt. Basierend auf dem aktuellen Wissensstand hinsichtlich der Expression spannungsgesteuerter Kaliumkanäle in den Zelllinien MCF-7 und MCF-10A, wurden erste Ansätze zur Modellierung der Einzelkanalströme, sowie der gesamten Ionenströme in diesen Zellen entwickelt.

Schlüsselwörter: Brustkrebs, Elektrophysiologie, Ionenkanäle, Modellierung, in-silico.

MCF in-silico: modelling of the potassium current in human breast cancer cells

Cancer is known to be a complex disease on which comprehensive research is carried out. Various studies reported correlations between electrophysiological properties of cancer cells and cancer development and progression. Markov Models can be used for in-silico modelling of ion channels and just recently, the ionic current of a whole cancer cell was replicated using this particular modelling approach. In this context, the malign breast cancer cell line MCF-7 was addressed in this thesis. Based on current knowledge on expression of voltage-gated potassium channels in MCF-7 and MCF-10A, first approaches were developed for modelling the single channel currents, as well as the whole-cell currents in these cell lines.

Key words: breast cancer, electrophysiology, ion channels, modelling, in-silico.

Contents

Abstract	iv
Abbreviations and Foreword	xi
1 Introduction	1
1.1 Cell Biology	1
1.1.1 The Cell	1
1.1.2 The Cell Membrane	2
1.1.3 Transmembrane Transport Mechanisms	3
1.1.4 Proliferation and Cell Cycle	4
1.1.5 Differentiation and Expression Profile	4
1.2 Cell Biophysics	5
1.2.1 Electrical Membrane Model	5
1.2.2 The Membrane Potential	6
1.2.3 The Nernst Potential	7
1.2.4 The Goldman-Hodgkin-Katz Equation	9
1.2.5 The Resting Membrane Potential	10
1.2.6 The Reversal Potential	11
1.3 Ion Channels	11
1.3.1 Classification of Ion Channels	12
1.3.2 Potassium Channels	14
1.3.3 Ion Channels and Proliferation	16
1.4 Cellular Electrophysiology	18
1.4.1 Patch-clamp Technique	18
1.4.2 Voltage- and Current-clamp Technique	21
1.5 Cancer and Cancer Electrophysiology	22
1.5.1 Terminology and Definitions	22
1.5.2 Benign and Malign Neoplasms	24
1.5.3 Development of Cancer	24

Contents

1.5.4	Classification of Cancer	25
1.5.5	Hallmarks of Cancer	26
1.5.6	Breast Cancer	28
1.5.7	Breast Cancer Cell Lines	28
1.5.8	Ion Channels in Cancer	30
1.5.9	Electrophysiological Characteristics of MCF-7	32
2	Problem Definition	37
3	Methods	38
3.1	Experimental Data	39
3.1.1	Data Preprocessing	40
3.1.2	Voltage Pulse Protocol	41
3.2	Ion Channel Modelling	42
3.2.1	Hidden Markov Model Approach	43
3.2.2	Channel Modelling and Implementation	44
3.2.3	Cell Modelling	49
3.2.4	Gating Analysis	55
3.3	Kinetic Models of K_V -channels	55
3.3.1	Kinetic Model of $K_{V1.1}$	56
3.3.2	Kinetic Model of $K_{V1.2}$	57
3.3.3	Kinetic Model of $K_{V1.3}$	59
3.3.4	Kinetic Model of $K_{V1.5}$	59
3.3.5	Kinetic Model of $K_{V7.1}$	60
3.3.6	Kinetic Model of $K_{V10.1}$	61
3.3.7	Kinetic Model of $K_{V11.1}$	62
4	Results	64
4.1	K_V -Channels in MCF-7 and MCF-10A	64
4.2	Single Channel Simulations	68
4.3	Comparison of Modelling Approaches	72
4.4	Experimental Data	72
4.5	Gating Analysis	76
4.6	Optimization Results	78
5	Discussion	85
5.1	Channel Expression	85

Contents

5.2	Modelling Approach	86
5.3	Single Channel Models	88
5.4	Experimental Data	89
5.5	Gating Analysis	91
5.6	Cell Models	93
6	Conclusion	95
	Bibliography	97
7	Appendix	107
7.1	Voltage Pulse Protocol	107
7.2	Further Ion Channels in MCF-7	107
7.2.1	Potassium Channels	107
7.2.2	Sodium Channels	109
7.2.3	Calcium Channels	109
7.2.4	Others	110

List of Figures

1	Electrical membrane model	6
2	Voltage-gated superfamily [11]	13
3	Topologies of K^+ -channels [14]	14
4	K^+ conductivity and V_m over the cell cycle adapted from [21]	17
5	Overview of patch-clamp configurations [25]	18
6	Equivalent circuit of the whole-cell configuration adapted from [26]	20
7	Hallmarks of cancer [29]	26
8	Equivalence of breast cancer subtypes [33]	29
9	Ion channel expression and carcinogenesis [17]	31
10	Roles of ion channels in cancer [17]	32
11	Membrane potential distribution in MCF-7 colony [41]	33
12	V_m over cell cycle phases in MCF-7 [44]	34
13	Whole-cell patch-clamp measurement of MCF-7 cell [48]	36
14	Whole-cell patch-clamp measurement of MCF-10A cell [50]	36
15	Workflow of cell modelling	38
16	Clamping potentials of VPP over time	42
17	Kinetic model of $K_{V11.1}$ introduced by [57]	44
18	Signal flow diagrams of cell models	51
19	Kinetic model of $K_{V1.1}$ introduced by [65]	57
20	Kinetic model of $K_{V1.2}$ introduced by [66]	58
21	Kinetic model of $K_{V1.3}$ introduced by [70]	59
22	Kinetic model of $K_{V1.5}$ introduced by [73]	60
23	Kinetic model of $K_{V7.1}$ introduced by [75]	61
24	Kinetic model of $K_{V10.1}$ introduced by [77]	62
25	Kinetic model of $K_{V11.1}$ introduced by [57]	63
26	K_V -channel selection for cell modelling adapted from [86]	67

List of Figures

27	Simulated single channel current response of $K_{V1.1}$	68
28	Simulated single channel current response of $K_{V1.2}$	69
29	Simulated single channel current response of $K_{V1.3}$	69
30	Simulated single channel current response of $K_{V1.5}$	70
31	Simulated single channel current response of $K_{V7.1}$	70
32	Simulated single channel current response of $K_{V10.1}$	71
33	Simulated single channel current response of $K_{V11.1}$	71
34	Comparison of macroscopic current responses of $K_{V7.1}$	72
35	Experimental data of MCF-7 cell (RAW)	73
36	Experimental data of MCF-7 cell (OSC)	73
37	Experimental data of MCF-7 cell (OSC + AVG)	74
38	Experimental data of MCF-7 cell (OSC + AVG + RCP)	74
39	Experimental data of MCF-10A cell (RAW)	75
40	Experimental data of MCF-10A cell (AVG)	75
41	Experimental data of MCF-10A cell (AVG + RCP)	76
42	Gating analysis with respect to the MCF-7 model	77
43	Gating analysis with respect to the MCF-10A model	77
44	Simulated whole-cell currents of MCF-7 cell model	79
45	Current composition of MCF-7 model	80
46	Simulated whole-cell currents of MCF-10A cell model	81
47	Current composition of MCF-10A model	82
48	Simulated whole-cell currents of MCF-10A cell model (RDU)	83
49	Current composition of MCF-10A model (RDU)	84

List of Tables

1	Molecular classification of breast cancer [The Physician Assistant Student's Guide to the Clinical Year: OB-GYN quoted in 30]	28
2	Channel blockers and MCF-7 proliferation	35
3	Constraints of MCF-7 model	53
4	Constraints of MCF-10A model	53
5	Overview of single channel simulations	68
6	Optimization results of cell models	78
7	Constraints of optimizations	78
8	Timing of voltage pulse protocol	107
9	Clamping potentials of voltage pulse protocol	107

Abbreviations and Foreword

4-AP	4-Aminopyridine
ATP	Adenosine triphosphate
AVG	Averaging
BPS	British physiological society
C	Close
Ca	Calcium
CHO cell	Chinese hamster ovary cell
Cl	Chloride
DTX	Dendrotoxin
HMM	Hidden Markov Model
I	Inactivated
IUPHAR	International union of basic and clinical pharmacology
K	Potassium
mRNA	Messenger-RNA
Na	Sodium
O	Open
OSC	Offset correction
PCR	Polymerase chain reaction
PSO	Particle swarm optimization
RCP	Removal of capacitive peaks
RDU	Reduced dataset usage
RRMSE	Relative root-mean square error
RT-PCR	Reverse transcription polymerase chain reaction
RVD	Regulatory volume decrease
SSM	State-space model
TEA	Tetraethylammonium
TM	Transmembrane helices
VGPC	Voltage-gated potassium channel
VPP	Voltage pulse protocol

Throughout this thesis, an arbitrary discrete-time variable x is denoted by $x[n]$ and its continuous counterpart by $x(t)$. However, as the described and derived equations are subsequently implemented in MATLAB, the continuous-time variables will be transferred to discrete-time variables without explicitly mentioning it.

Table headers in this thesis are separated from the table bodies by two horizontal lines and can comprise one or two rows. In case the table header is composed of two rows, the top row is used for labelling the columns while the lower header row refers to the unit of each column.

For denoting concentrations with respect to the compartment they refer to, the variables c^e and c^i are introduced. Please note that e and i are used for labelling purposes only. For example, c^i refers to a concentration in the intracellular region.

In terms of modelling the current responses of ion channels, $i(t)$ refers to a single channel current and $I(t)$ refers to a macroscopic current in this thesis.

1 Introduction

1.1 Cell Biology

A short introduction to cell biology is outlined at this point. This chapter is not meant to be a complete excursion or to entirely cover all aspects in cell biology. It should provide essential information and convey important principles for the upcoming chapters.

1.1.1 The Cell

Cells are the smallest units that comprise all essential functions by which living organisms are characterized. In eukaryotes (category including multicellular organisms), cells are the basic building blocks of more complexly organized organisms. [1]

All cells in the human body share the same basic structure and can be spatially described using an inner and an outer compartment and a separating membrane [2]. This separation principle is particularly important for maintaining the cellular processes in the inner compartment [1].

The inner compartment of the cell is referred to as the intracellular space or region in this thesis. It is spatially limited by the cell membrane and filled with cytoplasm. [2]

Cytoplasm consists of the cytosol (liquid part with dissolved substances), the cytoskeleton and cell organelles [1]. Up to 85 % of the cell consists of water (solvent/suspension) [2].

Note that the terms intracellular space/region and cytoplasm are synonymously used in this thesis. The outer compartment of the cell is referred to as the extracellular space or region in this thesis [2].

1.1.2 The Cell Membrane

Human cells are delimited by membranes. The major components of these structures are proteins, phospholipids and cholesterol. The exact compositions of these components are cell specific but the fundamental structures are always the same. The phospholipids (main components) form a lipid bilayer in which the hydrophilic ends are headed towards the intra- or extracellular region, respectively (outer part). [2]

These 5 nm thick membranes are not rigid, they are flexible. This is referred to as *fluidity* of the cell membrane. Cholesterol reduces the fluidity by stabilizing the molecular structure. [2]

While fat-soluble substances can permeate, the cell membrane acts as a strong barrier for water and water-soluble substances [2]. The electric resistance of the membrane is approximately $10^{15} \Omega$ [3].

Integral and peripheral proteins are incorporated in the membrane. Many of these integral membrane proteins are channel-like pores. Others are carriers which bind substances on one side and release them on the other side of the membrane. Pumps allow substances to travel against their gradients. [2]

Plasma membrane and cell membrane are used synonymously in literature [4]. The terms *membrane*, *plasma membrane* and *cell membrane* are used interchangeably in this thesis.

1.1.3 Transmembrane Transport Mechanisms

Substances can pass the cell membrane via active transport mechanisms or by diffusion. Fat-soluble substances can pass the membrane without the need of any transporting component, just by means of diffusion. [2]

Ions pass the membrane via ion channels. These channels form pores through which ions, with respect to their electrochemical gradients, can diffuse. In this context, conformational changes of the channel protein result in opening and closing the pore. This is generally referred to as *gating*. [3]

In contrast to channels, carriers bind substances before going through a series of conformational changes, followed by releasing the substances on the other side of the membrane [3].

Carriers can be classified by symporters (same direction of multiple agents), antiporters (opposite direction of multiple agents) and uniporters (one agent at a time only). Pumps are considered to be carriers as well. [2]

ATPasen (pumps) are of great importance in cellular electrophysiology. They utilize energy harvested from hydrolysing ATP to transport agents against their electrochemical gradients. The Na^+/K^+ -ATPase is the most common one and known to partially maintain the membrane potential (approximately 5 to 10 mV). [2]

Referring to [2] and [3], transmembrane transport mechanisms can be classified as follows:

- **Pores**
 - Ion channels
 - Aquaporines
- **Carriers**
 - Uniporter/Symporter/Antiporter
 - Active transport
 - * Primary active transport (ATPasen)
 - * Secondary active transport

1.1.4 Proliferation and Cell Cycle

Cell proliferation refers to both cell growth and cell division. Many cells divide regularly, others more rarely and some cells practically do not proliferate at all. [2]

The actual cell division often takes only 30 minutes, while the rest of the time the cell is considered to be in the interphase, fulfilling its actual purpose. The mitosis (cell division) is also referred to as M-phase and consists of six sequential phases: prophase, prometaphase, metaphase, anaphase, telophase and cytokinesis. [2]

The cell cycle can be subdivided alternatively using the following scheme: G₁-phase, S-phase, G₂-phase and M-phase. By the end of the M-phase, either a quiescent state G₀ or the next G₁-phase of a new cell cycle is entered. [1]

These two sequential segmentations of the cell cycle are consistent and compatible to each other. Mitosis and M-phase are equivalent. The interphase can be subdivided into G₁-, S- and G₂-phase. While G₁ represents the growing phase, G₂ represents the preparation of the cell division. The S-phase in between is the synthesis phase in which the genetic material is duplicated. [1]

1.1.5 Differentiation and Expression Profile

A single cell possesses the ubiquitous genetic information of the whole organism but typically expresses only a small part of it. A variety of proteins are expressed equally throughout all cells (e.g. structural proteins). However, some proteins are exclusively expressed in particular cells only. These cell-specific expressions are caused by *differentiation*. [2]

Differentiation is another word for the specialization of a cell during its maturation and it is basically defined by the requirements of the organism [4]. It causes the cell to express only the essential and required proteins for its specific purpose [2]. Gene expression is tightly regulated by the cell [1].

Expression profile refers to the expressed mRNA in a cell that collectively defines its phenotype [4].

A way of determining the expression profile is to investigate the mRNA sequences which are present in a cell. The presence of a specific transcript hints the expression of the corresponding protein. [2]

As it will be shown in upcoming chapters, this was usually carried out in different studies in order to determine the expressions of specific ion channels in observed cells. In many cases, the expression of the channel protein was additionally confirmed by determining the presence of the actual protein (e.g. via Western Blot) as the presence of the corresponding mRNA transcript only hints the expression.

1.2 Cell Biophysics

In this chapter, essential biophysical mechanisms in cellular environments are introduced.

1.2.1 Electrical Membrane Model

Using the previous description from chapter 1.1.2, the fundamental structure of a cell can be interpreted as two conducting compartments, separated by a partially-conductive barrier (plasma membrane). The distribution of charge carriers (ions) in this arrangement is usually asymmetric, which is the reason of literally all electrical phenomena on a cellular level [3].

By transferring this arrangement into the electric domain, the equivalent circuit diagram of the plasma membrane can be developed as follows.

Movements of charge carriers from one compartment to the other can be interpreted as ionic currents through the plasma membrane by the rules of physics. The total membrane current corresponds with a total membrane conductance, modelled by a resistor R_m in the equivalent circuit diagram [3]. Caused by the separation and storage of charges, the model of the plasma membrane also includes a capacitance between the two compartments [5].

Due to the thin bilayer, this capacitance can reach relatively high values [6]. A realistic value of the membrane capacitance C_m among all cell types is $0.8 \mu\text{F}/\text{cm}^2$ (specific capacity) [3].

Connecting R_m and C_m in parallel results in the equivalent circuit diagram of the plasma membrane in its simplest form [3]. Figure 1 shows the equivalent circuit of the cell membrane.

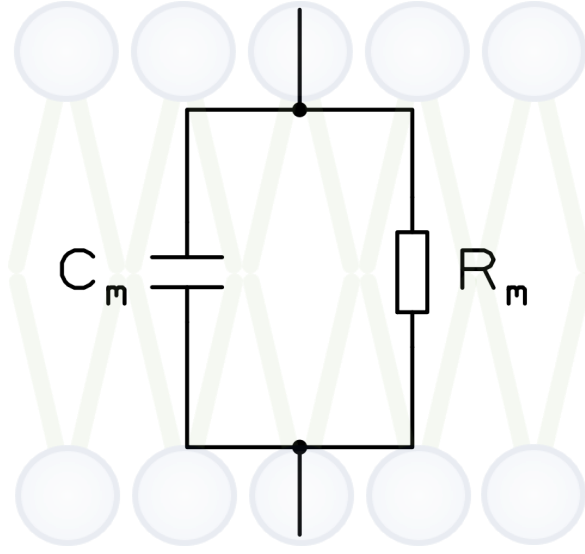


Figure 1: Electrical membrane model. R_m represents the total resistance and C_m the total capacitance of the cell membrane.

1.2.2 The Membrane Potential

As previously described, the plasma membrane separates two compartments with asymmetrically distributed charge carriers. By the rules of physics, an electric voltage results.

The membrane potential V_m can be principally defined using the potential of the intracellular region φ_i and the potential of the extracellular region φ_e [7]. Referring to [7], the conventional mathematical definition of the membrane potential V_m is shown in equation 1.

$$\boxed{V_m = \varphi_i - \varphi_e} \quad (1)$$

1.2.3 The Nernst Potential

For the description of the Nernst potential, the following initial definitions are provided.

The concentration of an ion species Ψ (e.g. Ψ refers to K^+ , Na^+ , Ca^{2+} or Cl^-) in a cellular environment is denoted by c_Ψ^i for the concentration of Ψ in the intracellular region and c_Ψ^e for the extracellular region. For each ion species Ψ , there will be a certain concentration ratio c_Ψ^i / c_Ψ^e maintained constantly by pumps and passive permeability [7].

As known from previous observations, almost all cells maintain a higher concentration of potassium in the intracellular region than in the extracellular one [8]. Equation 2 describes this circumstance mathematically.

$$c_K^i > c_K^e \Rightarrow \frac{c_K^e}{c_K^i} < 1 \quad (2)$$

A single, permeable ion species Ψ in a cellular environment and a concentration difference denoted by $c_\Psi^i \neq c_\Psi^e$ are assumed for the further description.

The concentration difference results in a *chemical gradient*, caused by the difference in chemical potentials $\mu_\Psi^i \neq \mu_\Psi^e$. A diffusion from the compartment with higher concentration to the compartment with the lower one will be the consequence. [7]

Ions also carry a charge or even multiple charges (e.g. Ca^{2+}). Based on the distribution in intra- and extracellular space, an *electric gradient* will result, caused by the potential difference $\varphi_i \neq \varphi_e$, counteracting the diffusion and the chemical equilibrium ($c_\Psi^i = c_\Psi^e$). [7]

Combining these two gradients results in an *electrochemical gradient* [7].

On a physical level, the ions feel two different forces: a diffusive force F_d , caused by the chemical gradient and an electric force F_e , caused by the electric gradient. The equilibrium is reached at the exact point in which both forces are same in size ($F_d = F_e$). [6]

As illustrated in [7], the Nernst equation for an ion species Ψ can be derived by using the electrochemical potentials $\tilde{\mu}_\Psi^i$ and $\tilde{\mu}_\Psi^e$.

With respect to [7], equation 3 shows the condition for electrochemical equilibrium, where $\tilde{\mu}_\Psi^i$ and $\tilde{\mu}_\Psi^e$ are the electrochemical potentials for intra- and extracellular region, respectively.

$$\tilde{\mu}_\Psi^i = \tilde{\mu}_\Psi^e \quad (3)$$

According to [7], equation 4 shows the Nernst equation for an ion species Ψ . The derivation of equation 4 is based on the conditional equation 3. The electric potentials for intra- and extracellular region are denoted by φ_i and φ_e , z_Ψ is the charge number of the ion species Ψ , R is the ideal gas constant, T is the temperature, F is the Faraday constant and c_Ψ^i and c_Ψ^e denote the concentrations of Ψ in the intra- and extracellular region. [7]

$$E_\Psi = \varphi_i - \varphi_e = \frac{RT}{z_\Psi F} \cdot \ln \frac{c_\Psi^e}{c_\Psi^i} \quad (4)$$

With respect to equation 4, the Nernst equation is used for calculating the Nernst potential E_Ψ of a distinct, specific ion species Ψ in a cellular environment. It is the exact membrane potential in electrochemical equilibrium when Ψ is the only permeable ion species [7]. As soon as the electrochemical equilibrium is reached, there will be no net flux of ions any more [6].

The concentration difference of potassium, outlined at the beginning of this chapter, is considered for an example now. Mammalian muscles were shown to maintain the following potassium concentrations: $c_K^i = 155mM$ and $c_K^e = 4mM$ [3]. Using equation 4, the Nernst potential of potassium E_K at $T = 20^\circ C$ can be calculated as follows.

$$E_K = \frac{R \cdot T}{z_K \cdot F} \cdot \ln \frac{c_K^e}{c_K^i} \approx \frac{8.314 \frac{J}{mol \cdot K} \cdot 293.15K}{1 \cdot 9.649 \cdot 10^4 \frac{C}{mol}} \cdot \ln \frac{4mM}{155mM} \approx \underline{\underline{-92.4mV}}$$

The concentration quotient defines both quantitative outcome and sign of the Nernst potential. As shown in equation 2, the condition $c_K^e/c_K^i < 1$ holds for potassium, resulting in a negative sign of E_K in general.

1.2.4 The Goldman-Hodgkin-Katz Equation

In the previous chapter, a single ion species was assumed of being exclusively permeable (Nernst equation). This does not reflect reality as the membrane is actually permeable for a variety of different ions [7]. Each ion species Ψ has its own specific concentration ratio c_Ψ^i/c_Ψ^e , resulting in different Nernst potentials [7]. It is obvious that the system won't settle at the exact Nernst potential of one single ion species. Based on the fact that each ion species has its own electrochemical equilibrium, the overall system settles in a steady state, governed by the balance of ionic fluxes [6]. The membrane potential V_m in steady state is located between the individual Nernst potentials of the ions [7].

Fundamentally, the total current over the membrane is considered to be zero in steady state [3]. A model has to be used for deriving an equation as the membrane potential is not thermodynamically defined in this case [7].

The Nernst-Planck equation is the starting equation for deriving the membrane potential V_m in steady state [7]. Referring to [7], the Nernst-Planck equation is shown in equation 5, where ϕ_Ψ is the electric potential in the membrane, D_Ψ is the diffusion coefficient, c_Ψ is the concentration of Ψ in the membrane and x is a distance. Other used variables were already explained in previous equations. Please see [7] for a more detailed description.

$$\phi_\Psi = -D_\Psi \cdot \left(\frac{dc_\Psi}{dx} + z_\Psi \cdot c_\Psi \cdot \frac{F}{RT} \cdot \frac{d\phi}{dx} \right) \quad (5)$$

In order to solve the Nernst-Planck equation, a series of assumptions needs to be introduced [3], [7], [9]. The diffusion coefficient and the electric field in the membrane are assumed to be constant and the ionic fluxes are assumed to be independent [3].

Solving the Nernst-Planck equation under the given assumptions results in the Goldman-Hodgkin-Katz equation [7]. For a detailed derivation please see the concerning chapters in the textbooks [3] or [7].

Referring to [7], equation 6 shows the Goldman-Hodgkin-Katz equation in case the membrane is permeable for K^+ , Na^+ and Cl^- . P_{K^+} , P_{Na^+} and P_{Cl^-} are the permeability coefficients of K^+ , Na^+ and Cl^- , respectively [7].

$$V_m = \varphi_i - \varphi_e = \frac{RT}{F} \cdot \ln \frac{P_{K^+} \cdot c_{K^+}^e + P_{Na^+} \cdot c_{Na^+}^e + P_{Cl^-} \cdot c_{Cl^-}^i}{P_{K^+} \cdot c_{K^+}^i + P_{Na^+} \cdot c_{Na^+}^i + P_{Cl^-} \cdot c_{Cl^-}^e} \quad (6)$$

With respect to [7], equation 7 shows the Goldman-Hodgkin-Katz equation in a more general form for ions with charge numbers of $z = \pm 1$.

$$V_m = \frac{RT}{F} \cdot \ln \frac{\sum_n P_{n^+} \cdot c_n^e + \sum_m P_{m^-} \cdot c_m^i}{\sum_n P_{n^+} \cdot c_n^i + \sum_m P_{m^-} \cdot c_m^e} \quad (7)$$

As it was explained and illustrated, charged carriers are still moving through the membrane in steady state but the system is balanced regarding its charge separation, resulting in a quasi-constant membrane potential [6].

1.2.5 The Resting Membrane Potential

Denoted by V_{rm} in this thesis, the resting membrane potential is directly linked to potassium in many cells [2]. As mentioned in chapter 1.2.3, the cell principally maintains a specific concentration gradient for each ion species [7]. V_{rm} can be estimated using equation 6 or 7 [6], [7].

Many cells maintain a resting membrane potential near the Nernst potential of potassium E_K . In many epithelial cells, the potassium resting conductivity is governed mainly by inwardly-rectifying potassium channels. Should V_m exceed a certain limit (≈ -60 mV), voltage-gated potassium channels are activated. These subsequently decrease V_m again by increasing the potassium conductance. [2]

1.2.6 The Reversal Potential

The reversal potential E_R can be interpreted as the exact value of V_m at which the net flux of an ion species becomes zero, i.e. changes its direction [2]. Importantly, a change in current direction is physically equivalent to a change in current sign. For ions carrying a positive charge (cations, e.g. K^+ or Na^+) $V_m > E_R$ results in an outward current and $V_m < E_R$ results in an inward current [2].

For example, the Nernst potential of sodium is assumed to be $E_{Na} = +55$ mV. By applying a membrane potential of $V_m = E_{Na}$ and by assuming that the membrane is permeable for sodium only, equilibrium can be evoked. Since the electrochemical gradient is compensated by the applied voltage, the sodium current will vanish. [7]

The important point of this explanation is that E_R is equivalent to the Nernst potential in case a single ion species is considered to be permeable. When the system comprises more than one permeable ion species (i.e. when the whole cell is approached), E_R can be interpreted as the exact value of V_m at which the ionic current over the membrane changes its direction [7].

1.3 Ion Channels

Ion channels principally maintain electrodiffusion as the plasma membrane is normally impermeable for ions. The common pore that is formed between intra- and extracellular region can be considered as a conductor when open. Opening and closing of the pore goes along with conformational changes the channel has to maintain. [2]

The regulation of these conformational changes is vividly called *gating*. Ion channels can be gated via V_m (voltage-gated), extracellular transmitters (ligands) or mechanical stimuli. Furthermore, some channels are also gated via intracellular messengers such as ATP, Ca^{2+} , pH or cyclic nucleotides. [2]

1.3.1 Classification of Ion Channels

Ion channels are principally selective for a type of charge (cation or anion). Especially cation channels are referred to as highly selective (K^+ versus Na^+). The nomenclature of channels is therefore primarily based on the ion species that is permeable (e.g. potassium channels or K^+ -channels are considered to be permeable for potassium only). [2]

Common ions in cellular electrophysiology are K^+ (potassium), Na^+ (sodium), Ca^{2+} (calcium) and Cl^- (chloride) [3]. Therefore, ion channels can be principally classified as follows.

- Potassium channels or K^+ -channels
- Sodium channels or Na^+ -channels
- Calcium channels or Ca^{2+} -channels
- Chloride channels or Cl^- -channels

Classifying ion channels using the selectivity only is insufficient as the variety of channels is enormous. Therefore, the gating mechanism is conventionally used for classification purposes as well [10].

In accordance with an official classification scheme published by IUPHAR/BPS, ion channels can be further classified as follows [10]:

- **Voltage-gated ion channels**
- **Ligand-gated ion channels**
- **Other ion channels** (e.g. aquaporins, piezo channels, etc.)

YU ET AL.

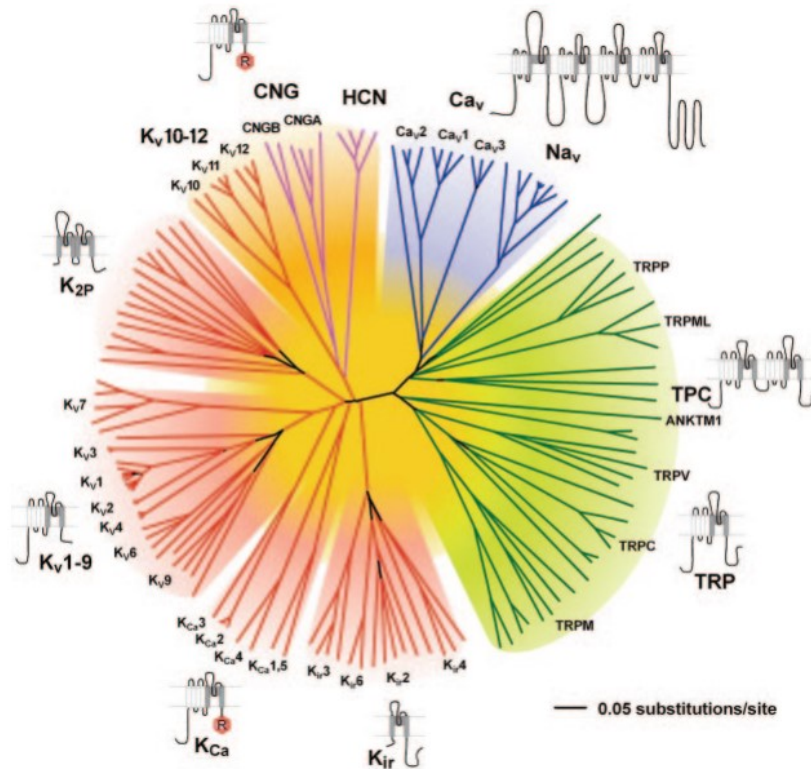


Figure 2: Voltage-gated superfamily [Yu FH and Caterall WA. The VGL-chanome: a protein superfamily specialized for electrical signaling and ionic homeostasis. 2004 quoted in 11]. It is composed of Ca_V (voltage-gated calcium channels), Na_V (voltage-gated sodium channels), TPC (two-pore channels), TRP (transient receptor potential channels), K_{ir} (inwardly rectifying potassium channels), K_{Ca} (Ca^{2+} -activated potassium channels), K_V (voltage-gated potassium channels), K_{2P} (two-pore domain potassium channels), CNG (cyclic nucleotide-regulated channels) and HCN (hyperpolarisation-activated, cyclic nucleotide-gated channels) [10].

Figure 2 shows that the voltage-gated superfamily, published in [Yu FH and Caterall WA. The VGL-chanome: a protein superfamily specialized for electrical signaling and ionic homeostasis. 2004 quoted in 11]. It shows that this superfamiliy not only includes purely voltage-gated channels. Therefore, it is also referred to as voltage-gated like ion channel superfamily in some publications [11].

1.3.2 Potassium Channels

Channel Structure

Today, it is an established fact that potassium channels are principally composed of transmembrane helices (TMs). This knowledge on basic molecular structure is reflected by many scientific reviews. [8], [12]–[14]

Identification of the molecular structure and subunit topology of potassium channels was initiated decades ago. For example in 1991, by determining the subunit stoichiometry, it was shown that shaker potassium channels have a tetrametric molecular structure [15]. Later in 1998, potassium channels consisting of two or six transmembrane helices were already known and a tetrametric subunit topology of potassium channels in *Streptomyces lividans* (KcsA-channel) was reported [16].

Figure 3 shows a comparison of molecular topologies of different potassium channels reviewed in [14]. It graphically illustrates that inwardly rectifying potassium channels consist of two, two-pore domain potassium channels (2PK) of four and voltage-gated potassium channels of six transmembrane helices [14].

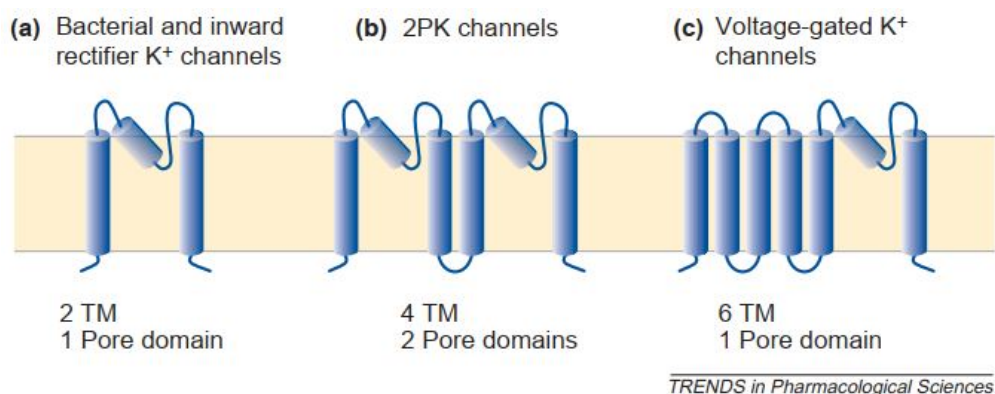


Figure 3: Topologies of K^+ -channels [14].

Voltage-gated Potassium Channels

As this thesis focusses on K_V -channels in MCF-7 and MCF-10A, the voltage-gated superfamily and the K_V -channel family are of particular interest.

In voltage-gated potassium channels, each subunit of the tetramer consists of six transmembrane helices where the S4-helix is referred to as the voltage sensor of the subunit. This particular TM is able to move in direction of the extracellular region (in case of depolarization) or in direction of the intracellular region (in case of repolarization), dependent on the membrane potential V_m . Activation of K_V -channel pores is initiated by depolarization and corresponding movement of the voltage sensor. The channels are deactivated on repolarization, performing the same sequence in opposite direction. Activation and opening, as well as the terms deactivation and closing are synonymously used, respectively. During activation and deactivation the channel goes through a cascade of conformational changes. [2]

A very important property of K_V -channels, especially regarding kinetic modelling, is inactivation.

By inactivation the conductance of the channel reduces over time, although the depolarizing membrane potential is still present. In K_V -channels, N- and C-type inactivation are known. For N-type inactivation the so called inactivation domain binds on a receptor inside the pore and thereby blocks the channel. In contrast, C-type inactivation is typically slower and caused by conformational changes in certain parts of the channel. The states of an arbitrary K_V -channel can therefore be divided into open, closed and inactivated (closed). [2]

1.3.3 Ion Channels and Proliferation

Several comprehensive scientific reviews were published, summarizing knowledge on ion channel activity linked to cell cycle progression. Some channels are specifically expressed in different cancer cells [17]. These will be partially addressed in chapter 1.5.8.

The circumstance that ion channel expression/activity correlates with cell proliferation has been established a long time ago. As far back as 1984, it was suggested that potassium channels influence mitogenesis as it was observed that K^+ -channel blockers inhibited 3H -thymidine incorporation in T-lymphocytes [18]. Some years later in 1986, modulation of potassium channel conductance correlating with cell cycle progression was observed in mouse T helper clones [19]. Today it is known that ion channel expression/activity changes in relation with distinct phases and checkpoints in the cell cycle of many cells but deriving a general rules is challenging due to heterogeneity of this issue [20].

As soon as channel activity and/or expression changes, V_m changes as a consequence. As reviewed in [20], the membrane potential is therefore considered to be directly linked to proliferation as well as its modulation was suggested to be mandatory for passing checkpoints in the cell cycle. The fluctuation of V_m during the cell cycle was considered to be a general property of cells in the review by [21]. In this context it is important to highlight that K^+ -channels dominate in maintaining the resting membrane potential [2], [21].

It has been reported that the resting membrane potential shows rhythmic changes as a cell progresses through the cell cycles. These oscillations can be interpreted as periodic changes of conductance of the membrane. [21]

Figure 4 shows the potassium conductance and membrane potential V_m during cell cycle progression, published as part of a review on this issue in 2014 [21]. Amazingly, the cyclic changes in membrane potential illustrated in figure 4 were already outlined decades ago.

In 1974 it was shown that the membrane potentials of Chinese hamster lung cells oscillated when the cells progressed through the cell cycle as a sudden and persistent onset at the beginning of the S-phase could repetitively be observed [22].

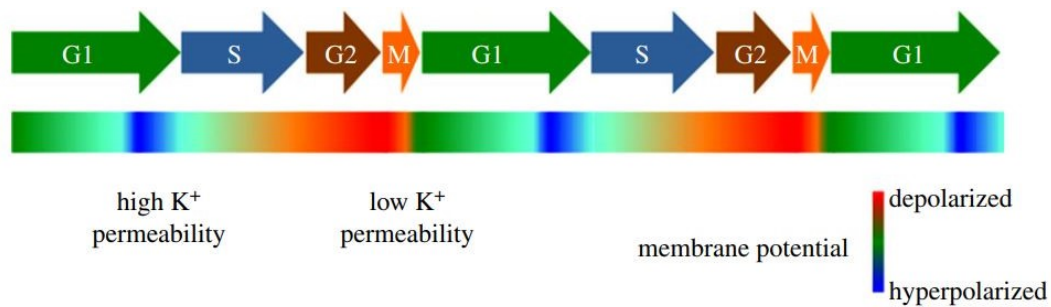


Figure 4: K⁺ conductivity and V_m over the cell cycle adapted from [21].

Previous studies revealed two resting membrane potential levels a cell has to maintain at the right time for passing the checkpoints G1/S (hyperpolarization) and G2/M (depolarization) during cell cycle progression [20], [21], [23].

Furthermore, it is widely accepted that K_V-channels participate in cell cycle regulation up to a certain point, using multiple mechanisms. They contribute in setting V_m of the cell, simultaneously influencing the Ca²⁺-flux over the membrane and furthermore, they directly participate in volume regulation. [21], [23]

The mentioned findings presented in this chapter are exemplary and not meant to be a complete review on this topic. Interested readers are referred to the reviews [20] and [24] that constitute great references for delving more deeply into this subject.

1.4 Cellular Electrophysiology

1.4.1 Patch-clamp Technique

In patch-clamp, a patch-pipette with a relative large front end diameter of circa $1\text{-}5\ \mu\text{m}$ is initially put onto the cell membrane. With a slight suction, the gap between pipette and membrane surface is closed, creating a high seal resistance of approximately $1\text{-}100\ \text{G}\Omega$ (*gigaseal*) at the same time. [3]

Different measurement configurations are available but all measurements start with establishing a gigaseal formation by approaching the whole, intact cell. This initial configuration is called *cell-attached patch-clamp* configuration. [5]

Cell-attached patch-clamp is also known as *on-cell patch-clamp*. Dependent on the targeted measurement values, the patch can further be broken and/or removed from the cell. [3]

Figure 5 shows further patch-clamp configurations derived from the centrally located on-cell patch-clamp configuration [25].

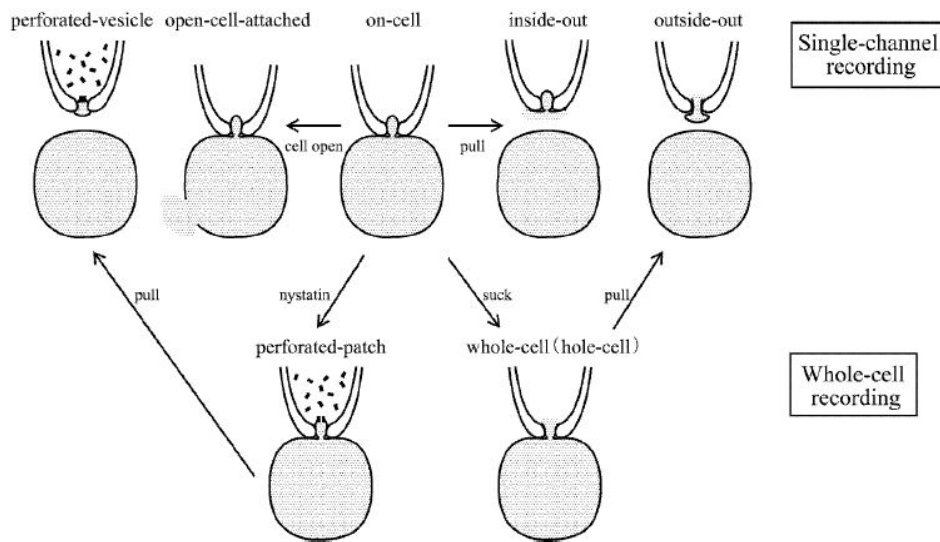


Figure 5: Overview of patch-clamp configurations [25].

The measurement arrangement of patch-clamp measurements is relatively simple.

The measured cell and a reference electrode (ground/bath electrode) are put into in a conductive bath. The patch-pipette is filled with a conductive solution, a voltage is applied and as soon as the pipette is in contact with the bath solution, a current flows to ground. By measuring this current, the pipette resistance R_p can be determined. [5]

When the pipette is lowered into the bath, a small pressure should be applied to avoid dust contamination on the tip. A gigaseal can be formed just by releasing the pressure on the pipette and eventually applying additional suction. [25]

The cell-attached configuration can be used to measure single channels in their physiological (i.e. in their normal) environment. Therefore, the pipette solution has to resemble the extracellular composition for this. The resting membrane potential is unknown in this configuration. [3]

Whole-cell Patch-clamp

As the name suggests, this configuration is applied to measure the electrophysiological behaviour of the cell as a whole [3]. The patch under the pipette is usually ruptured and destroyed by gently applying a negative pressure (suction), creating a low-resistive access to the inner compartment [5]. An exchange of intracellular solution with pipette solution is the consequence [3]. A slow transient in the current response will be seen because of the influence of the membrane capacitance C_m [5]. Breaking the patch results in a resistance R_s (typically $< 15\text{-}20\text{ M}\Omega$) in the passage of pipette to cytoplasm [5].

Alternatively, the patch under the pipette can also be made permeable to ions using chemical agents like Nyastin. Establishing electrical access to the cytoplasm this way is called *perforated-patch method*. [3]

Figure 6 shows the equivalent circuit diagram of the whole-cell configuration.

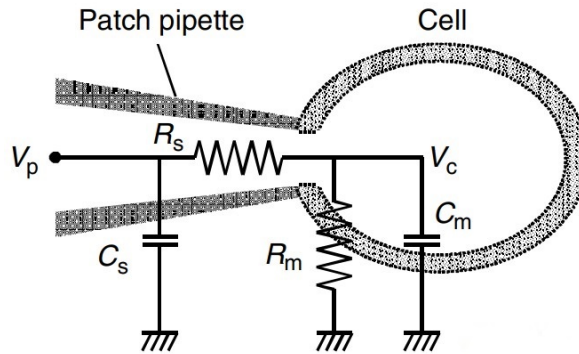


Figure 6: Equivalent circuit of the whole-cell configuration adapted from [26]. The series resistance R_s is the access resistance to the cytoplasm, the parameters C_m and R_m are the capacitance and resistance of the cell membrane, the capacitance C_s represents the stray capacitance of the arrangement and V_p refers to the applied voltage on the electrode [26].

The capacitive components shown in this circuit cause characteristic transients in measurements. These disruptive transients are typically compensated by the amplifier circuit of the measurement arrangement. The series resistance is usually compensated as well. [25]

Single-channel Patch-clamp

Single-channel patch-clamp measurements allow studying individual ion channels in cell-attached, inside-out or outside-out configuration. Especially in the excised-patch configurations (inside-out and outside-out), the probability is high that just a few channels are present in the patch. Currents measured in these configurations are typically very small (pA-range). Due to current magnitude and noise, a high seal resistance needs to be established. [5]

Inside-out patch-clamp

By pipette retraction from the initially established on-cell configuration, the membrane will rupture around the pipette, allowing the extraction of the patch from the membrane. In case a vesicle is formed on the pipette tip, a brief exposure to air (lifting out of the bath solution) will destroy it, exposing the intracellular side directly on the pipette. [5]

In this configuration intracellular factors on single channels can be studied [3].

Outside-out patch-clamp

This configuration is established by retraction of the pipette in the whole-cell configuration. The membrane will rupture and reform, exposing the extracellular side to the bath. [5]

This configuration allows studying extracellular factors on single channels [3].

1.4.2 Voltage- and Current-clamp Technique

Due to the fact that the conductivity of the plasma membrane shows a strong dependency on the membrane potential, clamping of voltage is particularly desirable for obtaining a controlled measurement environment. [5]

Currents through ion channels are usually measured using the voltage-clamp technique [2]. As the name suggests, the membrane potential is clamped to a fixed value V_C (clamping potential) and the voltage- and time-dependent change of conductivity is observed [3]. This is realized by injecting a current into cell that pleasantly reflects the ionic current at the clamped potential [2]. In most cases, a rectangular voltage pulse is used as clamping potential V_C [3]. This voltage is often incremented stepwise in accordance with a so called pulse or step protocol [5]. In voltage-clamp, a direct correlation between V_m and ionic current is the result, additionally reflecting the ionic conductivity at a particular membrane potential [2], [3].

In contrast to the voltage-clamp technique, a transient signal on the membrane can also be measured using the current-clamp technique. Here, a constant current is injected into the cell, resulting in a characteristic voltage response. [3]

Current-clamp not only allows the measurement of V_m and its dependence on a constantly injected current, also the resting membrane potential can be determined with this technique [5].

1.5 Cancer and Cancer Electrophysiology

This chapter introduces to the terminology and classification of cancer. Carcinogenesis is described, using the hallmarks of cancer. Correlations between cancer progression and electrophysiological properties of cells are outlined. Finally, the scoped cell lines of this thesis are briefly introduced and described.

There has been made an extensive progress in cancer research but it seems like the big picture is still incompletely understood which is of course related to the complexity of this disease. The introduction to cancer biology and breast cancer in this thesis is not meant to be a complete review of current knowledge in cancer research. However, it should serve as a short overview to known mechanisms and established concepts in order to get a feeling on what cancer principally is and how this disease develops and behaves.

1.5.1 Terminology and Definitions

Cancer is a disease that develops from normal cells and can affect virtually any part of an organism. All cancers tend to uncontrolled cell division and invasion by which the surrounding, healthy tissue is destroyed. In its final form, cancer is capable of colonizing foreign anatomical sites, survive there and start replicating and invading tissue there as well. [27]

All cancers show these characteristics with exception of brain cancer and basal cell carcinomas of the skin. These cancers are not able to leave the site in which they originally developed. [27]

Although cancer development follows certain principles, there is no standardized pattern of this process, since it is driven by random acquisition of mutations during expansion. Tumor cells lost their mutation control and by proliferation, the tumor produces waves of subclones, increasing the heterogeneity of the population in each step. [27]

Cancer cells derive from normal cells due to changes in their genetic material as described. These changes can be induced by ionizing radiation, chemical reagents or hereditary. Certain viruses, bacteria and parasites are capable of inducing this transformation as well. [2]

Cancer

Cancer is the designation of a malignant neoplasm. An accepted synonym for cancer in the field of oncology is tumor. [27]

Neoplasm

A neoplasm is always considered to be pathological and refers to a new and abnormal growth of tissue [27].

Tumor

There is no exact definition of the term tumor as it just describes a mass or swelling. Masses are always considered to be pathological but may or may not be neoplasms. [27]

Metastation

The systemic spread of cancer cells in context of cancer progression is referred to as metastation [27]. The product of metastation is called a metastasis or multiple metastases.

Carcinogenesis

Carcinogenesis is an interchangeable term for cancer development [27]. The term tumorigenesis is synonymously used [28].

1.5.2 Benign and Malign Neoplasms

Based on appearance and functionality, neoplasms are divided into benign and malign. Growth pattern and appearance are used for classification and build the basis for pathological diagnostics of cancers. However, it is not always possible to distinguish between benign and malign neoplasms with a complete certainty. [27]

Most malignant neoplasms develop from normal cells but it is also possible that a malign neoplasm derives from an existing benign one [27].

The important difference between benign and malign neoplasms lies in the capability of producing metastases. While malign neoplasms are able to develop metastases, benign neoplasms are completely missing this capability. Importantly, metastatisation is referred to be the primary death cause in cancers. [27]

For metastation, malign cells need to gain several new capabilities which are acquired by mutations to the most part. Only these allow the cells to consequently leave their origin and to enter foreign sites, like the lymphatic system or the blood. [27]

Benign neoplasms are missing the ability of metastation but can cause death by growth and expansion in their original site. Smooth contours and encapsulation are characteristic attributes of benign cells compared to their malign counterparts. [27]

1.5.3 Development of Cancer

The process of carcinogenesis usually takes many years. It starts with an initial mutation of a cancer-causing gene (proliferation or mutation control gene) in a cell. A cancer-causing gene can either be a proto-oncogen (involved in proliferation control) or a tumor suppressor gene (involved in mutation control). Mutated proto-oncogenes are called oncogenes then. The initial mutation is simply called *initiation*. [27]

By a mutation in the right gene, carcinogenesis is initiated and mutated cells are the result. These then divide and generate further mutated clones. This step is called *promotion*. [27]

Following daughter cells may then be afflicted with additional mutations. This is called *progression*. The variety of acquired mutations causes the vast heterogeneity of most malign neoplasms. By mutation, the cancer can gain novel capabilities and may then be able to invade or destroy surrounding tissue or to travel to foreign anatomical sites and survive there. [27]

Before the malign transformation has succeeded, pre-malignant changes in tissue known as dysplasias are already observable. However, it is not possible to completely determine whether a dysplasia will develop to a malign neoplasm or not. [27]

1.5.4 Classification of Cancer

It is common knowledge that cancer is a highly heterogeneous disease. Therefore, it is not surprising, that cancer can be subdivided in many categories. More than 100 types of cancers and tumor subtypes can be found in different organs [28]. Referring to [27], cancers can be classified as follows:

- Carcinoma
- Sacroma
- Lymphoma and leukemia
- Melanoma
- Mesothelioma
- Cancer of brain and central nervous system
- Germ cell cancers

Carcinomas are malign neoplasms of epithelial tissue and represent the most common type of human malignancies (80 to 90 %). They are also known to develop metastases. [27]

According to [27], carcinomas can further be subdivided as follows:

- Squamous cell carcinomas
- Adenocarcinomas
- Neuroendocrine carcinomas

Adenocarcinomas are referred to as the most common class of carcinomas in humans. Ductal and lobular breast carcinomas are classical adenocarcinomas. [27]

1.5.5 Hallmarks of Cancer

Decades of cancer research revealed certain rules carcinogenesis follows when transforming normal cells into cancer cells (malign transformation). Back in 2000, there already was evidence that carcinogenesis alters the genotype and breaches single anti-tumour barriers of cells in a step-wise manner. Suggested were six distinct checkpoints carcinogenesis needs to pass in order to accomplish the malign transformation. It was proposed that these steps are shared among most types of cancers. [28]

Figure 7 shows an overview of these steps proposed by Hanahan et al. 2011 from their extended publication on the hallmarks of cancer [29]. The publication from 2011 [29] refers to the publication from 2000 [28].

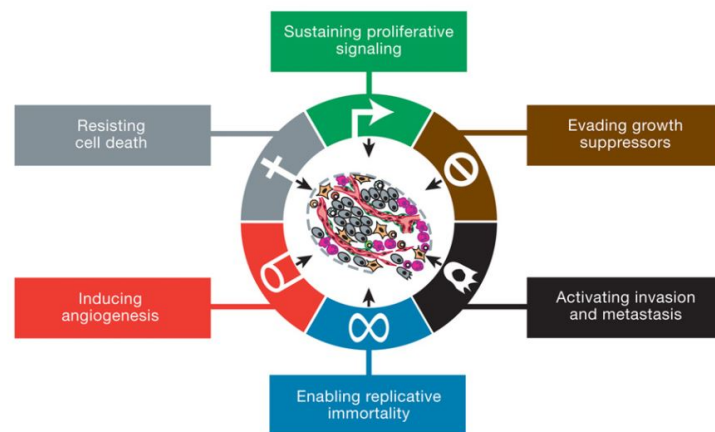


Figure 7: Hallmarks of cancer [29].

Cancer cells develop the capability of becoming independent on mitogenic growth signals. These are normally provided externally by the microenvironment in the tissue and needed for leaving the quiescent state. Cancer cells become capable of synthesizing mitogenic growth factors on their own. [28]

By proceeding in transformation, cancer cells gain the ability of becoming insensitive to growth suppressors. Normally, the proliferation of healthy cells is regulated by antigrowth signals. These force the cells either into the quiescent state or into a permanent, differentiated postmitotic state when proliferation is denied. Tumor cells developed multiple strategies to bypass this mechanism. [28]

By monitoring intracellular and extracellular environment, a signalling cascade decides on the programmed cell death of abnormal cells. Also here, cancer cells developed multiple strategies to overcome this regulative mechanism. A very common example is the mutation of the p53 tumor suppressor gene that results in loss of pro-apoptotic signalling. [28]

In order to generate a vast number of cells, cancer cells need to gain the capability of limitless replication. As healthy cells normally maintain a program that limits their multiplication, cancer cells must overcome this limitation in order to expand. One barrier constitutes the presence of tumor suppressors. Another barrier is the mortality barrier that, in case of breaching during transformation, reveals unlimited replicative potential. [28]

Cancer cells are in need of forming new blood vessels for supplying the tumor with nutrients and oxygen in order to advance the expansion. This process is called angiogenesis. In normal cells angiogenesis is tightly regulated within the tissue. Cancer cells lack these kind of regulation by gaining the capability of inducing and maintaining angiogenesis after a certain step in carcinogenesis. [28]

After the tumor has gained all these capabilities the cancer cells will spread in the body, settle on occasion and create new colonies. This requires the outspreading cells to be able to adapt to new environments. The tumor from which the metastases developed is then referred to as the primary tumor. [28]

1.5.6 Breast Cancer

Like cancer in general, breast cancer is a heterogeneous disease with many facets. As described, breast cancer is an adenocarcinoma [27].

Clinically, this type of cancer can be anatomically classified by the location of the tumor (ductal or lobular). Additionally, breast cancer can be molecularly classified by the hormone receptivity (estrogen receptor ER, progesteron receptor PR and human epidermal growth factor 2 receptor HER-2). [30]

Breast cancer can be classified by using the corresponding identities as shown in table 1. The molecular identity also hints the aggressiveness of the breast cancer subtype. [The Physician Assistant Student's Guide to the Clinical Year: OB-GYN quoted in 30]

Subtype	ER	PR	HER-2
Luminal A	+	+	-
Luminal B	+	+	\pm
HER-2 positive	-	-	+
Triple negative	-	-	-

Table 1: Molecular classification of breast cancer [The Physician Assistant Student's Guide to the Clinical Year: OB-GYN quoted in 30]

1.5.7 Breast Cancer Cell Lines

Cell lines are extensively used in cancer research as they provide a self-replicative source of cells with high homogeneity [31]. It is logical that working with such a homogeneous cell population makes measurements reproducible and results from different studies comparable [32]. The amount of available cell lines in breast cancer research is high but surprisingly only a few cell lines are extensively used [33]. However, cell lines can also be afflicted by geno- and phenotypic deviations, distorting results [31]. Conclusions from observations or measurements in cell lines should be derived cautiously since cell lines do not always completely replicate the behaviour of the primary cells and often the subjected cells are not completely understood as well [32].

With respect to citations, the MCF-7, MDA-MB-231 and T47D are the most prominent breast cancer cell lines (popularity decreasing by this order). Interestingly, most of the cell lines are not derived from the actual tumor, but from metastases. [31]

Figure 8 schematically illustrates the correlations between breast cancer tumors and cell lines using the introduced molecular identities [33].

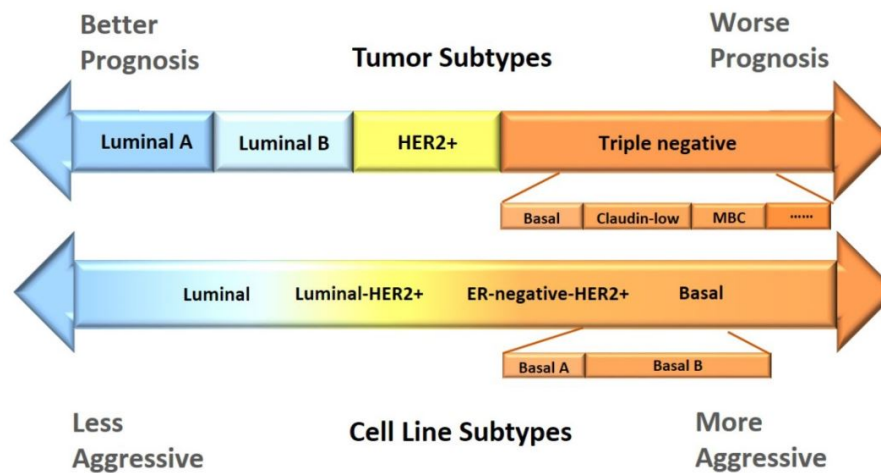


Figure 8: Equivalence of breast cancer subtypes [33].

MCF-7 denotes a popular breast cancer cell line [34]. MCF-10A denotes a popular cell line of normal breast cells [35].

The according cells of MCF-7 were isolated from a pleural effusion. The term MCF derives from the place where its establishment took place, the *Michigan Cancer Foundation*. [Soule et al. A human cell line from a pleural effusion derived from a breast carcinoma. 1973 quoted in 34]

Regarding its molecular identity, MCF-7 cells are ER-, PR+ and HER2- and therefore assigned to the luminal A subtype (data from review) [33]. Functions of MCF-7 cells resemble those of normal epithelial cells in many ways [34].

Originally isolated from benign breast tissue in 1990, MCF-10A cells are ER- and non-tumorigenic. Two types of these cells are known: MCF-10A (attached) and MCF-10F (floating). [36]

As illustrated, these two cell lines are rather contrary with respect to molecular identity and tumorigenicity. It will be shown in upcoming chapters that this contrast is additionally reflected by the expression of ion channels known by today.

1.5.8 Ion Channels in Cancer

A strong correlation between ion channel expression and different cancers has been reported by several scientific reviews [17], [20], [23].

As reviewed in 2020, several ion channels may be focussed as promising targets in cancer therapy and diagnostics, especially members of the K_V10 and K_V11 families [23].

The voltage-gated potassium channel $K_V10.1$ was reported to be a well-studied ion channel in cancer research [21]. Experimental data from CHO cells showed that overexpression of $K_V10.1$ stimulated growth and the cells lost dependence on growth factors [37]. These characteristics were previously described as typical hallmarks of cancer. Therefore, expression of $K_V10.1$ is considered to be an advantage for proliferation in tumor cells [37]. Noticeably, no expressions have been reported in cells of healthy mammary gland [37].

By exposing SKBr3 and MDA-MB-231 cell lines (both known to express $K_V11.1$) to the channel activator NS1643, cell cycles could be arrested in G0/G1-phase [38].

From experimental data, $K_V11.1$ was also shown to have an impact on apoptosis and tumor cell growth. It was suggested that the channel promotes carcinogenesis and the expression of $K_V11.1$ was considered as a significant advantage in cancer development. [39]

Importantly, $K_{V10.1}$ and $K_{V11.1}$ are just two isolated examples as there are striking indications that actually a large amount of different channels correlate with cancer development and progression [17]. As it will be shown in chapter 4.1, $K_{V10.1}$ and $K_{V11.1}$ will be of particular interest with respect to MCF-7.

Up- and down-regulation of ion channel expressions were shown to vary among different cancer cells. By today, a general rule of channel expression in cancer cells could not be determined as expression profiles were reviewed to be very complex. [17]

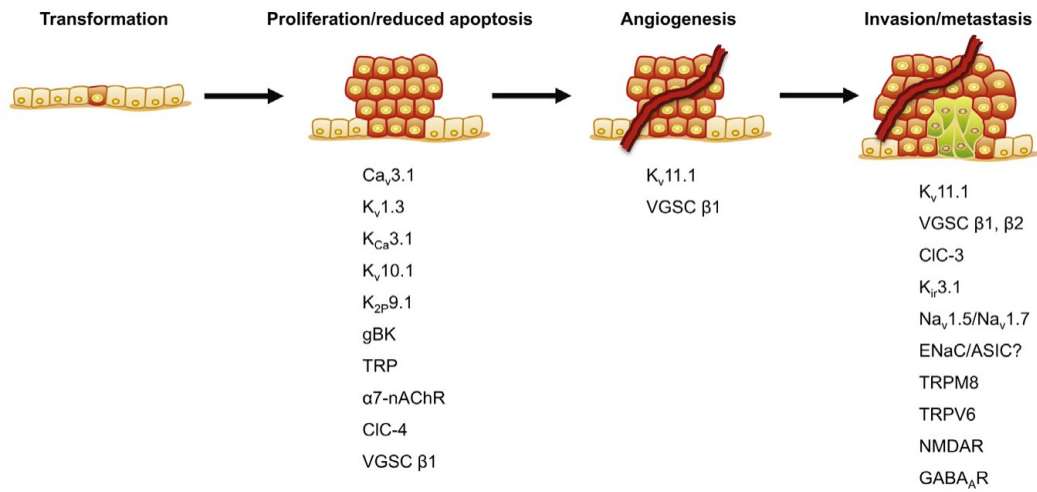


Figure 9: Ion channel expression and carcinogenesis [17].

Figure 9 shows collections of ion channels that were suggested to promote distinct phases in carcinogenesis. In this context, changing ion channel expression levels were considered to promote proliferation, angiogenesis, invasion and metastasis in cancer progression specifically. [17]

Typically, cancer cells tend to maintain a more depolarized resting membrane potential compared to healthy cells [17], [20]. For example, experimental data from 1995 revealed that V_{rm} in multiple neuroblastoma cells was significantly depolarized and varied in a range of -40 to -20 mV [40].

This is interesting as it was previously described that cell proliferation strongly correlates with the membrane potential (see chapter 1.3.3).

Depolarization was suggested to influence the activity of voltage-gated channels. In this context it is still unclear, if ion channel expression alone or the combination of altered channel expression and resulting change in resting membrane potential affects cell proliferation. [17]

In the review published by [17] in 2016, ion channels were suggested to have a series of impacts on cancer development and progression, based on observations from previous studies. Referring to [17], these impacts are summarized in figure 10.

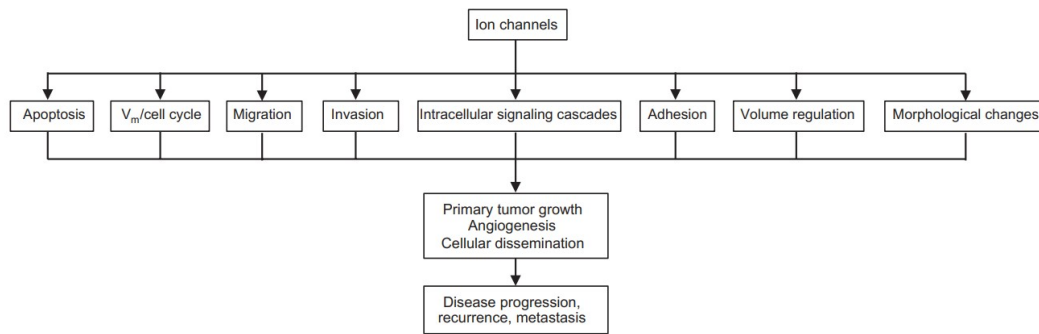


Figure 10: Roles of ion channels in cancer [17].

At this point, interested readers are referred to the comprehensive review on ion channels in cancer by [17] and the review on voltage-gated potassium channels in cancer by [23]. Both publications serve as great references in this context.

1.5.9 Electrophysiological Characteristics of MCF-7

With respect to the primarily focussed cell line in this thesis, the electrophysiological characteristics of MCF-7 are outlined in the following. Additionally, representative whole-cell patch-clamp measurements of MCF-7 and MCF-10A cells from literature are presented.

A frequency distribution analysis of membrane potentials in MCF-7 showed four significant levels and suggested a changing resting membrane potential when these cells progress through the cell cycle [41].

Figure 11 shows the concerning distribution of membrane potentials, measured in a colony of 188 unsynchronized cells. Four peaks were suggested to be clearly identifiable. [41]

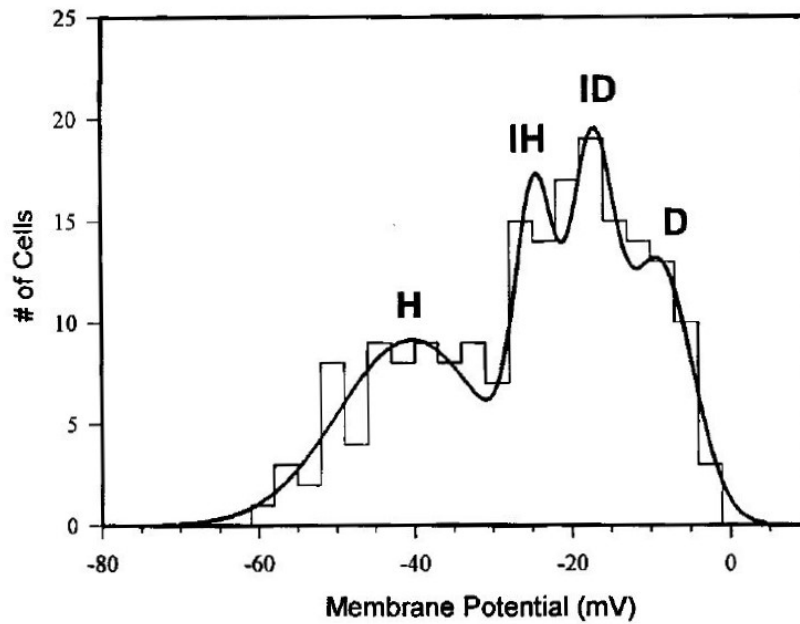


Figure 11: Membrane potential distribution in MCF-7 colony [41]. H stands for hyperpolarized, IH for intermediate hyperpolarized, ID for intermediate depolarized and D for depolarized [41].

In one study, V_{rm} in MCF-7 cells varied in a range of $V_{rm,min} = -58.6mV$ and $V_{rm,max} = -2.7mV$ [41]. Another study reported that the resting membrane potential varied in a range of approximately $V_{rm,min} = -72mV$ and $V_{rm,max} = -9mV$ [42]. Resting membrane potentials of these cells were generally reported to be more depolarized than in normal human mammary epithelial cells [43]. Nevertheless, it should be noted at this point that the reported ranges of resting membrane potentials are actually rather large.

By accumulating the cells in different passages of the cell cycle the conclusion could be made that V_{rm} hyperpolarizes in the G₁-S transition [41]. This has been confirmed by a subsequent study, in which it was suggested that hyperpolarization is initiated during G₁-phase [42].

With respect to figure 11, a significant correlation of the group D with cells in early G₀/G₁-phase was reported [41]. Results of membrane potential measurements of MCF-7 cells arrested in G₀/G₁-phase supported this correlation (V_{rm} measured in a range of -34 mV to -10 mV during G₀/G₁) [42]. Also the stepwise change of V_{rm} , proposed in [44] and shown in figure 12, fits this pattern.

The hyperpolarization of MCF-7 cells was shown to be caused by an increase in potassium current, underlining the particular importance of potassium in governing the resting membrane potential [42]. MCF-7 cells were also shown to be sensitive to surrounding Ca^{2+} concentrations as the absence of external Ca^{2+} induced cell death [43]. Described correlations of cell cycle phases and resting membrane potentials in MCF-7 are illustrated in figure 12 as well.

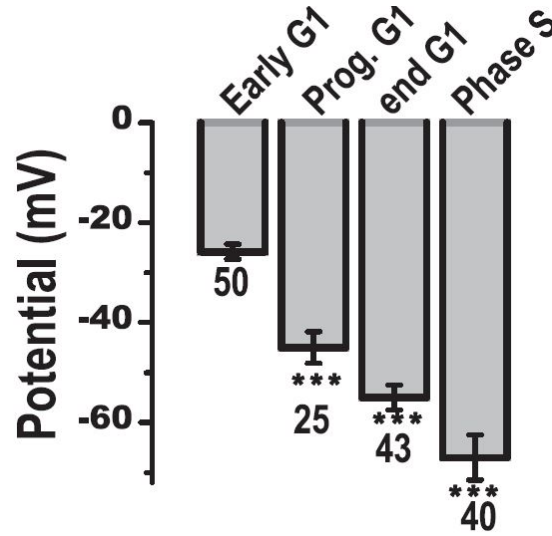


Figure 12: V_m over cell cycle phases in MCF-7 [44]. The numbers of investigated cells correlating with each phase are referred to under each bar [44].

Table 2 shows an overview of channel antagonists and their impact on growth and proliferation in MCF-7. Interestingly, opening potassium channels using minoxidil was shown to result in a dose-dependent stimulation of growth in MCF-7 cells [45]. In contrast to the inhibiting potential of Tetraethylammonium (TEA) shown in table 2, another study reported growth stimulation when using it on MCF-7 cells [43].

Name of agent	Targets	Inhibition	Arrest	References
Quinidine	K_{V10} , $K_{V1.4}$, $K_{V1.5}$, $K_{V1.7}$, $K_{Ca5.1}$, K_{Na1}	Growth	G ₀ /G ₁	[10], [42], [46], [47]
TEA	K_VX , K_{CaX}	Growth	G ₀ /G ₁	[10], [42], [46]
4-AP	K_{V1} , K_{V2} , $K_{V3.1}$, $K_{V3.2}$, $K_{V3.3}$, K_{V4}	Growth	*	[46], [47]
Amiodarone	$K_{V1.7}$	Growth	**	[45], [47]
α -DTX	$K_{V1.1}$, $K_{V1.2}$, $K_{V1.6}$	Proliferation	**	[10], [48]
Astemizole	$K_{V10.1}$, $K_{V11.1}$	Proliferation	G ₀ /G ₁	[10], [42], [47], [49]

Table 2: Channel blockers and MCF-7 proliferation. * indicates a lack of significance and ** indicates that no data was available in the reference. Growth and proliferation inhibition refers to considerations in quoted references. Arresting the cell in a specific phase of the cell cycle can be naturally considered as an inhibition of proliferation as well. Exemplary target channels are listed for each blocker. The target channel names K_VX and K_{CaX} refer to divers varieties of voltage- and calcium-gated potassium channels.

Figure 13 shows a whole-cell patch-clamp measurement of an MCF-7 cell with and without TEA perfusion, published by [48]. Furthermore, a whole-cell patch-clamp measurement of an MCF-10A cell, published by [50], is shown in figure 14 in this context.

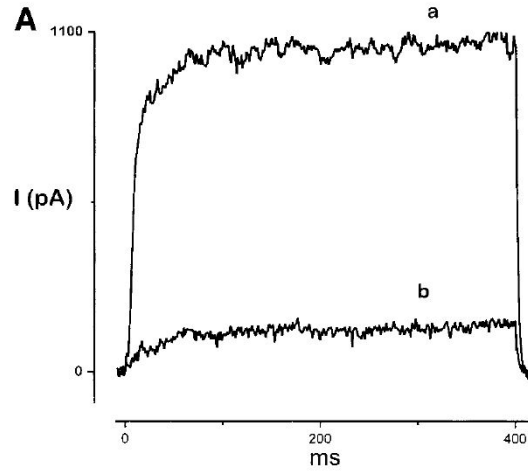


Figure 13: Whole-cell patch-clamp measurement of MCF-7 cell [48]. A current measurement of an MCF-7 cell in whole-cell patch-clamp configuration for a depolarizing voltage pulse from -60 mV to +60 mV without (a) and with (b) TEA perfusion is shown. Both membrane capacitance, pipette capacitance and series resistance were compensated. [48]

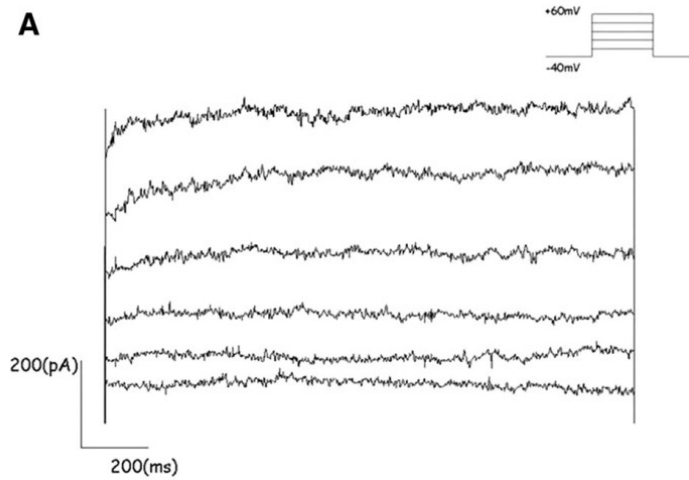


Figure 14: Whole-cell patch-clamp measurement of MCF-10A cell [50]. The whole-cell current of the cell is shown for varying clamping potentials in a range of -40 mV to 60 mV, using a 20 mV incremental step size. The measurement duration was 800 ms. [50]

2 Problem Definition

Cancer is doubtless a very complex disease. Understanding specific aspects of cancer may open the way for the development of more advanced diagnostic and therapeutic approaches in order to address this disease more effectively in the future. Therefore, a lot of research in different fields is currently carried out.

The aim of this thesis is the implementation of a first approach, modelling the currents maintained by K_V -channels in MCF-7 and MCF-10A. Using an appropriate method and provided experimental data, whole-cell currents of these cell lines are finally approximated by these specific potassium currents (cell models).

Based on the results of a comprehensive literature research, the current knowledge on the K_V -channel expression in both cell lines is specified in this work.

By carrying out a second literature research on corresponding kinetic models for these particular channels, the expressed K_V -channels are subsequently modelled using a Markov Model approach.

Through combining the single channel models, cell models of MCF-7 and MCF-10A are developed. The macroscopic currents of integrated single channel models in the corresponding cell models are subsequently optimized using provided experimental data of whole-cell patch-clamp measurements and a particle swarm optimization, taking into account the current knowledge on their individual contribution based on experimental data from literature.

3 Methods

Referring to the problem definition, the work in this thesis was split accordingly. The modelling process is graphically illustrated in figure 15.

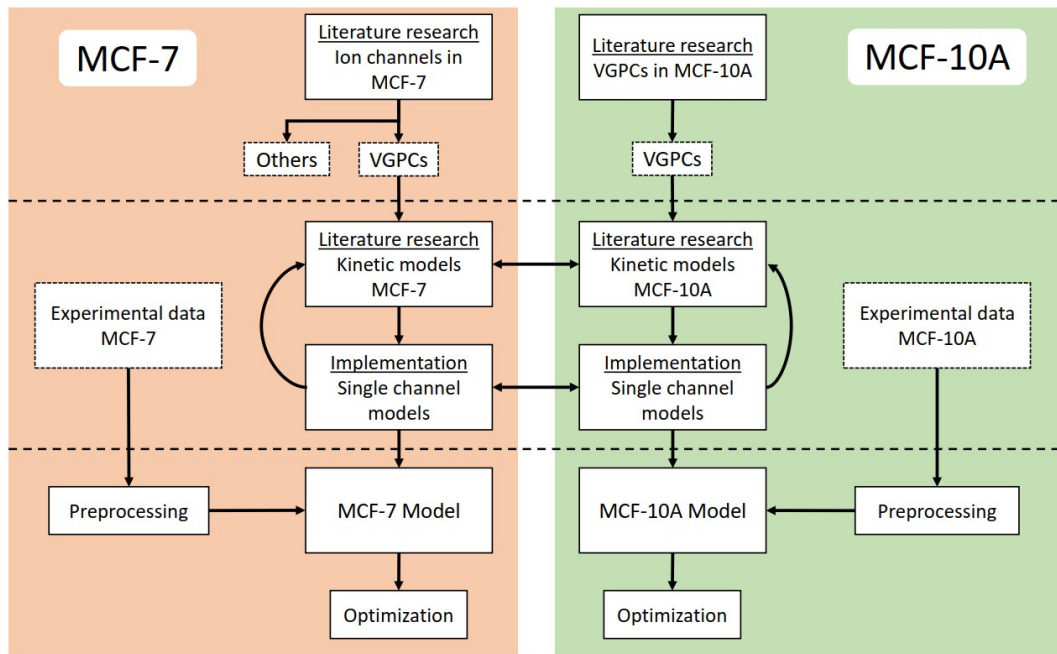


Figure 15: Workflow of cell modelling.

In step one, literature researches on ion channel expressions were carried out. The results were the K_V -channel (VGPC) expressions in MCF-7 and MCF-10A cells. Based on these results a subsequent literature research was carried out for implementation of single channel models (step two). As most kinetic models did not instantly fit, iterating through a pool of available

models for selection was inevitable. In the final step three, successfully implemented single channel models were integrated in corresponding cell models. Experimental data was preprocessed and used for optimizing the macroscopic currents of the cell models by optimizing the expression levels of integrated single channel models. The entire modelling process was split into software components accordingly and implemented using MATLAB R2022a (The MathWorks Inc., Natick, Massachusetts, USA).

As it is discussed in corresponding chapters in this thesis, many channels are known to co-assemble with other subunits, altering electrophysiological characteristics. For example, $K_V7.1$ is known to have a different single channel conductance when co-assembled with KCNE1 subunits [47]. In this thesis, all K_V -channels were considered to be homomeric, i.e. no heteromultimerization was considered for single channel modelling.

3.1 Experimental Data

Whole-cell currents of patch-clamp measurements were provided in the form of binary files (abf). The experimental data of MCF-7 and MCF-10A comprised five measurements each. For MCF-7, two patch-clamp measurements were performed in a first system and three measurements were performed in another system. Depending on the used measurement system, the whole-cell currents showed different offsets and scaling. The electrophysiological recordings of MCF-10A were provided identically to the MCF-7 data but the same measurement system was used for all five measurements. Therefore, all whole-cell currents were scaled by the same scaling factor and all measurements were afflicted by the same offset. Each measurement comprised 24 whole-cell current curves and all correlated with the same voltage pulse protocol.

All measurements were carried out at room temperature. No capacitive transient compensation was performed. This resulted in relatively high capacitive peaks at times where the clamping potentials were changed. The pulse protocol and each measurement had the same length in time (2 s). The sampling frequency of the measurements was read from the binary files and had the value $f_{S,Measure} = 10kHz$.

Loading the experimental data was implemented using the function *abfload* in the version 1.13.0.0, provided by Forrest Collman (2022) and pulled from the official *MathWorks File Exchange* [51]. This function was embedded in the function *getabffile.m* in which also a time vector for the measurement data was generated.

Furthermore, the data was scaled based on the used measurement system. The function *getabffile.m* is called in the functions *mcf7_model_load_data.m* and *mcf10_model_load_data.m* in which also the preprocessing of the concerning data was implemented.

The experimental data of whole-cell patch-clamp measurements was finally used for optimizing the channel expressions in the MCF-7 and MCF-10A cell models. For each of the 24 clamping potentials in the pulse protocol, there were five corresponding whole-cell current traces for each cell line. No further information was provided on measurement configuration and protocol. The measurement data for MCF-7 was preprocessed in three sequential steps: offset correction, averaging and removal of capacitive peaks. The same was done for the MCF-10A data but as these cells were measured in one measurement system only, no offset correction was required in this case.

3.1.1 Data Preprocessing

Each step of data preprocessing is briefly described in the following. The figures 35 to 38 show the raw measured whole-cell currents of MCF-7 and the currents after each step in preprocessing. The same is shown for the whole-cell currents of MCF-10A in the figures 39 to 41.

It was clearly visible that the two measurement systems resulted in two different offset values for the whole-cell currents. For averaging corresponding currents curves, an offset correction (referred to as OSC in the implementation) was required. This was realized by calculating the average whole-cell current of all 24 measurements during the first 30 ms for each of the five measurements.

One measurement was chosen as reference and the offsets of the other measurements were corrected with respect to the reference measurement. Note, that this offset correction was relative. The absolute offset of the measurement data was unknown.

The data was averaged after offset correction. This is denoted as AVG in the implementation.

The measurements showed significant and disruptive capacitive peaks in the current traces. These artefacts were unwanted, especially in terms of optimization. As no further information was provided on the measurements, the peaks were simply cut from the curves. This is referred to as RCP in the implementation. A cutting duration Δt_{Cut} was defined. Within Δt_{Cut} the current values at the peak in each particular section were exchanged by the average current of the previous section. The capacitive peaks naturally manifested at times at which the clamping potential changed (corresponding to pulse protocol). Therefore, the default cutting times were set to 30 ms, 80 ms, 1.6 s and 1.7 s. The last two times had to be adjusted in the script as the transients were slightly shifted from the reference points.

3.1.2 Voltage Pulse Protocol

The exact same pulse protocol was used for each dataset. Therefore, it was introduced in the modelling process as well. Timing and corresponding clamping potentials of the pulse protocol are summarized in the tables 8 and 9 in the appendix. The pulse protocol is further referred to as VPP in this thesis. A distinct clamping potential is denoted by V_C and the actual pulse is referred to as V_P .

The voltage was initially clamped to 0V at 0s and subsequently to $-60mV$ at 30ms (holding potential). Then the pulse V_P was applied from 80ms to 1600ms. After the pulse, the clamping potential was subsequently set back to $-60mV$ at 1600ms, followed by 0V at 1700ms. The pulse V_P was varied from -120 to $110mV$ with a $10mV$ incremental step size. Figure 16 shows the time course of the clamping potentials.

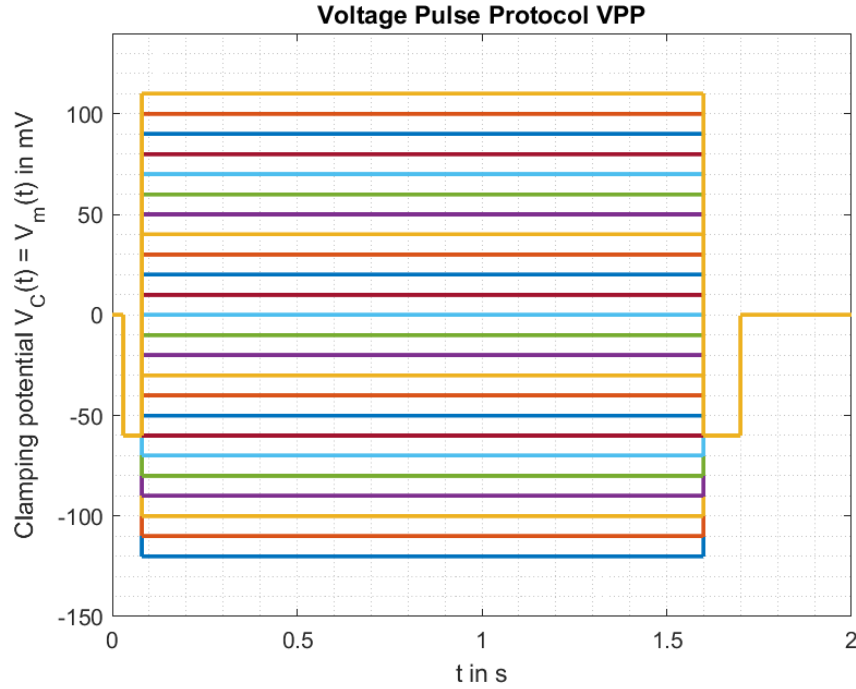


Figure 16: Clamping potentials of VPP over time.

3.2 Ion Channel Modelling

Different mathematical models for ion channels are known. Some modelling approaches are based on Hodgkin-Huxley formulations (thermodynamic models), others are based on Markov Models. [52]

A comparison of these specific modelling approaches is provided in [53].

Markov models comprise a series of advantages over other modelling techniques as they provide a flexible framework and gating kinetics can be replicated very precisely [53]. A publication from 2021 reported that the A-549 whole-cell current could be successively replicated by ion channel modelling using Markov Models [54]. This particular modelling approach was chosen for MCF-7 and MCF-10A cells as well.

Please note that the terms Markov Models, Hidden Markov Models and kinetic models are used interchangeably in this thesis in context of ion channel modelling due to reasons of consistency with cited literature.

3.2.1 Hidden Markov Model Approach

Markov Models are probabilistic models and represent gating of ion channels as sequences of random state changes. One or more of these states represent the channel to be open (O), closed (C) or inactivated (I) and in an ideal model, each state would correlate with a distinct channel conformation. Markov Models of single channels are principally stochastic in their basic form, causing the microscopic current to fluctuate. In case of a large population of identical channels, these fluctuations of single channel currents will average, resulting in a relatively smooth macroscopic current. It is then approximatively correct to consider these models deterministically. Importantly, state transitions in these models are exclusively dependent on currently occupied states and not on histories of occupations (*Markovian property*). [52]

These models can be illustrated with kinetic schemes [52]. A kinetic scheme is a weighted and directed graph, consisting of states and transitions [55]. The transitions are parametrized by transition rates [52], [55].

Each state in the model corresponds with a probability of occupation [56]. In this thesis, the state probability $P_S(t)$ is defined as the probability that a state S is occupied at certain time t . In terms of ion channel models, S is replaced by O , C or I accordingly.

Principally, two variants of modelling a macroscopic current exist: a pure stochastic approach and an approximative deterministic approach. While the stochastic approach means to summarize the distinctly simulated currents of all channels of a population, the deterministic approach means to calculate and scale the expected value of the current by the size of the population. This reduces computational costs under the assumption that current fluctuations vanish at a sufficiently large amount of channels N_C . [52]

3.2.2 Channel Modelling and Implementation

Using the kinetic model of $K_{V11.1}$ introduced by [57], the modelling approach of a single channel in the MCF-7 model is illustrated in the following. Figure 17 shows the concerning five-state model, comprising three C-states, one I- and one O-state.

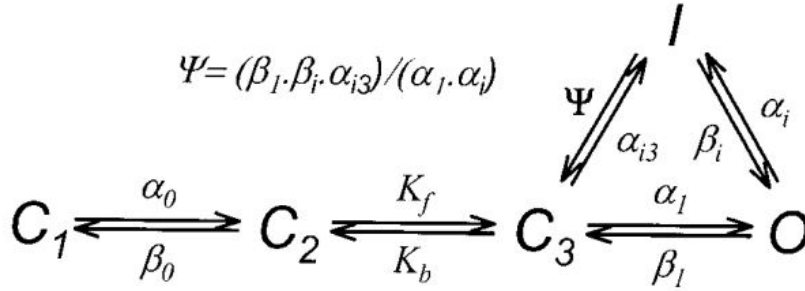


Figure 17: Kinetic model of $K_{V11.1}$ introduced by [57]. The nodes C_1 to C_3 denote the closed states, O is the open state and I is the inactivated state of the model. The transition rates α_0 , β_0 , α_1 , β_1 , α_i , β_i , α_{i3} and Ψ are voltage-dependent, while the transition rates K_f and K_b are constant. [57]

The time evolution of the state probability $P_{C_1}(t)$ is defined as shown in equation 8 [54]. In this equation, $P_{C_1}(t)$ and $P_{C_2}(t)$ represent the corresponding state probabilities, while α_0 and β_0 denote the transition rates at the concerning node with respect to figure 17.

$$\frac{d}{dt}P_{C_1}(t) = P_{C_1}(t) \cdot (-\alpha_0) + P_{C_2}(t) \cdot \beta_0 \quad (8)$$

Logically, the time evolution of each state in the model is defined analogously to this, resulting in a system of ordinary differential equations [55]. According to [55], a convenient notation is shown in equation 9, where \mathbf{P} is the probability vector and \mathbf{Q} is the generator matrix of the Markov Model, holding all transition rates of the system.

$$\boxed{\frac{d}{dt}\mathbf{P} = \mathbf{Q}\mathbf{P}} \quad (9)$$

Transition probabilities between states can be approximated by multiplying each transition rate with a sufficiently small time interval T_S [55]. Given a transition rate α , the corresponding transition probability can be calculated by $\alpha \cdot T_S$ then. Introducing a transition probability matrix (corresponding with T_S) is convenient for calculations in modelling [58].

With respect to [55], the numerical solution of the probability P_{C_1} at time $t + T_S$ of the model by [57], denoted as $P_{C_1}(t + T_S)$, can be calculated using equation 10. This simplification was also used in the A-549 whole-cell modelling approach [54].

$$P_{C_1}(t + T_S) = P_{C_1}(t) \cdot (1 - \alpha_0 \cdot T_S) + P_{C_2}(t) \cdot \beta_0 \cdot T_S \quad (10)$$

In the end, the initial occupancy of states and the transition probabilities of the model allow a complete description of the system, both for transients and in steady-state. The current probability of occupancy can be computationally calculated in a stepwise manner, using transition probabilities and recent state probabilities. [55]

The total open probability $P_O(t)$ of a single channel is defined as the sum of state probabilities of all open states and can be calculated by $P_O(t) = \sum_i P_{O,i}(t)$ with $P_{O,i}(t)$ denoting the state probability of an open state and i varying from 1 to the total number of open states [54].

According to [55], the macroscopic current $I(t)$ can be calculated using equation 11, where the parameter N_C denotes the number of single channels, g represents the single channel conductance and E_R denotes the reversal potential of the ion species [55]. As voltage-gated potassium channels are modelled in this thesis, the open probability $P_O(t)$ is naturally dependent on V_m as well. With respect to the derived equation in [55], the sign of the current $I(t)$ in equation 11 was changed for reasons of consistency.

$$I(t) = N_C \cdot P_O(t) \cdot g \cdot (V_m - E_R) \quad (11)$$

Equation 11 illustrates that voltage-gated single channel currents are principally dependent on voltage in two ways. Firstly, the voltage has an impact on channel gating, i.e. on the open probability $P_O(t)$.

Secondly, the voltage difference $V_m - E_R$ defines the driving force for the ionic current in case of $P_O(t) > 0$. In all cases, the condition $P_O(t) > 0$ must hold so that a current can flow. There is only one case in which the current equals zero nevertheless, namely when the membrane potential V_m equals the reversal potential E_R .

In this thesis, the term single channel current refers to microscopic current. This particular current can be calculated analogously, using equation 11 and $N_C = 1$. In this context the macroscopic current $I(t)$ can be interpreted as the single channel current $i(t)$ scaled by the number of channels N_C . This correlation is illustrated in equation 12.

$$I(t) = i(t) \cdot N_C \Rightarrow i(t) = P_O(t) \cdot g \cdot (V_m - E_R) \quad (12)$$

In equation 11, the deterministic approach can be seen, as the calculated open probability of a single channel $P_O(t)$ is assumed to be the fraction of channels in a population being open, in case of modelling a macroscopic current [56]. This approximative approach is described mathematically in equation 13, where N_C denotes the number of channels of the population, $n_O(t)$ the number of open channels at a certain time t and $P_O(t)$ the total open probability of the model at a certain time t .

$$N_C \gg 1 \Rightarrow P_O(t) \approx \frac{n_O(t)}{N_C} \quad (13)$$

Following the deterministic approach proposed by [54], a system matrix **A** for state-space representation of single channel models was introduced, holding the transition probabilities of the kinetic model. Transition rates were directly adopted from the corresponding literature and the fundamental assumption was made that kinetic models have universal validity throughout all cells. The resulting input-free, discrete-time state-space model is shown in the equations 14 and 15 [54]. Note, that the vector product $\mathbf{C}\mathbf{P}[n]$ extracts and summarizes the open probabilities for calculating the total open probability $P_O[n]$ via a dot product. In equation 14, **P** is a vector, that holds the state probabilities and **A** is the system matrix of the state-space model that holds the transition probabilities. The vector **C** in equation 15 maps the total open probability in a scalar $P_O[n]$ (output of the model).

For this purpose, the vector components of \mathbf{C} are zeros for non-open states and ones for open states.

$$\mathbf{P}[n + 1] = \mathbf{A}\mathbf{P}[n] \quad (14)$$

$$P_O[n] = \mathbf{C}\mathbf{P}[n] \quad (15)$$

Using a state-space model for single channel modelling as proposed by [54] was convenient as built-in MATLAB functions simplified simulating the system responses. Therefore, the single channel model was firstly transferred to a discrete-time state-space model using the built-in function *ss* with a sampling time $T_{S,Model}$. Then the response of the system could be simulated using the built-in function *lsim*. The sampling time $T_{S,Model}$ was the same as the one used for calculating the transition probabilities in the system matrix \mathbf{A} . Equivalent to the implementation in [54], a global sampling time of $T_{S,Model} = 5 \cdot 10^{-7} s$ was used.

Each single channel model was implemented in a separate function, returning the discrete-time state-space model of the channel. This implementation style was adopted from [54]. A consistent naming convention was used for these functions, clearly denoting the channel and hinting the literature from which the kinetic model was adopted. The architecture of these functions was principally identical for all single channel models. As only voltage-gated potassium channels were modelled, transition rates were either constant or dependent on V_m . To be able to retrace the implementation, both adopted transition rates and calculated transition probabilities were defined in the single channel functions. The functions also held the emission matrices for simulating the stochastic single channel current responses (Hidden Markov Model).

Referring to equation 11, both single channel conductances g and reversal potential E_R had to be determined for modelling and simulation. The single channel conductances were adopted from literature. The reversal potential of potassium E_K was calculated using the Nernst equation. The K^+ concentrations used in the measurements were published in [59].

With the provided values on solution compositions and equation 4, the reversal potential of potassium could be calculated as follows.

Intra- and extracellular potassium concentrations were adopted from [59] and given by $c_K^i = 141mM$ and $c_K^e = 2mM$. A temperature of $T = 20\text{ }^\circ\text{C}$ was assumed.

$$E_K = \frac{R \cdot T}{z_K \cdot F} \cdot \ln \frac{c_K^e}{c_K^i} \approx \frac{8.3145 \frac{J}{mol \cdot K} \cdot 293.15K}{1 \cdot 9.6485 \cdot 10^4 \frac{C}{mol}} \cdot \ln \frac{2mM}{141mM} \approx \underline{\underline{-107.5mV}}$$

The Simulation of single channel models was implemented in the function *model_single_channel_simulation.m*. The implementation allowed the voltage pulse protocol for the simulation to be freely chosen. Depending on the literature from which the kinetic models were adopted, the initial state vectors $\mathbf{P}[0]$ were chosen accordingly. Channel gating was considered to be exclusively dependent on membrane potential and on time. Corresponding simulation results of single channel models are shown in chapter 4.2.

In contrast to the deterministic modelling approach using state-space models, channel responses were also stochastically simulated for illustration purposes and comparison during the modelling process, using Hidden Markov Models. The stochastic simulation of channel responses was implemented in the function *model_hmm_simulation.m*, using the built-in function *hmmgenerate*.

In this context, the macroscopic current response of the $K_V7.1$ model was simulated for illustration purposes using both state-space model and Hidden Markov Model approach. The current responses were simulated for $V_P = 60\text{ mV}$ during 0 to 1.5 s with respect to VPP. A channel expression level of $N_C = 175$ was used (optimized channel expression level from the MCF-7 model). The macroscopic current responses are shown in chapter 4.3.

3.2.3 Cell Modelling

The primary objective of this thesis was the implementation of a first approach, modelling the potassium current in MCF-7 and MCF-10A cells. For this, kinetic models of expressed voltage-gated potassium channels should be used for an approximative modelling approach. Each channel was modelled using an appropriate kinetic model from literature. These models were then integrated in cell models and channel expression levels were optimized via a particle swarm optimization using provided experimental data [54]. Based on this principal line of thought, the cell modelling approach is outlined in the following.

The presented correlations in the single channel domain appear to be simple but as soon as the whole cell is approached, many degrees of freedom add at once and tremendously increase the overall complexity of the system. The basic correlation of voltage and current remains but many factors are now influencing the transient and stationary behaviour of the system.

For the general case that all macroscopic currents are taken into account, the whole-cell current can be principally defined by equation 16. In this equation, $I_{\tilde{\zeta},i}(t)$ denotes a macroscopic current that might be gated by voltage, ligands, Ca^{2+} or any other possible factor represented by the variable $\tilde{\zeta}$. Both whole-cell current $I_{tot}(t)$ and the macroscopic currents $I_{\tilde{\zeta},i}(t)$ are naturally dependent on time.

$$\boxed{I_{tot}(t) = \sum_i I_{\tilde{\zeta},i}(t)} \quad (16)$$

As explained, the current of a population of voltage-gated ion channels can be calculated via equation 11, using an appropriate kinetic model. By indexing the macroscopic currents with i , the total membrane current that is conducted by voltage-gated channels can be calculated using equation 17.

In equation 17, $I_{V_m,tot}(t)$ is the voltage-gated whole-cell current, $I_{V_m,i}(t)$ is a macroscopic current, maintained by an ensemble of voltage-gated channels of the same type (e.g. current maintained by $K_{V1.1}$) and $I_{tot}(t)$ is the whole-cell current of the cell.

$$I_{V_m,tot}(t) = \sum_i I_{V_m,i}(t) < I_{tot}(t) \quad (17)$$

Only voltage-gated potassium channels were considered in this thesis. Therefore, $I_{V_m,tot}(t)$ in equation 17, limited to potassium currents, was assumed to be approximatively reflecting the whole-cell current $I_{tot}(t)$. This is mathematically expressed in equation 18. Logically, the more populations are added, the more this approximation will reflect the whole-cell current.

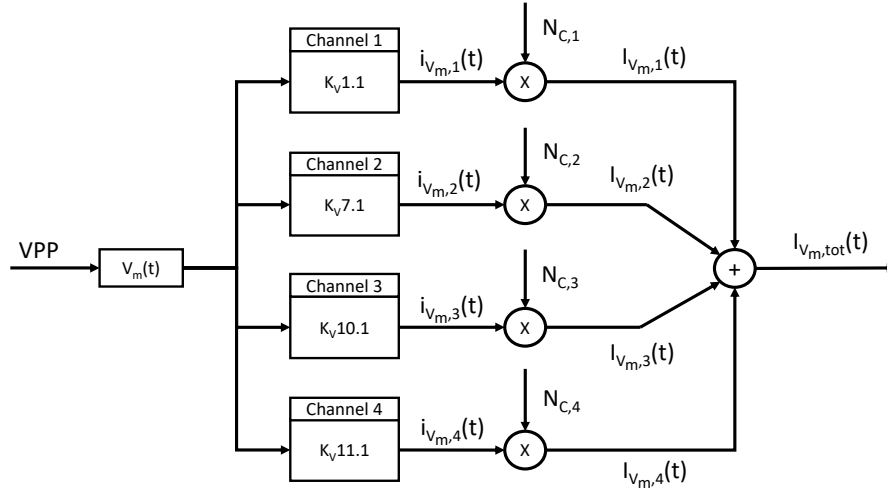
$$I_{tot}(t) \stackrel{!}{=} \sum_i I_{V_m,i}(t) = \sum_i i_{V_m,i}(t) \cdot N_{C,i} = I_{V_m,tot}(t) \quad (18)$$

The idea was to integrate K_V -channels based on their reported expression and subsequently optimize their channel expression levels in a way that the sum of considered macroscopic currents would reflect the whole-cell current [54]. Each cell model was composed of four single channel models per default, based on the results of the literature researches presented in chapter 4.1. The cell models can be graphically illustrated as signal flow diagrams as shown in the figures 18a and 18b.

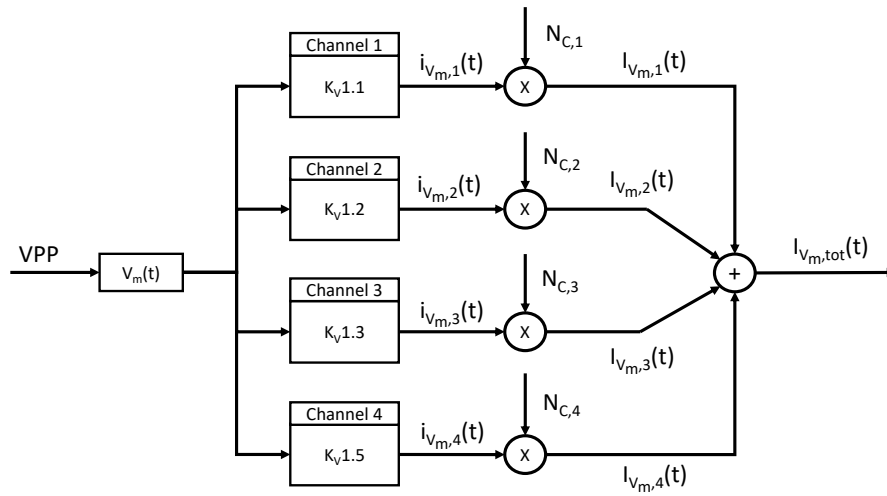
A particle swarm optimization was used for solving this optimization problem by minimizing the RRMSE of measured and simulated data, as done in the publication by [54]. According to [54], the relative root-mean square error RRMSE is defined as shown in equation 19, where $I_{tot}(t)$ denotes the whole-cell current from the measurement data and $I_{V_m,tot}(t)$ denotes the modelled whole-cell current of voltage-gated potassium channels. The optimization was carried out for all preprocessed whole-cell currents, i.e. for all corresponding pulse potentials in VPP.

$$RRMSE = \sqrt{\frac{\sum (I_{V_m,tot}(t) - I_{tot}(t))^2}{\sum I_{tot}(t)^2}} \quad (19)$$

3 Methods



(a) MCF-7 cell model



(b) MCF-10A cell model

Figure 18: Signal flow diagrams of cell models.

A particle swarm optimization (PSO) is principally based on the information exchange about local and global best values when a swarm of particles iteratively evolves in context of solving an optimization problem. The performance of each particle can be determined by the so called individual and social perspectives. The individual perspective refers to the performance of each single particle, while the social perspective refers to the performance of the swarm as a whole. These perspectives are combined for the prediction in each iteration in order to calculate the best value updates for the next iteration. [60]

The optimization was implemented in the function *model_optimization* and was partially based on published source code for the A-549 cell model by [54]. Simulated single channel currents and measured whole-cell currents were put into datasets and expression levels were subsequently optimized using the built-in function *particleswarm* from the *global optimization toolbox*. The function tolerance was chosen by 10^{-6} and the maximum amount of iterations was set to 500. The implemented optimization could be used for optimizing four channel expressions per default. Alternatively, three channel expressions in the MCF-10A model could be optimized when the flag for reduced dataset usage (RDU) was set (bypassing $K_{V1.2}$). As four K_V -channels were used per cell model, the optimization problem principally had four degrees of freedom defined by $N_{C,1}$, $N_{C,2}$, $N_{C,3}$ and $N_{C,4}$. The constraints for the MCF-10A model were defined without prior knowledge. In case of the MCF-7 model, the expression level of $K_{V1.1}$ was estimated based on whole-cell patch-clamp measurement results published in [48], where approximately 65 % of the MCF-7 whole-cell current was reported of being sensitive to α -DTX during a measurement duration of 200 ms, after applying voltage pulses up to 60 mV. α -DTX is a selective blocker of $K_{V1.1}$, $K_{V1.2}$ and $K_{V1.6}$ [10]. Only $K_{V1.1}$ was considered to be functionally expressed in MCF-7. The expression level of this channel was estimated by dividing 65 % of the mean value of the whole-cell current of the experimental data by the mean value of the single channel current of the $K_{V1.1}$ model (both corresponding with $V_P = 60mV$). The timespan of 80 to 280 ms was considered for this and the calculation resulted in approximately 65 channels. Based on this value, the constraints for $K_{V1.1}$ in terms of optimization were chosen by 60 and 70, allowing the parameter to settle in this range.

This calculation was carried out under the assumption that the whole-cell patch-clamp measurements in [48] and the provided experimental data for optimization were principally comparable and by additionally considering the strong inactivation of the modelled channel during the first 200 ms after applying a voltage pulse. A similar approach was used for choosing the constraints of $K_{V7.1}$. Based on published results of another measurement, astemizole was reported to block approximately 45 ± 12 % of the whole-cell current in MCF-7 when applying a 60 mV voltage pulse during a measurement duration of 200 ms [42]. Astemizole is known to block both $K_{V10.1}$ [42] and $K_{V11.1}$ [10], [47]. By assuming that this is also the case in the steady state of the provided experimental data and by additionally taking into account the steady state current maintained by $K_{V1.1}$, the constraints for $K_{V7.1}$ were concluded accordingly. The timespan of 0.8 to 1.4 s was considered as steady state in this context. Firstly, the collectively maintained current by $K_{V1.1}$ and $K_{V7.1}$ was considered to reflect 43 % to 67 % of the whole-cell current of the experimental data, correlating with $V_p = 60mV$. After subtracting the macroscopic current of $K_{V1.1}$, using the previously calculated channel expression level (65), the constraints of $K_{V7.1}$ were calculated and resulted in approximately 120 and 222. For the sake of completeness it should be noted at this point that it was unknown in which phases of the cell cycle the five MCF-7 and MCF-10A cells were, when they were measured. In the tables 3 and 4, the constraints for optimizing the cell models are shown. The start and stop times of both optimizations were chosen by 20 ms and 1.8 s as the same timing was used in all experiments. The parameters $N_{C,i,min}$ and $N_{C,i,max}$ denote the constraints of the solver with respect to the optimization problem for each single channel model. The single channel models are enumerated using the index i .

i	Name	$N_{C,i,min}$	$N_{C,i,max}$
1	-	1	1
1	$K_{V1.1}$	60	70
2	$K_{V7.1}$	120	222
3	$K_{V10.1}$	5	350
4	$K_{V11.1}$	5	350

Table 3: Constraints of MCF-7 model

i	Name	$N_{C,i,min}$	$N_{C,i,max}$
1	-	1	1
1	$K_{V1.1}$	1	100
2	$K_{V1.2}$	1	100
3	$K_{V1.3}$	1	100
4	$K_{V1.5}$	1	100

Table 4: Constraints of MCF-10A model

As the measurement data and single channel simulations were sampled using different sampling frequencies ($f_{S,Measure}$ versus $f_{S,Model}$), the simulation results had to be downsampled because of the chosen values which are shown in the equation below.

$$f_{S,Measure} = 10kHz < f_{S,Model} = 2MHz$$

This was implemented using the built-in function *downsample* as the down-sampling factor was an integer value.

The downsampling factor K_{DS} could be calculated using equation 20 in which $f_{S,Measure}$ denotes the sampling frequency of the measurements and $f_{S,Model}$ denotes the sampling frequency that was used in simulation.

$$K_{DS} = \frac{f_{S,Model}}{f_{S,Measure}} = \frac{2MHz}{10kHz} = 200 \quad (20)$$

It must be noted that the optimization for some channels resulted in very low expression levels ($N_{C,i} \geq N_{C,min}$ versus $N_{C,i} \gg N_{C,min}$, with $N_{C,min}$ denoting the lower constraint in optimization). The deterministic approach for these single channel currents was considered to be approximately correct during modelling as the partial currents maintained by these low channel expressions were assumed to be small in comparison with the macroscopic currents of the other (typically up-regulated) channel populations in the cell model.

The optimization results of the cell models and the current responses of the optimized cell models are shown in chapter 4.6. Additionally, the current composition of $I_{V_m,tot}(t)$ in each cell model is illustrated for two distinct pulse potentials.

3.2.4 Gating Analysis

For investigating the individual contribution of integrated single channel models in the cell models, steady state open probabilities were analysed. The steady state during the voltage pulse V_P was focussed for gating analysing as literally all information on switching dynamics was lost because of uncompensated capacitive transients in the experimental data. For this reason, the mean open probabilities of single channel models in steady state $P_{O,SS}(V_P)$ were calculated for each pulse potential V_P and plotted accordingly. Subsequently, the total open probability for each cell model in steady state $P_{O,tot,SS}(V_P)$ (normalized by the number of integrated single channel models) was calculated for each pulse potential V_P and plotted against the averaged steady state current $I_{tot,SS}(V_P)$ of the experimental data. The corresponding figures for analysing the gating in each cell model are presented in chapter 4.5.

The mean open probabilities $P_{O,SS}(V_P)$ were calculated by averaging the resulting open probability of the single channel responses for each pulse potential V_P from 0.4 s to 1.4 s (this timespan was considered to be the steady state in this context). The total open probability in steady state $P_{O,SS,tot}(V_P)$ was calculated by summation of the steady state open probabilities for each pulse potential V_P , normalized by 4: $P_{O,SS,tot}(V_P) = 0.25 \cdot \sum_i P_{O,SS,i}(V_P)$. The whole-cell current in steady state $I_{tot,SS}(V_P)$ was calculated by averaging this current from 0.4 s to 1.4 s with respect to each pulse potential V_P .

3.3 Kinetic Models of K_V -channels

Based on the literature researches on voltage-gated potassium channel expressions in MCF-7 and MCF-10A (chapter 4.1), kinetic models for $K_{V1.1}$, $K_{V1.2}$, $K_{V1.3}$, $K_{V1.5}$, $K_{V7.1}$, $K_{V10.1}$ and $K_{V11.1}$ were needed. In the following, kinetic models from literature are introduced and briefly discussed on occasion. The corresponding results of single channel simulations of the chosen models are presented in chapter 4.2.

3.3.1 Kinetic Model of $K_{V1.1}$

Drug effects of fluoxetine (flu) on $K_{V1.1}$ were studied in a previous publication, using oocytes of *Xenopus laevis*. One of the main findings of this study was the significant decrease of potassium current when using Flu in voltage-clamp experiments (at 19 to 23 °C). As part of this publication, a quasi-linear kinetic model with seven states was derived, including four C, one O and two additional Flu-dependent states. [61]

Another study investigated the impact of glycosylation on $K_{V1.1}$ channels in Chinese hamster ovary (CHO) cells and reported evidence of modified channel functionality in terms of altered gating kinetics. Three kinetic models were introduced (C5-Q, ZHA-Q and ZHA-Q-elec) and it was shown, that the ZHA-Q-elec model fitted experimental data the best (e.g. I-t-curve). Worth mentioning is, that slow C-type inactivation of $K_{V1.1}$ in CHO cells was reported (at 23 to 25 °C). [62]

Another kinetic model was introduced in order to investigate the effects of syntaxin 1A (syx) on $K_{V1.1}$ in *Xenopus* oocytes. The model comprised several C-states, including a fully occupied initial state. The O-states of the model were based on observations in electrophysiological measurements where a fully conductive state and two sub-conductance states could be determined. The model was not capable of replicating inactivation. [63]

A neural kinetic model, derived from the Frankenhaeuser-Huxley model, was published as part of an investigation on K_V blockers [64].

As pointed out by [65], inactivation in previously introduced Markov models of $K_{V1.1}$ was either not or not sufficiently enough considered. Based on the electrophysiological data of $rK_{V1.1}$ in CHO cells, both [53] and [65] presented a more sophisticated Hidden Markov Model approach for $K_{V1.1}$. These newer models from [53] and [65] resolved gating kinetics more precisely than the previously presented kinetic models and were particularly capable of modelling the inactivation of the channel. On the downside, both models were parametrized for current curves at 35 °C [53], [65]. This was problematic as the patch-clamp measurements of the provided data for the optimizations were performed at room temperature.

The model introduced by [65] was implemented for the $K_V1.1$ single channel model. Although this model was parametrized for higher temperatures, it nicely replicated the inactivating kinetics in contrast to the model by [62] for example. Transition rates and single channel conductance (8.7 pS) were completely adopted from [65]. As a first approach, temperature differences were neglected. The model by [65] is shown in figure 19.

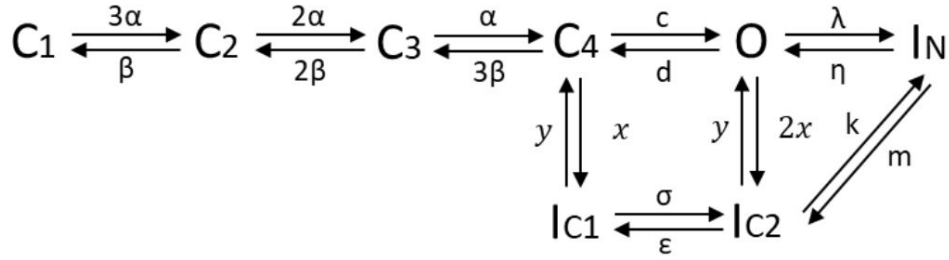


Figure 19: Kinetic model of $K_V1.1$ introduced by [65]. The kinetic model comprises four closed states C_1 to C_4 , three inactivated states I_N , I_{C1} and I_{C2} and one open state O [65].

3.3.2 Kinetic Model of $K_V1.2$

A 16-state kinetic model introduced by [66] in 2012 was implemented as a first approach for modelling the gating kinetics of $K_V1.2$.

The kinetic scheme comprised 14 C-states and one final O-state. Additionally, another state ($O:B^+$) could be reached from the open state and the corresponding transition was dependent on the intracellular NMG^+ (N-methyl-D-glucamine) concentration. [66]

This particular state was omitted as the intracellular NMG^+ concentration, denoted by $[B^+]$ in the kinetic scheme, was considered to be zero. By doing this, the state was virtually cut from the kinetic scheme as the resulting transition probability from O to $O:B^+$ resulted to be zero as a consequence. In harmony with considerations in [66], the simulated single channel current response of the implemented model did not show any inactivation.

3 Methods

This was not in complete harmony with the noticeable inactivation of $rK_{V1.2}$ channels at 25 °C in [67]. The lacking inactivation of the model was considered to be approximately correct as a first approach in this thesis.

An alternative model introduced by [68] was implemented but simulations resulted in unforeseeable gating behaviour for parts of the used pulse protocol. The model was principally capable of replicating inactivation but for higher voltages, the simulated single channel current responses returned to almost zero Amperes after the initial peak. This was caused by the fact that the model got trapped in closed states at higher voltages. For this reason, the model by [68] was not further considered as an alternative for the modified model by [66] and the model by [66] was the only single channel model that was considered for $K_{V1.2}$ in this thesis.

The single channel conductance (18 pS) was adopted from [Grissmer S. et al. Pharmacological characterization of five cloned voltage-gated K⁺ channels, types Kv1.1, 1.2, 1.3, 1.5, and 3.1, stably expressed in mammalian cell lines. 1994 quoted in 69]. Figure 20 shows the kinetic scheme by [66] used for modelling $K_{V1.2}$.

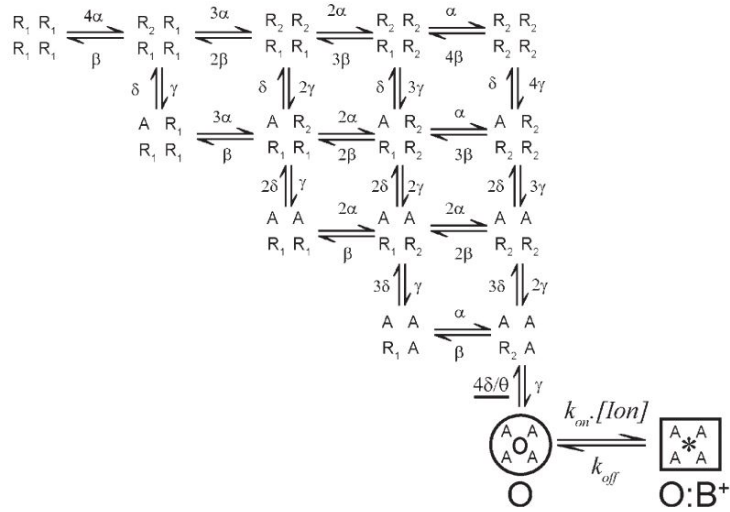


Figure 20: Kinetic model of $K_{V1.2}$ introduced by [66]. The model is composed of 14 closed states and the final open state O . The additional state $O : B^+$ can be exclusively reached from the open state via an NMG^+ -dependent transition rate as indicated in the kinetic scheme. [66]

3.3.3 Kinetic Model of $K_V1.3$

A linear, seven-state kinetic model for $K_V1.3$ was introduced in 2014. The model was parametrized using experimental data from transfected HEK293 cells and was capable of replicating literally all important gating kinetics. The electrophysiological measurements for this were carried out at room temperature. [70]

For these reasons, the model by [70] was implemented as single channel model for $K_V1.3$. The single channel conductance (13 pS) was adopted from a publication, in which *Xenopus* oocytes were measured at room temperature [71]. Figure 21 shows the kinetic scheme by [70] used for modelling $K_V1.3$.

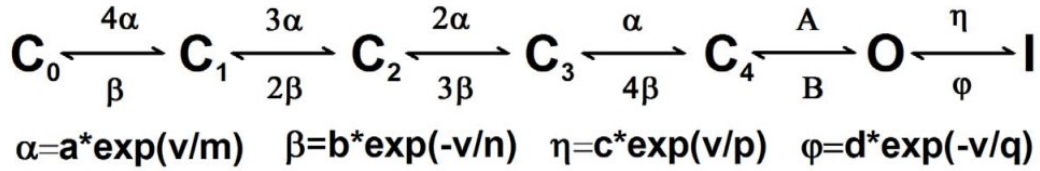


Figure 21: Kinetic model of $K_V1.3$ introduced by [70]. The linear model comprises five closed states C_0 to C_4 , one open state O and one inactivated state I [70].

3.3.4 Kinetic Model of $K_V1.5$

Based on the Ramirez-Nattel-Courtemanche (RNC) model, a kinetic model for $K_V1.5$ was developed in 2010. The RNC model is basically a Hodgkin-Huxley-like model and used for modelling canine action potentials (non-human model). The subsequently developed, linear Markov Model was intended to be used for studying drug effects on these action potentials. The model was parametrized using the original RNC model results. No C-type inactivation was considered in the kinetic model. Without drug-dependent states, the model comprised four C-states and one O-state. [72]

Another kinetic model for $K_{V1.5}$ was introduced in 2017. The model comprised four C-states, one O-state and one I-state. The model was originally developed for investigating drug binding effects on $K_{V1.5}$ gating and the parametrization was carried out by using experimental data of atrial myocytes. [73]

Fortunately, also a drug-free model was provided by [73]. As the model by [73] was considered to replicate gating more precisely after comparison with the previous one, the model by [73] was implemented for $K_{V1.5}$. The single channel conductance (8 pS) was adopted from [74]. Figure 22 shows the kinetic scheme by [73] used for modelling $K_{V1.5}$.

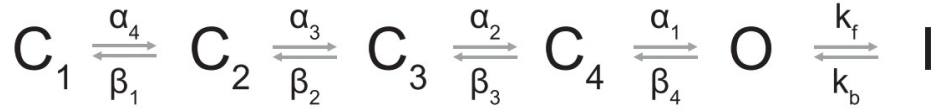


Figure 22: Kinetic model of $K_{V1.5}$ introduced by [73]. The kinetic model consists of four closed states C_1 to C_4 , one open state O and one inactivated state I [73].

3.3.5 Kinetic Model of $K_{V7.1}$

Electrophysiological recordings of $K_{V7.1}$ expressed in oocytes of *Xenopus laevis* showed that depolarization triggers fast activation of the channel, followed by a delayed settling in an inactivated state [75].

Repolarization of the channel resulted in a delayed recovery from this inactivated state. This was shown to manifest as a hook in the current course. The shape of the hook could be influenced by the length of the preceding depolarization pulse. [75]

Higher preceding pulses were shown to increase the size of the current hook as well [76].

It was suggested that activation and inactivation are linked to each other. A linear five-state kinetic model with two O-states, two C-states and a voltage-independent I-state was introduced, reproducing the reported kinetics of the channel. [75]

Another study suggested that the unique inactivation of $K_V7.1$ is caused by the conformational change of the voltage sensor from intermediate to activated, which slightly reduces the open probability of the pore, resulting in the previously described inactivating behaviour. This study introduced a six-state kinetic model that was said to be able to replicate the discussed gating behaviour. [76]

The kinetic model introduced by [75] was selected for the $K_V7.1$ channel. It provided a simple and robust model and replicated the most important characteristics of $K_V7.1$. The single channel conductance (1.8 pS) was adopted from [47]. Figure 23 shows the kinetic scheme by [75] used for modelling $K_V7.1$.

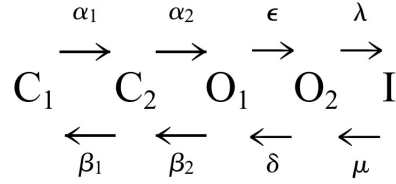


Figure 23: Kinetic model of $K_V7.1$ introduced by [75]. The linear model comprises two closed states C_1 and C_2 , two open states O_1 and O_2 and one inactivated state I [75].

3.3.6 Kinetic Model of $K_V10.1$

Different kinetic models were introduced, quantitatively describing gating of $K_V10.1$ by using experimental data. Four kinetic models with different topologies were developed. Five- and six-state kinetic models were found to replicate channel kinetics insufficiently. Ten- and twelve-state kinetic models were considered as more suitable approaches, replicating the general current response of the channel more realistically and precisely. Both (ten- and twelve-state) models comprised I-states paired to each O- and C-state in the kinetic scheme. The introduced twelve-state model was exclusively capable of reproducing the slower phase of activation, which has been observed beforehand. The twelve-state model also had the smallest fit error compared to the other models. [77]

The twelve-state kinetic model introduced by [77] was implemented for $K_{V10.1}$. As specified, the initial state probabilities of C_0 and I_0 were set to 0.5 each in simulation [77]. Simulations of the model resulted in similar current responses. No exact value for the single channel conductance could be found in literature. Based on the value provided by [Pardo LA et al. Cell cycle-related changes in the conducting properties of r-eag K⁺ channels. 1998 quoted in 69], the conductance was assumed to be 1 pS as a first approach. Figure 24 shows the kinetic scheme by [77] used for modelling $K_{V10.1}$.

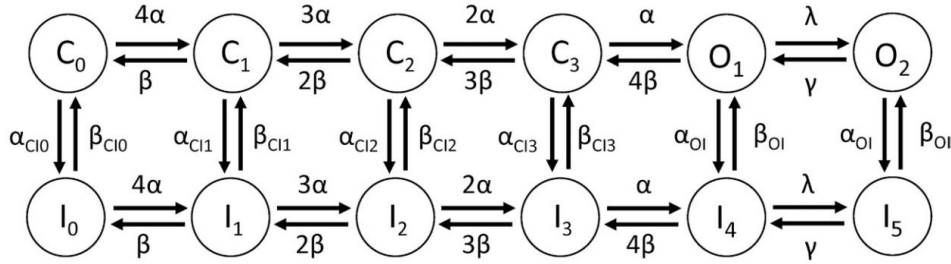


Figure 24: Kinetic model of $K_{V10.1}$ introduced by [77]. The kinetic model is composed of four closed states C_0 to C_3 , six inactivated states I_0 to I_5 and two open states O_1 and O_2 . Each closed and open state is paired with a corresponding inactivated state. [77]

3.3.7 Kinetic Model of $K_{V11.1}$

A variety of different kinetic models were developed for $K_{V11.1}$ [78], [79].

It has been shown that these channels are activated around -40 mV and the current maximizes at voltage levels between -20 mV and 0 V. Due to inward rectification, the current decreases for higher voltages. $K_{V11.1}$ channels are also known to show a transient peak in a certain voltage range. [80]

One of the first modelling approaches was based on measurements in oocytes and the publication suggested a five-state kinetic model [80]. This approach was an expansion of a previously published model and included inactivation from the final closed state [79]. As reviewed by another study, properly parametrized five-state models were able to replicate the characteristic transient peak in the current response of the channel [78].

The review of [78] suggested that $K_{V11.1}$ is best modelled with three C-states, combined with one O- and one I-state. A comparison of kinetic models in [78] revealed the five-state kinetic model by [57] as potent for replicating $K_{V11.1}$ channel kinetics. The topologies of the kinetic models by [80] and [57] are basically identical. In both models the inactivated state can be reached either from the last C- or the O-state. This is the main difference to the linear model proposed by [81] in which the inactivated state can only be reached via the open state.

Due to its rather simple topology and based on the comprehensive review by [78], affirming its correctness in gating behaviour, the model introduced by [57] was used for modelling $K_{V11.1}$. According to [57], the model was parametrized for physiological temperature. As it was done for the $K_{V1.1}$ model, temperature differences were neglected for this first approach. The parameters of the model were adopted from the review by [78]. Note that the membrane potential V_m of the transition rates in [78] was meant to be inserted in millivolts. Simulation of the model with the same voltage-step protocol as it has been used in [78] resulted in similar current responses of the implemented model, confirming its correct implementation.

The simulated single channel currents could be shown to replicate the described behaviour well. The single channel conductance (2 pS) was adopted from [82].

Figure 25 shows the kinetic scheme by [57] used for modelling $K_{V11.1}$.

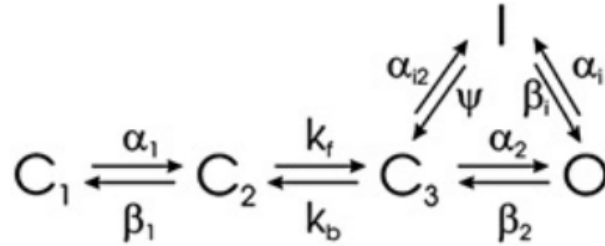


Figure 25: Kinetic model of $K_{V11.1}$ introduced by [57]. The kinetic scheme shows three closed states C_1 to C_3 , one open state O and one inactivated state I [57].

4 Results

4.1 K_V -Channels in MCF-7 and MCF-10A

The following four K_V -channels were considered to be functionally expressed in MCF-7 cells.

$K_{V1.1}$ is member of the shaker-related family K_V1 and encoded by the gene *KCNA1* [10], [47].

Using immunocytochemical methods, a study reported protein expression of subunits of $K_{V1.1}$ in the MCF-7 plasma membrane. While anti- $K_{V1.1}$ antibodies labelled the membrane, no labelling was reported for $K_{V1.2}$ and $K_{V1.3}$. The presence of fragments of the corresponding mRNA transcript was confirmed using RT-PCR. [48]

Another publication from 2010 reported presence of mRNA transcripts for $K_{V1.1}$, $K_{V1.2}$, $K_{V1.3}$ and $K_{V1.5}$ in MCF-7 cells [83]. The publication by [83] was exclusively available in Chinese. Therefore, no direct conclusion was derived from it in context of MCF-7 cell modelling. $K_{V1.2}$ and $K_{V1.3}$ were considered to be not functionally expressed in MCF-7, since the antibody labelling reported by [48] suggested this. Furthermore, the publication of [83] reported that the expression of $K_{V1.5}$ was much higher in MCF-10A than in MCF-7.

It has been elaborated that extracellular perfusion with TEA results in a striking reduction of current in whole-cell patch-clamp measurements. It was subsequently concluded that the whole-cell current of MCF-7 cells was mainly governed by potassium. $K_{V1.1}$ functionality in MCF-7 was experimentally confirmed by extracellular perfusion using α -DTX. This agent reduced the whole-cell current significantly as well but not as much as TEA. [48]

K_V1.1 is capable of forming heteromultimers by recruiting other members of the K_V1 family [47]. The formation of these structures in MCF-7 was reported to be unlikely as the protein expression of K_V1 family members in the plasma membrane suggested this and furthermore, observed current dynamics supported this consideration [48].

K_V7.1 is encoded by the gene KCNQ1 [10], [47].

A previous study identified fragments of this channel in the MCF-7 RNA using RT-PCR. Additionally, fragments of KCNE1, KCNE2 and KCNE3 (subunits which are known to co-assemble) were identified as well. Co-assemblies of KCNQ1 with KCNE1 and/or KCNE3 were considered as most likely in this publication. The presence of the protein product of KCNQ1 in MCF-7 was confirmed using Western blotting. [84]

Regulatory volume decrease (RVD) was observed and linked to the activity of K_V7.1. As experimentally examined, MCF-7 cells suffer an increase in size after being transferred from an isotonic into a hyposmotic solution. RVD regulates the cell volume by releasing the osmotic stress via K⁺-fluctuation over the membrane. [84]

The ability of RVD in MCF-7 cells could be influenced by specific blockers of K_V7.1, such as chromanol 293B and XE991, providing solid evidence that K_V7.1 is involved in RVD. Furthermore, the functional expression of K_V7.1 was confirmed as a consistent whole-cell current, sensitive to 293B, was measured in hyposmotic solution. [84]

K_V10.1 is encoded by the gene KCNH1 [10], [47].

A previous study identified mRNA transcript expression of K_V10.1 in MCF-7. Corresponding expression levels have been shown to be strongly dependent on the cell cycle as they were observed using semi-quantitative RT-PCR. It was shown that expression levels of K_V10.1 mRNA increased in G₀/G₁ phase, reached a maximum in G₁ phase and decreased again in S phase. [42]

A subsequent study confirmed that both mRNA of KCNH1 and the corresponding protein product are present in MCF-7 cells. Results of channel blocking experiments suggested that K_V10.1 is involved in proliferation in MCF-7. [49]

The varying expression levels of $K_{V10.1}$ in MCF-7 reported by [42] support this consideration.

$K_{V11.1}$ corresponds with the gene $KCNH2$ [10], [47].

Using Western blotting, protein expression of $K_{V11.1}$ in MCF-7 was determined in previous studies [49], [85]. $KCNH2$ mRNA expression in MCF-7 has been confirmed using RT-PCR [49].

Interestingly, experiments with E-4031 ($K_{V11.1}$ blocker) showed that $K_{V11.1}$ channels do not contribute to cell proliferation as the [3H]-thymidine incorporation showed no significant dependency. However, $K_{V11.1}$ channels in MCF-7 contribute to RVD, since the ability of performing regulatory volume decrease was significantly impaired in the presence of E-4031. Blocking via astemizole and imipramine resulted in similar outcomes. [49]

Regarding MCF-10A, a publication from 2010 reported the expression of a large part of the shaker-related family K_V1 in MCF-10A cells. Using RT-PCR, the presence of corresponding genes for $K_{V1.1}$, $K_{V1.2}$, $K_{V1.3}$ and $K_{V1.5}$ were determined in MCF-10A and MCF-7 cells. By Western Blotting, the presence of the protein of $K_{V1.5}$ was solidly confirmed in MCF-10A. [83]

The publication of [83] was available in Chinese only and the discussed reports and derivations were concluded with the help of an online translator (DeepL SE, Köln, Deutschland, www.deepl.com/translator). In a subsequent publication, the reported presences of mRNA transcripts of $K_{V1.1}$, $K_{V1.2}$, $K_{V1.3}$ and $K_{V1.5}$, as wells as the protein expression of $K_{V1.5}$ in MCF-10A cells were confirmed [50].

4 Results

Based on the literature research on K_V -channel expression, figure 26 shows the selection of K_V -channels used for modelling MCF-7 and MCF-10A.

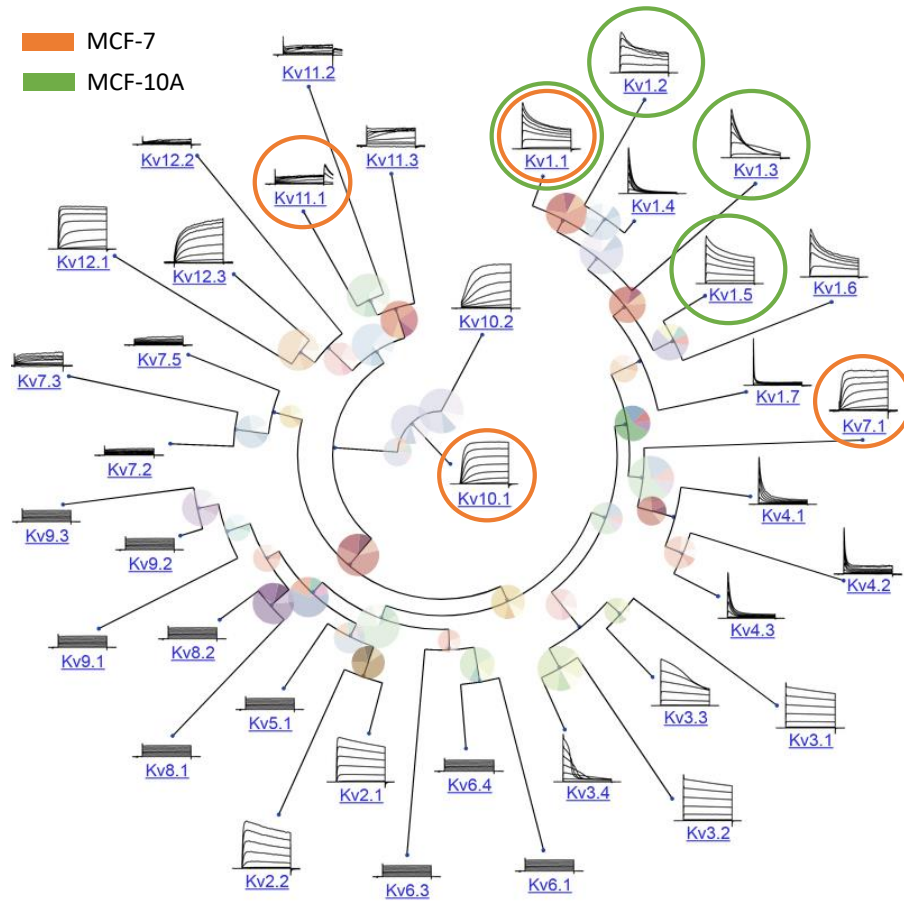


Figure 26: K_V -channel selection for cell modelling adapted from [86]. An overview of K_V -channels is shown, using channel names and their characteristic current responses. An encircled item denotes the integration of the channel in the corresponding cell model.

4.2 Single Channel Simulations

The figures 27 to 33 show the single channel current responses $i_{V_m}(t)$ of the single channel state-space models using the applied voltage pulse protocol. The corresponding pulse protocols are shown under each single channel current response. As the ensembles of curves comprise 24 traces each, no legends are shown for $i_{V_m}(t)$ and $V_m(t)$. Table 5 shows an overview of the simulated single channel current responses.

Channel	Figure	Page	Reference
$K_V1.1$	27	68	[65]
$K_V1.2$	28	69	[66]
$K_V1.3$	29	69	[70]
$K_V1.5$	30	70	[73]
$K_V7.1$	31	70	[75]
$K_V10.1$	32	71	[77]
$K_V11.1$	33	71	[57]

Table 5: Overview of single channel simulations

Single channel current response of ch- $K_V1.1$ -Langthaler2022 ($g = 8.7$ pS, $E_K = -107.5$ mV)

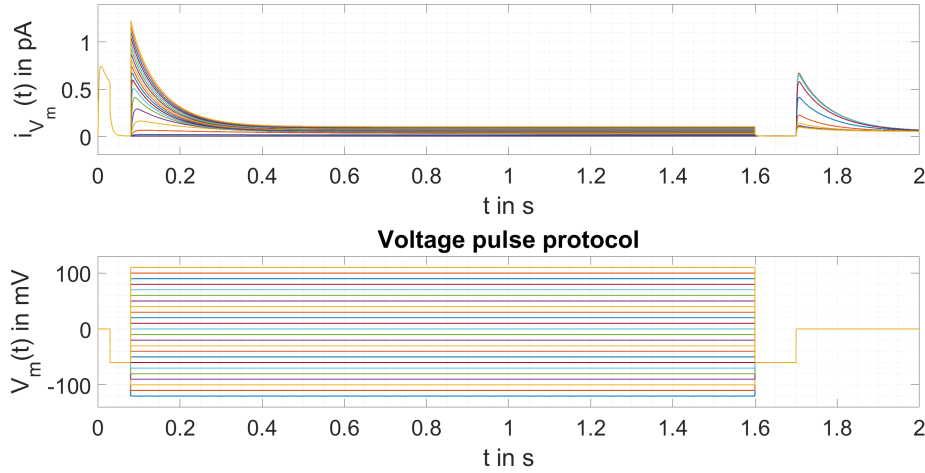


Figure 27: Simulated single channel current response of $K_V1.1$.

4 Results

Single channel current response of ch-K_V1.2-Goodchild2012 ($g = 18$ pS, $E_K = -107.5$ mV)

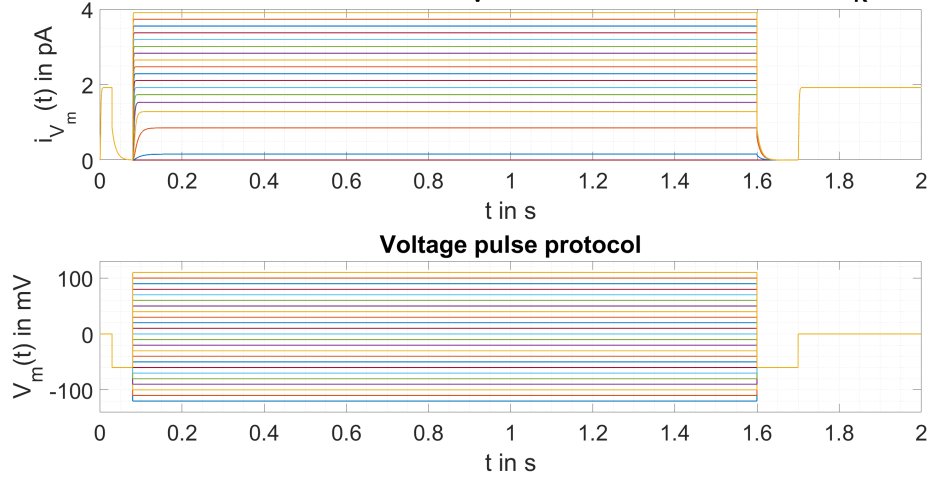


Figure 28: Simulated single channel current response of K_V1.2.

Single channel current response of ch-K_V1.3-Hou2014 ($g = 13$ pS, $E_K = -107.5$ mV)

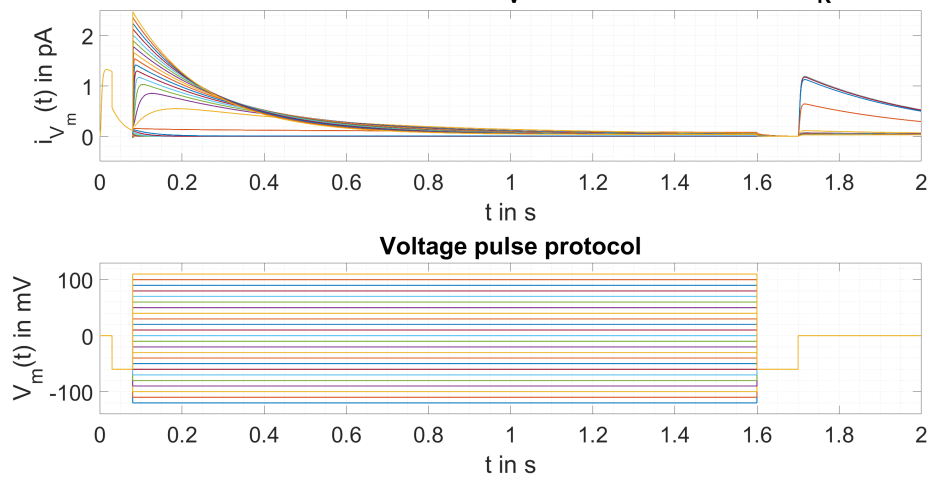


Figure 29: Simulated single channel current response of K_V1.3.

4 Results

Single channel current response of ch-K_V1-5-Ellinwood2017 ($g = 8$ pS, $E_K = -107.5$ mV)

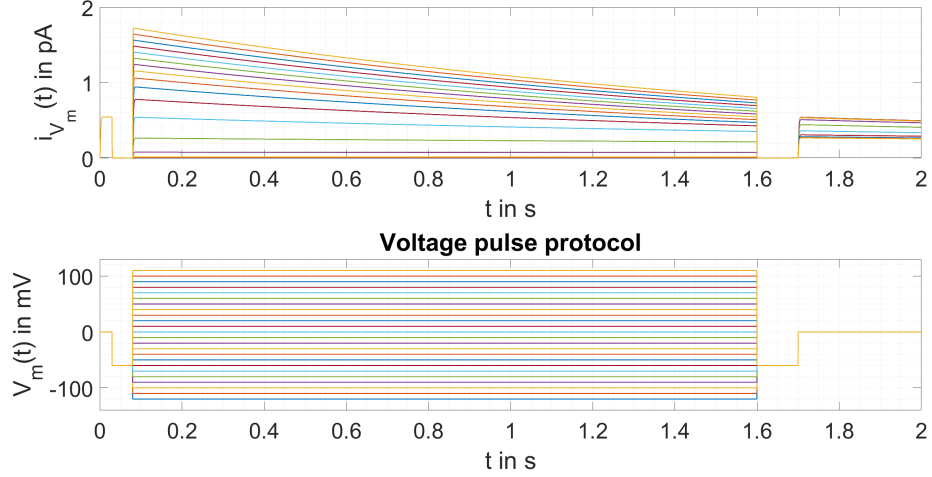


Figure 30: Simulated single channel current response of K_V1.5.

Single channel current response of ch-K_V7-1-Pusch1998 ($g = 1.8$ pS, $E_K = -107.5$ mV)

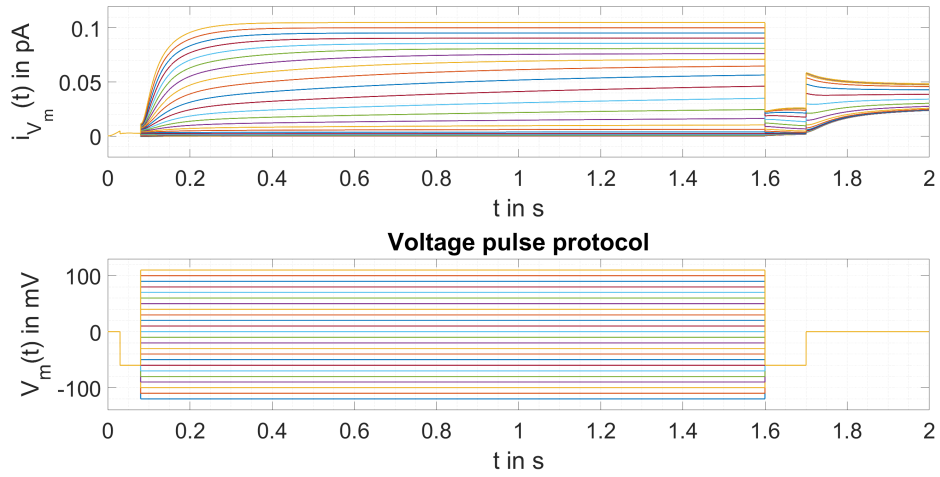


Figure 31: Simulated single channel current response of K_V7.1.

4 Results

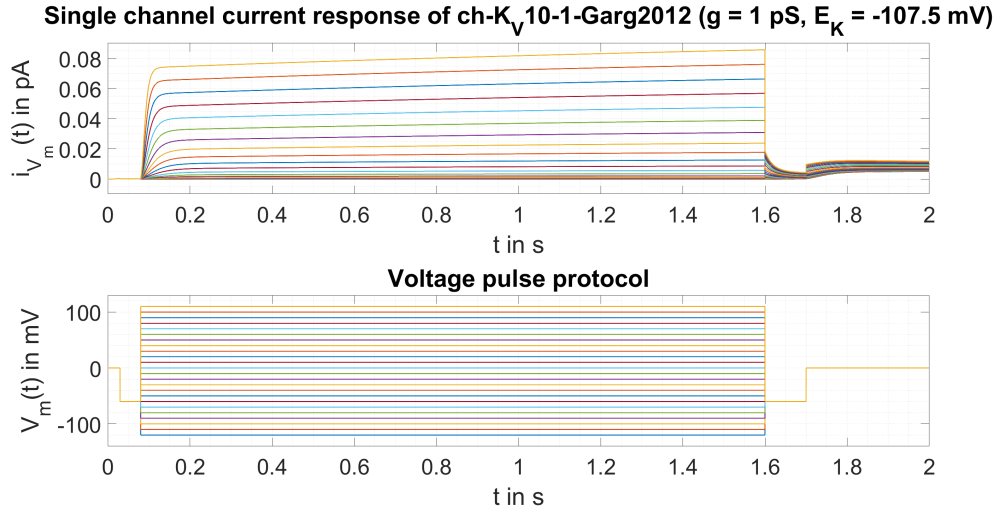


Figure 32: Simulated single channel current response of K_V10.1.

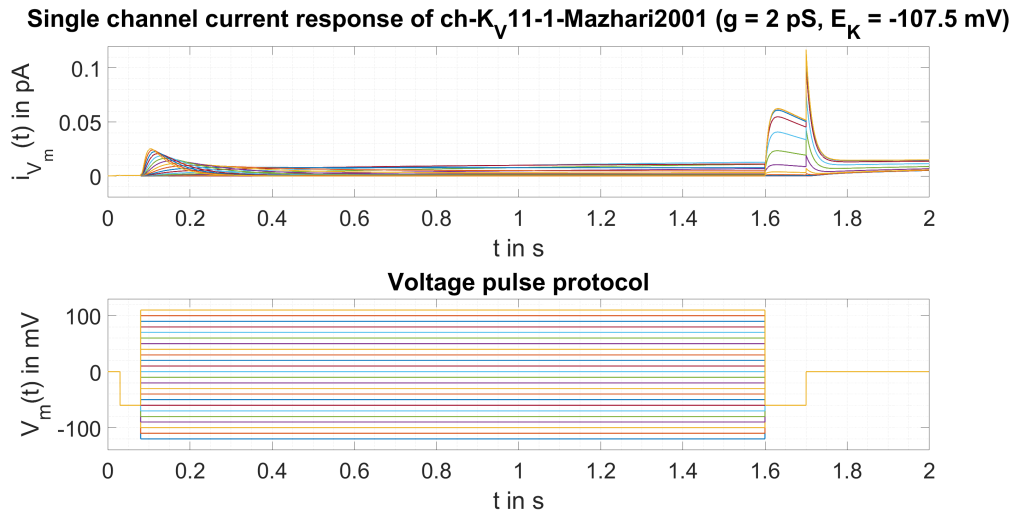


Figure 33: Simulated single channel current response of K_V11.1.

4.3 Comparison of Modelling Approaches

Figure 34 shows the macroscopic current responses $I_{V_m}(t)$ of $K_{V7.1}$ using deterministic and stochastic modelling approaches for a channel expression level of $N_C = 175$.

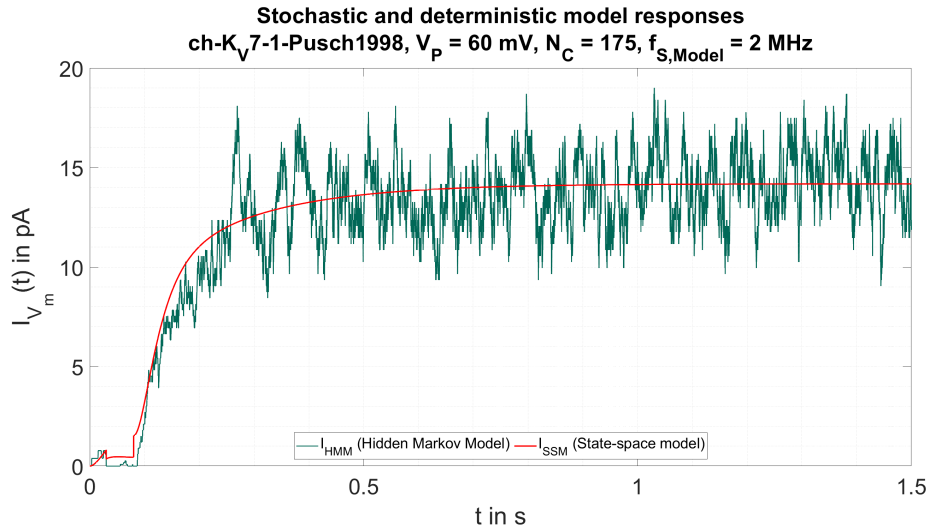


Figure 34: Comparison of macroscopic current responses of $K_{V7.1}$. The current response of the deterministic model is shown in red and the current response of the stochastic one is shown in green. Channel expression level N_C and voltage pulse of VPP were chosen as indicated in the figure.

4.4 Experimental Data

The figures 35 to 38 and 39 to 41 show the measured whole-cell currents $I_{tot}(t)$ of MCF-7 and MCF-10A before and after each step in preprocessing.

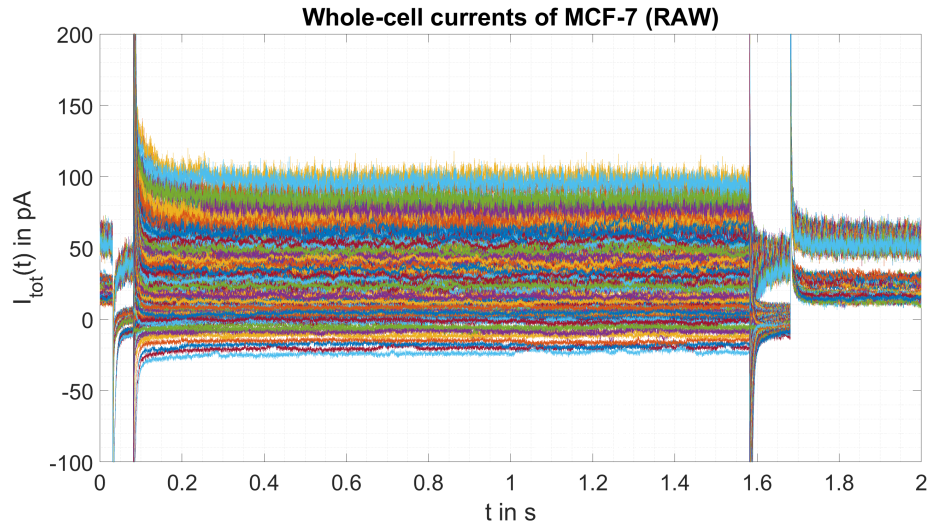


Figure 35: Experimental data of MCF-7 cell (RAW).

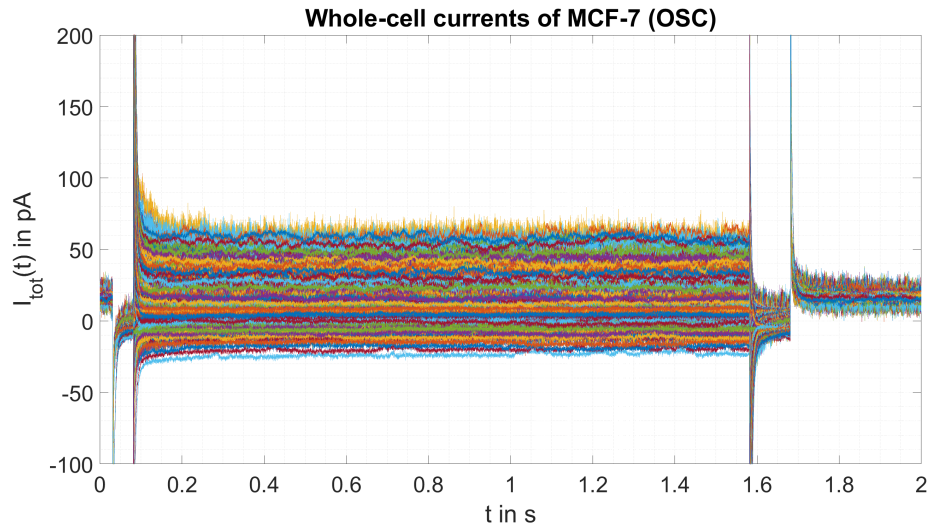


Figure 36: Experimental data of MCF-7 cell after offset correction (OSC).

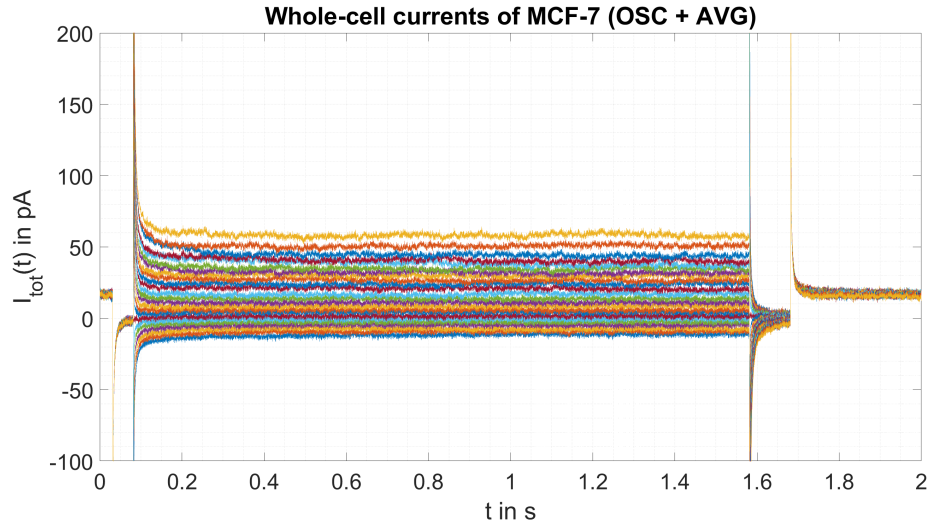


Figure 37: Experimental data of MCF-7 cell after offset correction (OSC) and averaging (AVG).

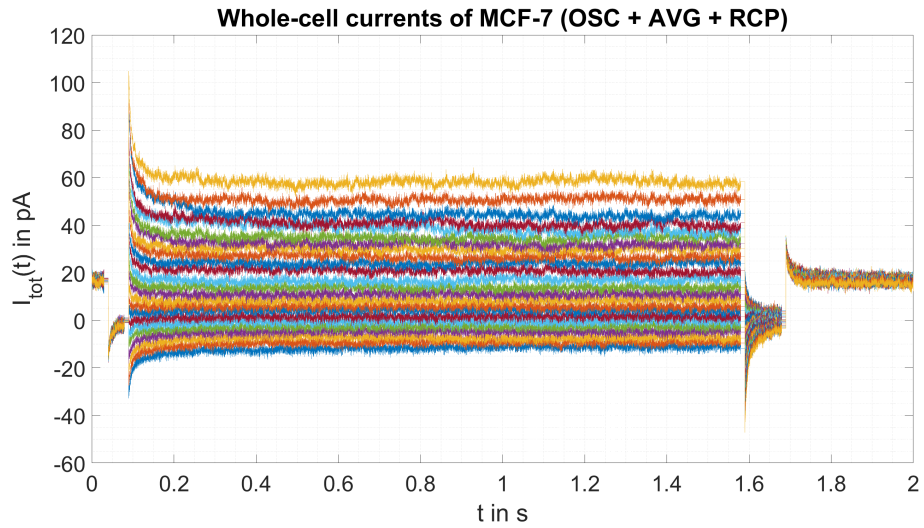


Figure 38: Experimental data of MCF-7 cell after offset correction (OSC), averaging (AVG) and removal of capacitive peaks (RCP).

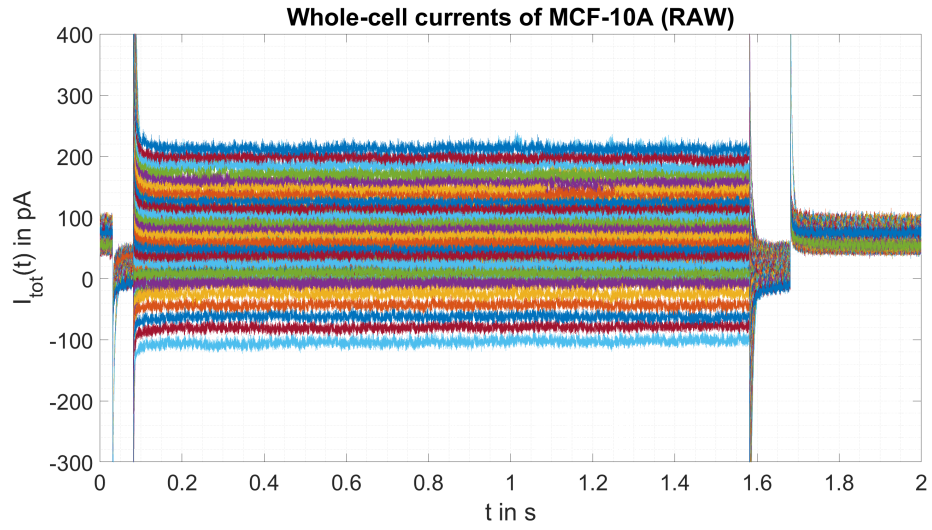


Figure 39: Experimental data of MCF-10A cell (RAW).

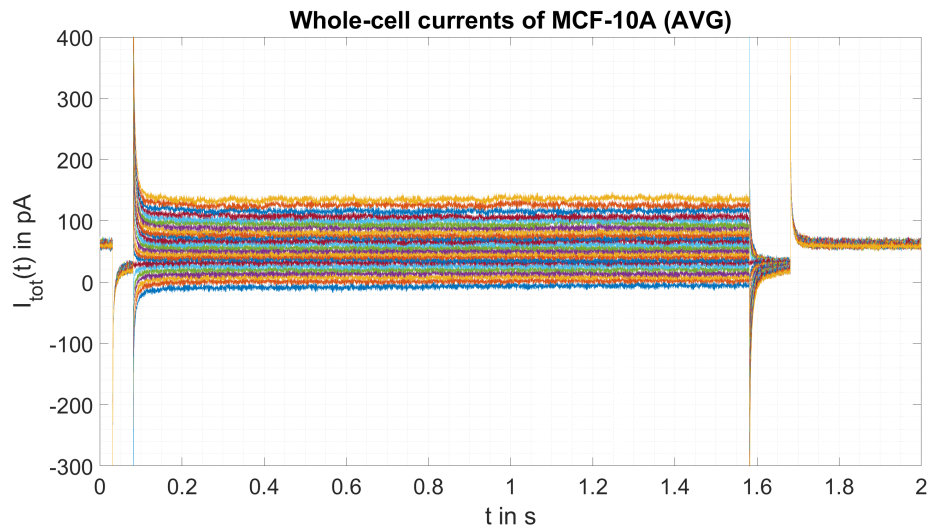


Figure 40: Experimental data of MCF-10A cell after averaging (AVG).

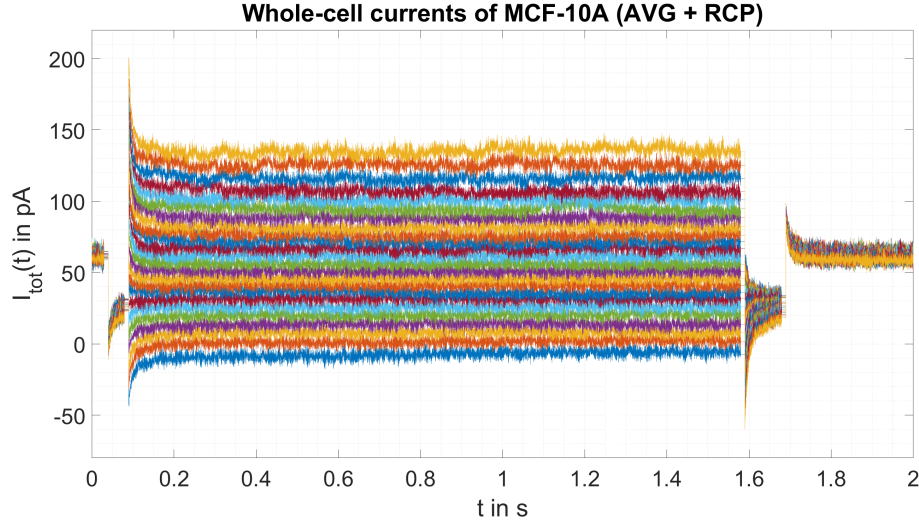


Figure 41: Experimental data of MCF-10A cell after averaging (AVG) and removal of capacitive peaks (RCP).

4.5 Gating Analysis

The figures 42 and 43 show the steady state open probabilities $P_{O,SS}(V_P)$ per channel, the total open probability in steady state $P_{O,tot,SS}(V_P)$ and the averaged measured whole-cell current in steady state $I_{tot,SS}(V_P)$. With respect to the figures 42 and 43, the reversal potential of MCF-7 appeared to be approximately -70 mV and the reversal potential of MCF-10A approximately -110 mV.

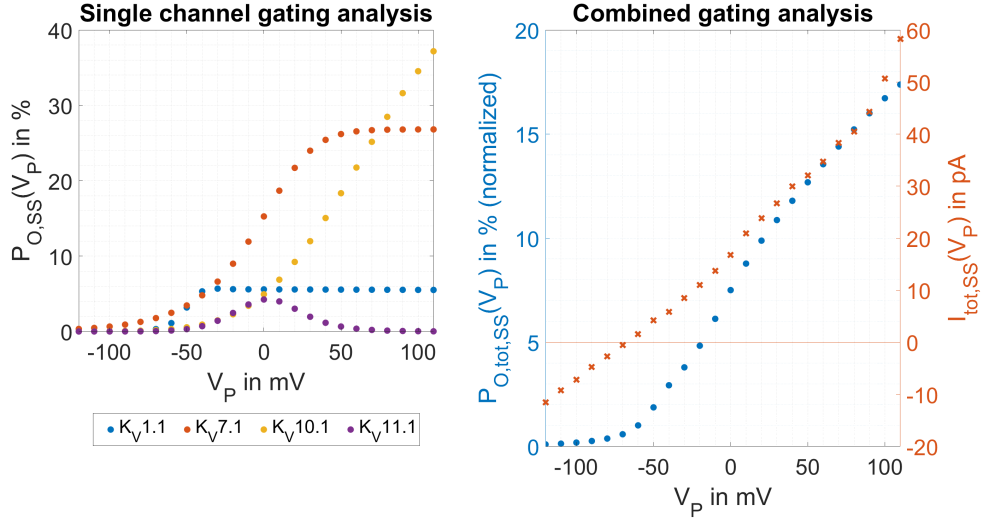


Figure 42: Gating analysis with respect to the MCF-7 model.

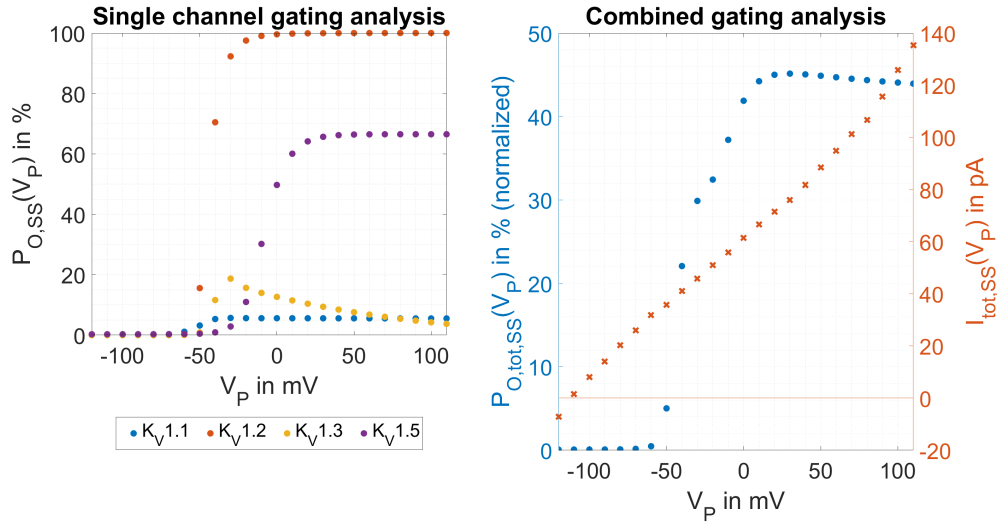


Figure 43: Gating analysis with respect to the MCF-10A model.

4.6 Optimization Results

An overview of the optimization results of both cell models is shown in table 6. Optimization no. 1 and 2 refer to optimizations of four channel expression levels per cell line (default configuration of optimization). No. 3 refers to optimization in case of reduced dataset usage in MCF-10A. Table 7 shows the defined constraints for each optimization. Figure 44 shows the current responses $I_{V_m, tot}(t)$ of the optimized MCF-7 cell model (no. 1) for all 24 pulse potentials V_P of the pulse protocol VPP in comparison to the experimental data. Figure 46 shows the the same for the MCF-10A cell model (no. 2). The simulation results are shown in red (approximation) and the experimental data is shown in green (reference). The figures 45a and 45b as well as the figures 47a and 47b exemplary show the compositions of the optimized currents $I_{V_m, tot}(t)$ in comparison with the whole-cell currents $I_{tot}(t)$ from experimental data for the two pulse potentials $V_P = -60mV$ and $V_P = 60mV$ for each cell model.

The optimization results of the MCF-10A model in case of reduced dataset usage (no. 3) are illustrated analogously to the models optimized in default mode. The current responses of this model can be seen in figure 48. The current compositions are shown in the figures 49a and 49b.

No.	Cell model	$N_{C,1}$	$N_{C,2}$	$N_{C,3}$	$N_{C,4}$
1	MCF-7	60 ($K_{V1.1}$)	222 ($K_{V7.1}$)	307 ($K_{V10.1}$)	5 ($K_{V11.1}$)
2	MCF-10A	1 ($K_{V1.1}$)	32 ($K_{V1.2}$)	2 ($K_{V1.3}$)	1 ($K_{V1.5}$)
3	MCF-10A	11 ($K_{V1.1}$)	0 ($K_{V1.2}$)	1 ($K_{V1.3}$)	100 ($K_{V1.5}$)

Table 6: Optimization results of cell models

No.	$N_{C,1}$		$N_{C,2}$		$N_{C,3}$		$N_{C,4}$	
	min	max	min	max	min	max	min	max
1	60	70	120	222	5	350	5	350
2	1	100	1	100	1	100	1	100
3	1	100	-	-	1	100	1	100

Table 7: Constraints of optimizations

4 Results

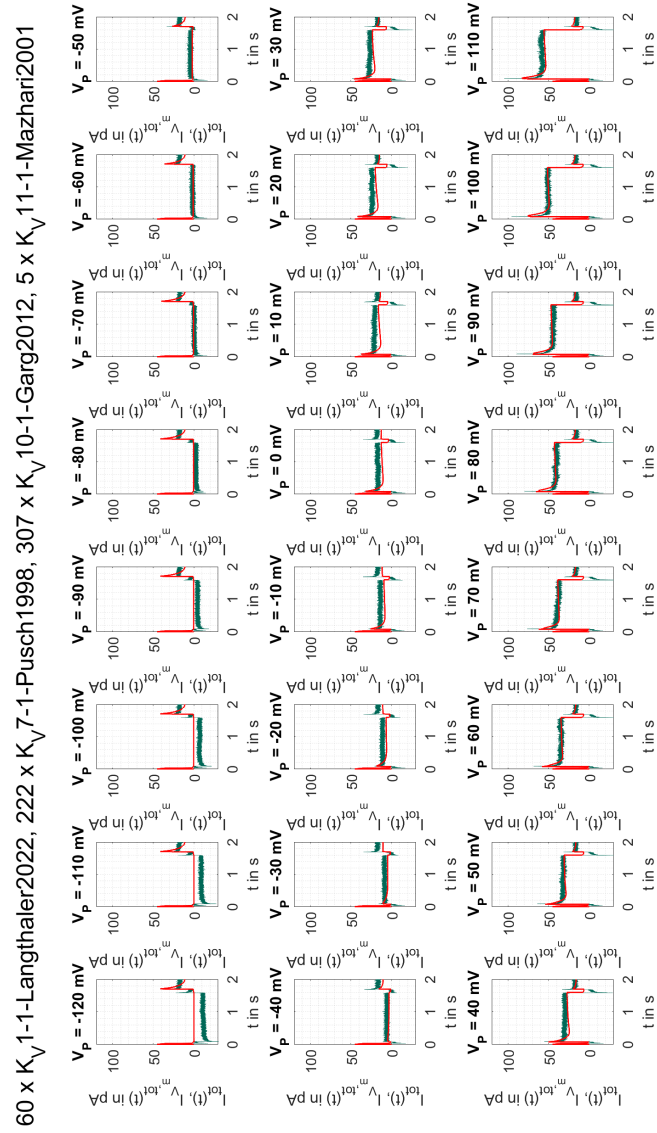
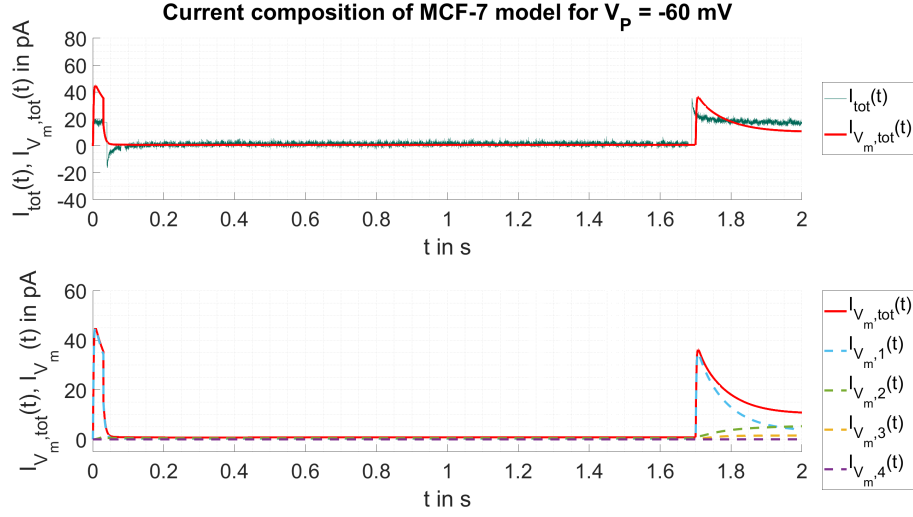
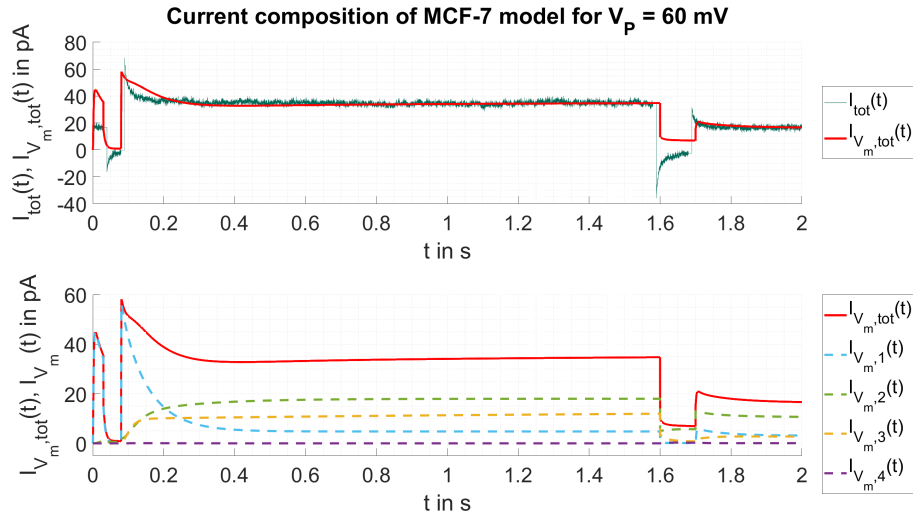


Figure 44: Simulated whole-cell currents of MCF-7 cell model.

4 Results



(a) Composition of $I_{V_m, tot}(t)$ for $V_p = -60$ mV



(b) Composition of $I_{V_m, tot}(t)$ for $V_p = 60$ mV

Figure 45: Current composition of MCF-7 model.

4 Results

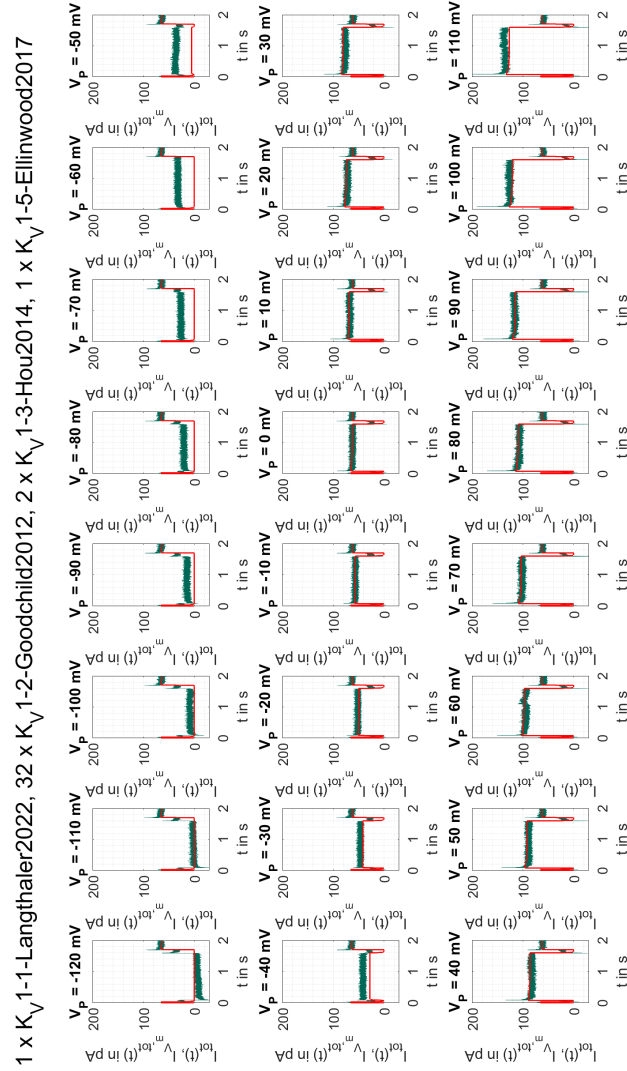
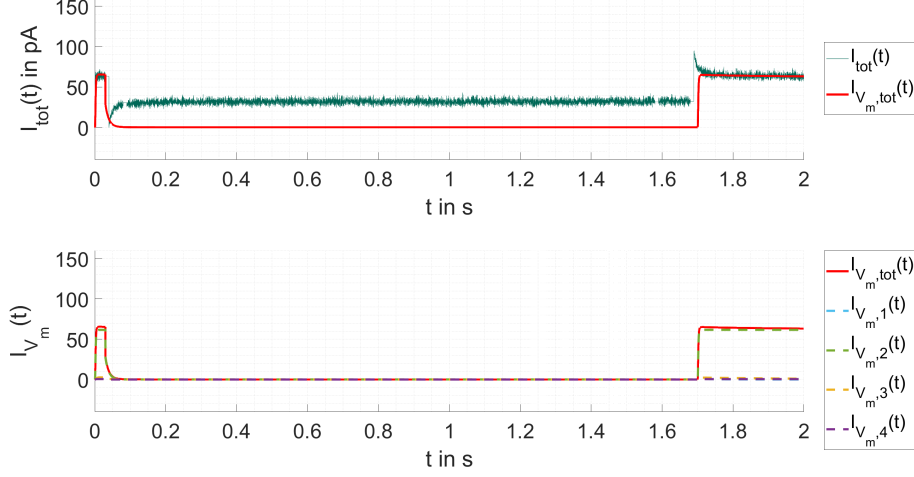


Figure 46: Simulated whole-cell currents of MCF-10A cell model.

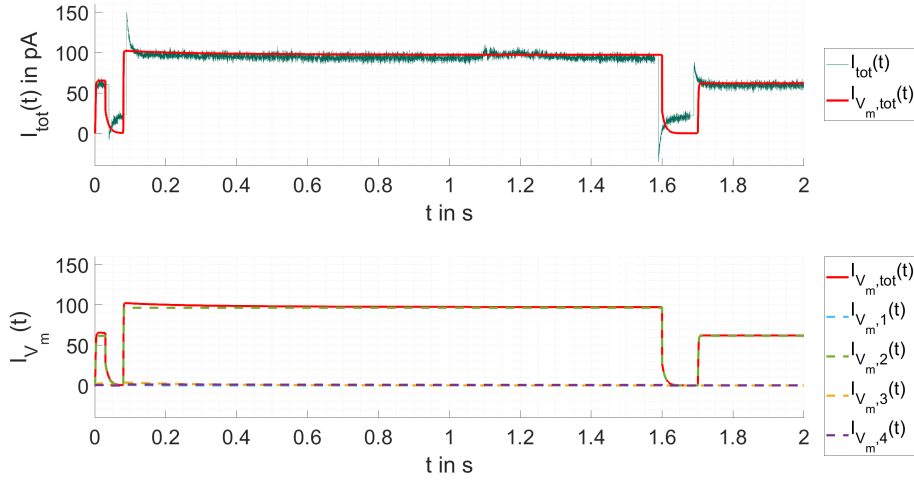
4 Results

Whole-cell current and macroscopic currents of MCF-10A model for $V_p = -60$ mV



(a) Composition of $I_{V_m, tot}(t)$ for $V_p = -60$ mV

Whole-cell current and macroscopic currents of MCF-10A model for $V_p = 60$ mV



(b) Composition of $I_{V_m, tot}(t)$ for $V_p = 60$ mV

Figure 47: Current composition of MCF-10A model.

4 Results

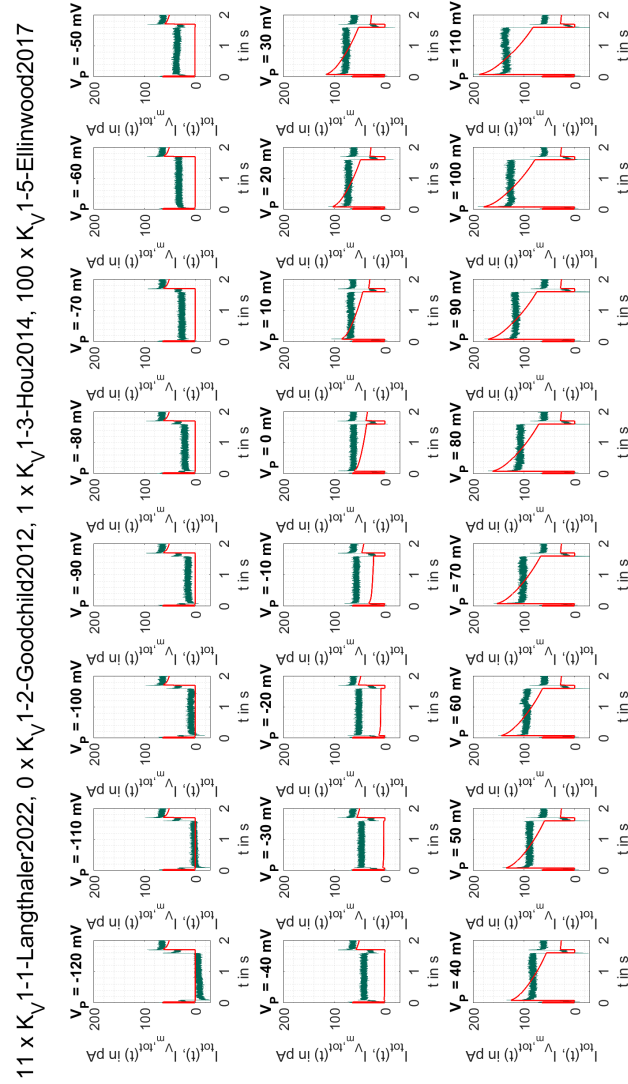
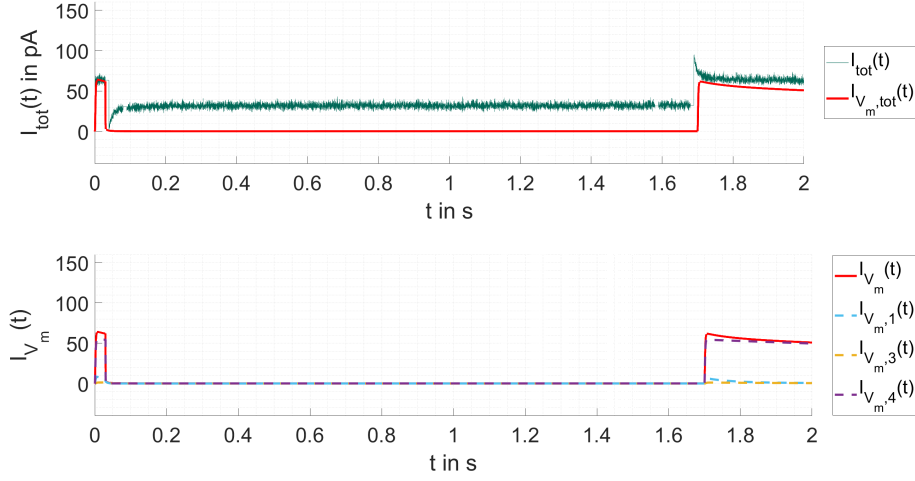


Figure 48: Simulated whole-cell currents of MCF-10A cell model (RDU).

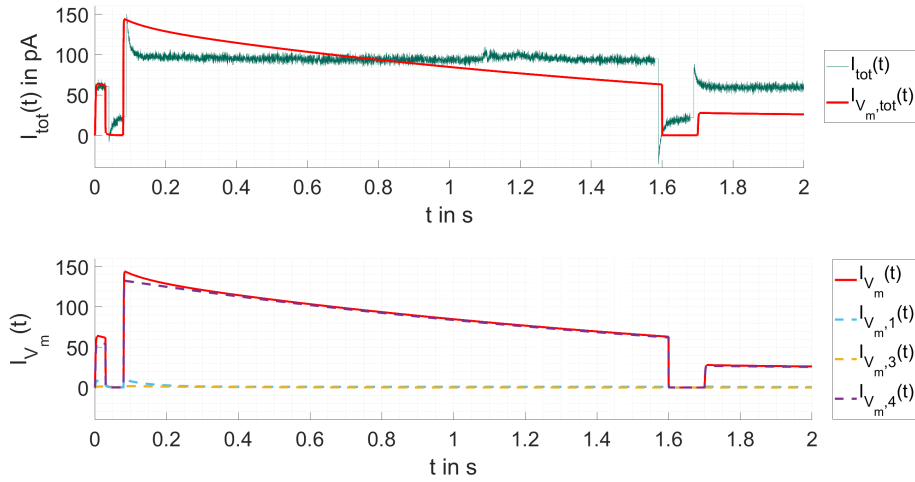
4 Results

Whole-cell current and macroscopic currents of MCF-10A model for $V_p = -60$ mV



(a) Composition of $I_{V_m,tot}(t)$ for $V_p = -60$ mV

Whole-cell current and macroscopic currents of MCF-10A model for $V_p = 60$ mV



(b) Composition of $I_{V_m,tot}(t)$ for $V_p = 60$ mV

Figure 49: Current composition of MCF-10A model (RDU).

5 Discussion

5.1 Channel Expression

Both cell lines were modelled using four voltage-gated potassium channels each. Only $K_{V1.1}$ was found to be expressed in both cell lines. Remaining channel expressions appeared to be divers, which was not surprising. One concluded that this might be linked to the fact that MCF-7 cells are malign and MCF-10A cells are benign breast cells. Therefore, differences in ion channel expressions were expected beforehand. Expressions of $K_{V10.1}$ and $K_{V11.1}$ in the malign cell line were in harmony with literature on ion channel expression in cancer [17]. Regarding the K_V1 family, the presented reports of expressions were principally consistent.

The literature research was limited to voltage-gated potassium channels regarding MCF-10A. It is fair to say that more literature for MCF-7 than for MCF-10A was available. This was specifically the case in context of K_V -channels as well. A possible explanation for this could be the fact that MCF-7 is by far the most popular breast cancer cell line.

A channel was considered to be expressed when the mRNA transcript of the corresponding gene and its corresponding protein were determined in the cell. This was principally the case for all channels in the MCF-7 cell model. In case of $K_{V1.1}$, the functional expression in MCF-7 was confirmed by using the selective blocker α -DTX when measuring the whole-cell current [48]. The functional expression of $K_{V7.1}$ was confirmed using specific blockers and observing the ability of MCF-7 in context of performing RVD [84]. The functional expression of $K_{V11.1}$ was confirmed analogously to this approach [49]. In case of $K_{V10.1}$, the functional expression was considered to be confirmed based on channel blocking experiments in [49].

Although the mRNA and protein expression of $K_{V1.5}$ in MCF-7 was reported in [83], this particular channel was not used in the MCF-7 cell model as the publication was assessed to be not reliable enough in order to confirm the functional expression in this context.

Caused by the insufficient data situation, the reported mRNA transcript expression was defined as the only requirement for integrating single channel models into the MCF-10A cell model. This proved to be an appropriate approach as only the presence of $K_{V1.5}$ was confirmed in this cell line in context of protein expression.

It was noticeable that publications on ion channel expressions in the MCF-7 cell line were partially clustered by research groups. It should be noted as well that the literature research beyond K_V -channels was performed for MCF-7 only. Furthermore, the expressions of $K_{V7.1}$, $K_{V10.1}$ and $K_{V11.1}$ in MCF-10A could not be excluded as no data on this could be found.

5.2 Modelling Approach

In this thesis, the principally stochastic single channel currents were approximated using a deterministic modelling approach. This was done under the assumption that a sufficiently high number of channels is expressed in the subjected cell lines. An exemplary comparison of these two modelling approaches is presented in chapter 4.3 for illustration purposes only, using the chosen model for $K_{V7.1}$ and its optimized expression level in the MCF-7 cell model.

As described, Markov Models provide a very sufficient and flexible modelling framework for ion channels [53]. In the end, they are still approximations, since they are naturally incapable of completely mapping the conformational changes on a molecular level with a 100 % accuracy. Usually, these models comprise several states that correlate with the same physical observations (emissions). In context of voltage-gated ion channels, these emission are either a single channel current represented by $i_{V_m}(t) \neq 0$ or no current, i.e $i_{V_m}(t) = 0$.

Therefore, considering these models to be Hidden Markov Models is principally correct as the emissions alone do not allow determining the exact state the channel occupies at a particular time.

Modelling the whole-cell current using the deterministic approach could be considered as fairly accurate as the conditions $N_{C,i} \geq 1$ and $\sum_i N_{C,i} \gg 1$ held in any case. The smooth current curves in this case allowed assessing model behaviour more easily. The random fluctuations were assumed to vanish as the total amounts of channels in the cell models were relatively high.

Modelling the single channel currents deterministically had striking advantages. Firstly, it made simulations reproducible and therefore comparable. The effects of changes in the model could be observed directly in the resulting alterations in current responses. Secondly, the deterministic approach reduced computational effort as the channel responses on a given pulse protocol could be calculated, stored and loaded again. On the other hand, it must be noticed that the deterministic approach is basically an approximation and does not fully replicate the gating kinetics as it completely neglects the stochastic characteristics of ion channels in principal. However, it was shown that various publications proposed Markov Models to be well suited for this kind of application and that they allow a flexible fitting of experimental data as well.

The modelling approach presumes a sufficiently high expression level of channels in order to compensate random fluctuations of currents. However, the minimum expression level in this context is not generally quantifiable as it depends. Choosing the appropriate approach primarily depends on how big the current fluctuations are, in relation to the expected macroscopic current of the observed channel population in a patch [52]. Discussed observations in this context are principally in harmony with previous considerations and reports from literature.

5.3 Single Channel Models

The figures 27 to 33 in chapter 4.2 show the single channel current responses $i_{V_m}(t)$ on varying membrane potentials $V_m(t)$. Some kinetic models performed well immediately after implementation. For most channels however, several cycles of model implementation and assessment were necessary, especially when several kinetic models were available. Implementation, testing and assessment of several kinetic models assigned to one channel increased the chance of using an appropriate single channel model and enhanced cell model performance in context of replicating current responses more realistically. Working through several publications for single channel implementation was time-consuming but reasonable in any case.

The used models were most probably afflicted with inaccuracies as their topologies were based on observed channel characteristics and their transition rates were based on experimental data in most cases. Evaluation of channel responses in this thesis mainly referred to qualitatively assessing gating properties. This was carried out by comparing simulated single channel current responses $i_{V_m}(t)$ with provided experimental data from literature (e.g. [67]). This approach turned out to be appropriate and expedient.

Several assumptions were made during the modelling process. One of these assumptions was the partial neglect of temperature influences on gating kinetics. Gating kinetics were shown to be strongly dependent on temperature [67]. With exception of the kinetic models introduced by [65] and [53], no model could be found for replicating $K_V1.1$ inactivation. The models by [65] and [53] were parametrized for 35 °C. $K_V1.1$ channels generally inactivate faster at higher temperatures and this difference appeared to be very significant compared to room temperature [67]. The simplification of neglecting temperature dependencies can be considered as a major limitation of the developed models.

Finding an appropriate kinetic model for modelling single channel responses of voltage-gated potassium channels was not a straight-forward process. The number of available models directly correlated with the popularity of each channel. In most cases, the number of available models was low. Although modelling channel kinetics using Markov Models was said to be a common approach in modern days, it was unexpectedly hard to find

kinetic models with comprehensive documentation for the general use. For example, several kinetic models introduced in this thesis were originally developed for investigating drug impacts on ion channel gating.

In this thesis it was assumed that functionally expressed ion channels exhibit the same gating kinetics across different cell types. This assumption was mandatory as no kinetic models could be found that were specifically developed and parametrized for MCF-7 or MCF-10A cells. As highlighted in a previous study, kinetics of K_V -channels are basically consistent across different cell lines [67].

Regarding scheme topology and parametrization, kinetic models of channels were fully adopted from literature. Therefore, models and corresponding responses were principally considered to be correct after implementation and review. Some channels indeed produced unexpected responses at certain clamping potentials. For example, a discarded $K_V1.2$ implementation variant showed a very excessive inactivation in higher voltage ranges.

It is fair to say that the implemented single channel models in this thesis were afflicted with inaccuracies due to simplifications and assumptions. This was expected beforehand. The presented selection of kinetic models in this thesis can be used as a solid starting point both for integration in cell models and further developments as the concerning literature research was carefully and comprehensively carried out.

5.4 Experimental Data

The experimental data used for optimizing the macroscopic currents in the cell models was provided without documentation. As described in chapter 3, measurements concerning the MCF-10A cell line were carried out in a single measurement system. Therefore, all results were afflicted by the same absolute offset. Considering the offset correction being obsolete in this case was appropriate. Generally, the measurement data of MCF-10A cells appeared to be afflicted with more noise than current curves of the other measurement system.

The offset correction of MCF-7 measurement results was mandatory as it could be seen with the bare eye that relative offsets differed significantly. The compensation was carried out with respect to a chosen reference measurement. Offset correction provided a better signal quality as the noise could be reduced more efficiently by the subsequent averaging. Importantly, it must be noted that offset correction of MCF-7 whole-cell currents affected the results tremendously. By adjusting the offsets with reference to measurement one, the MCF-7 data showed no inward current for all voltages in VPP. Using the other measurement system resulted in inward currents for lower clamping potentials.

In this thesis the same measurement system (three of five measurements in MCF-7 and five of five measurements in MCF-10A) was used as reference for offset correction. This was done in order to make the measurements of the two cell lines comparable but consequently resulted in moving the MCF-7 whole-cell currents towards more negative values. Concretely, this resulted in negative/inward currents for the MCF-7 cell line in the voltage range $-120mV < V_m < -80mV$. The correctness of the offset corrected currents however could not be confirmed as only the relative offsets between the measurement systems could be compensated but the absolute offsets of the measurements were unknown.

The question may arise, if there would have been a significant difference when the other measurement system was used as reference in offset correction. Most probably not, because of the following reasons. The reversal potential of potassium in both measurement arrangements was calculated with $E_K = -107.5mV$. This means that only voltage pulses below this threshold would have been able of driving a negative potassium current, i.e. a potassium current in inward direction. This would have been possible for two voltage levels only: $V_p = -120mV$ and $V_p = -110mV$. Additionally, the steady state open probabilities of the integrated channel models were shown to be close to zero in almost all cases for these low clamping potentials. In the end, it would have been impossible anyway to accurately model the negative currents for lower clamping potentials by considering the integrated K_V -channels only. A possible consideration in this case would have been a leakage current in inward direction to enhance the whole-cell current fits of the cell models. The introduction of leakage currents in the cell models was considered to be principally questionable as no documen-

tation was provided for the experimental data at all. One decided against this approach as a leakage current would have only enhanced optimization results without having an additional benefit in quality of replicating the voltage-gated potassium current.

By comparing the whole-cell currents in the figures 13 and 35, it is fair to say that a lot of information in MCF-7 whole-cell currents was lost due to uncompensated capacitances, especially in terms of current onset when switching the clamping potential. The whole-cell currents markedly differed in size as well. A quantitative comparison of these two measurements was not made. Principally, the same observations were made with respect to the MCF-10A whole-cell currents.

5.5 Gating Analysis

As it can be seen in figure 42, integrated single channel models in the MCF-7 model drastically differed in their steady state open probabilities $P_{O,SS}(V_P)$. The implemented $K_{V1.1}$ model responded with a current spike for each activation but opened only for voltages higher than $V_P = -60mV$ in a long term. At $V_P = -30mV$, the steady open probability reached a fixed value of approximately 5.5 %. $K_{V7.1}$ showed activation before reaching a plateau throughout the whole voltage range in VPP. The channel slowly started opening from $V_P = -120mV$ on and the steady state open probability asymptotically reached a fixed value of approximately 27 %. The corresponding $P_{O,SS}-V_P$ -curve of this channel had the shape of a sigmoid function. $K_{V10.1}$ started opening at $V_P = -30mV$. The steady state open probability of $K_{V10.1}$ was shown to be directly linked to the membrane potential and exhibited a quasi-linear dependency on voltage for $V_P > 0V$. In contrast, the steady state open probability of $K_{V11.1}$ was low for all values of V_P compared to the other channels. The open probability started increasing at $V_P = -60mV$, peaked at $V_P = 0V$ and decreased again in the same manner, resulting in a steady state open probability of approximately zero for voltages in the ranges of $V_P < -60mV$ and $V_P > 60mV$.

In figure 42 it can be seen, that the MCF-7 cell exhibited a steady state inward current for voltage pulses in a range of $-120mV \leq V_P \leq -70mV$. The total

steady state open probability $P_{O,tot,SS}(V_p)$ was rather low in this voltage range because channels started opening from $V_p = -60mV$ on. Based on the modelled gating behaviours, the whole-cell current was expected to be more accurately modelled for the voltage range $-60mV \leq V_p \leq 120mV$. Significant deviations were expected for the voltage range of $-120mV \leq V_p \leq -70mV$.

The same gating analysis was carried out with respect to the MCF-10A model. The results are shown in figure 43. As the $K_{V1.1}$ model was adopted from the other cell model, it logically showed the same gating behaviour in steady state. The $K_{V1.2}$ model showed an abrupt increase in steady state open probability, starting at $V_p = -50mV$. At $V_p = 0V$, the open probability of the channel reached approximately 100 %, resulting in relatively high macroscopic currents. Due to its gating behaviour and high conductance, this channel was expected to be significantly up-regulated in the MCF-10A model. $K_{V1.3}$ was shown to produce spikes when activated and showed a strong inactivation. The steady state open probability started rising from $V_p = -50mV$, reached a maximum at $V_p = -30mV$ and decreased again for higher voltages. The higher the voltage, the lower was the open probability. At $V_p = 80mV$, the steady state open probability of $K_{V1.3}$ fell below the plateau value of $K_{V1.1}$. The steady state open probability of $K_{V1.5}$ was shown to slowly increase from $V_p = -50mV$ on and reached a fixed value at $V_p = 40mV$. The curve was similar to steady state open probability of $K_{V7.1}$, although this channel shows a slow inactivation.

In contrast to the MCF-7 cell, the experimental data of the MCF-10A cell showed no inward currents, with exception of the whole-cell current at $V_p = -120mV$. The total open probability in steady state was approximately zero for voltages in a range of $-120mV \leq V_p \leq -60mV$. Above this range, the total steady state open probability started to increase abruptly, peaking at $V_p = 30mV$. The slow decrease after peaking was obviously caused by the decreasing open probability of $K_{V1.3}$. Based on the gating analysis of integrated single channel models, the cell model was expected to show high deviations for lower voltage ranges as the open probability was very low for $V_p \leq -40mV$. As $K_{V1.2}$ showed almost 100 % steady state open probability for higher voltages, the optimization result of this particular channel was expected to be relatively high.

5.6 Cell Models

By using the optimized channel expression levels it could be shown that the modelling approach was principally able to replicate the whole-cell currents in both cell lines. As it can be seen in the figures 44 and 46, the modelled whole-cell currents (red) fitted the currents from experimental data (green) well for most clamping potentials. Not only the steady state currents could be modelled fairly accurate but also dynamic changes and stabilizations on steady state values were surprisingly well replicated in the MCF-7 model. Generally, it could be clearly seen that the MCF-7 model resulted in better outcomes than the MCF-10A model due to the following reasons.

The lacking inactivation of the integrated $K_{V1.2}$ model resulted in a significant up-regulation of the $K_{V1.2}$ expression level in the optimized MCF-10A model. The optimization provided a good fit to the MCF-10A whole-cell current on the one hand but resulted in low optimized channel expression levels of $K_{V1.1}$, $K_{V1.3}$ and $K_{V1.5}$ on the other. For comparison, the MCF-10A model was also optimized using a reduced dataset, bypassing the $K_{V1.2}$ expression level. The corresponding results are shown in figure 48. Bypassing $K_{V1.2}$ resulted in a strong up-regulation of $K_{V1.5}$ expression levels, going hand in hand with a worse fitting in the cell model as the integrated $K_{V1.5}$ model replicated a slow inactivation. The suspicion in this context was, that the optimized MCF-10A model was not replicating the whole-cell current very realistically. This might also be partially caused by the fact that optimization constraints in the MCF-10A model were chosen without prior knowledge.

In general, it was obvious and could be clearly noticed that the relative errors were significantly higher for lower voltages in the pulse protocol. The fit error decreased as the pulse potentials increased because of the opening of large amounts of channels simultaneously. These observations were in harmony with the previously described gating behaviour of integrated single channel models in both cell models and are reflected by the comparisons of current compositions, shown in the figures 45, 47 and 49. The fit error for lower voltages was indisputably caused by the fact that the integrated potassium channel models slowly started opening at $V_P = -60mV$ in MCF-7 and MCF-10A models.

The only exception was the $K_{V7.1}$ model in MCF-7 that slightly opened at $V_p = -120mV$ already. The change in conductivity over V_p was slow in the MCF-7 model and abrupt in the MCF-10A model.

Based on the the provided and preprocessed experimental data, it could be seen that whole-cell currents of MCF-7 and MCF-10A cells appeared to be outward currents for most clamping potentials. This was in harmony with published results of whole-cell patch-clamp measurements by [48] (MCF-7) and [50] (MCF-10A). Cells typically maintain a higher potassium concentration in the intracellular region [8]. When exclusively considering potassium, this naturally results in an outward current of potassium for the case $V_m > E_K$, provided that the corresponding channels are open. Furthermore, it was reported that the MCF-7 whole-cell current is largely maintained by potassium [48]. The approach of modelling the whole-cell current in MCF-7 by focussing on voltage-gated potassium channels in the first place was surely an appropriate approach in this context as it was possible to model a large part of the whole-cell current with a fair amount of integrated single channel models. It must be noted that the cell models are surely incomplete. A possible way for modelling the inward currents at lower voltages would have been the implementation of a leakage channel for maintaining a voltage-dependent current in inward direction. Alternatively, also the introduction of sodium currents would have been an appropriate approach for modelling inward currents in this context. It should be mentioned at this point that MCF-7 cells were also reported to express BK and SK4 channels [87], [88]. A presentation of corresponding findings from literature is included in the appendix. These two channels were also used in context of A-549 cell modelling [54]. As this thesis focusses K_V -channels in the first place, they were not integrated into the MCF-7 model but doing so can be considered as an appropriate way of extending the current model.

6 Conclusion

The literature research on K_V -channel expressions in MCF-7 and MCF-10A cells resulted in four channels for each cell line. It was shown for the MCF-7 cell line specifically that the whole-cell current could be replicated nicely using only four kinetic models of voltage-gated potassium channels. Results of the MCF-10A modelling were also shown to fit the experimental data surprisingly well, although rougher assumptions were made for this cell model. Removing a single channel expression was shown to result in a significantly worse fitting of the MCF-10A model (RDU). Nevertheless, results of MCF-10A modelling are principally questionable due to specified reasons.

Compared to the MCF-7 cell line, data on ion channel expression in MCF-10A was hardly accessible. This was considered to be linked to the enormous popularity of MCF-7 and to the fact that MCF-10A is actually not a cancer cell line. It was generally hard to compare these two cell lines as they differed both in malignancy and molecular identity. It could be found that $K_{V1.1}$ was reported to be expressed in both. While MCF-7 was shown to express a diverse variety of voltage-gated potassium channels, MCF-10A was reported to express a large part of the K_{V1} family.

Using the deterministic approach made it possible to principally replicate macroscopic and whole-cell currents in cell models. The correlation between fit error and channel expression level could be illustrated vividly by comparing deterministic and stochastic approach, using an appropriate example. During the modelling process, several assumptions were made. Importantly, it must be pointed out that many of these assumptions limited both complexity and modelling accuracy at the same time.

Based on the simulated single channel current responses and simulated steady state gating characteristics, optimization of the cell models showed expected results. A task for further investigations in this context would be the determination of the actual expression levels of considered K_V -channels in both cell lines for defining the constraints in optimization more accurately. Furthermore, it would be interesting to determine channel expression levels in correlation with MCF-7 and MCF-10A cell cycles. This would add another degree of freedom to the system. Strongly suggested in context of cell modelling is the implementation of an alternative $K_{V1.2}$ model in MCF-10A.

By integrating more channels, it should be possible to further enhance fitting of the simulated whole-cell currents and to replicate them more realistically. Knowledge on channel expressions during the cell cycle would it make possible to model the whole-cell currents dependent on cell proliferation. This could be used for finally modelling V_{rm} and its dependence on the cell cycle in-silico.

Bibliography

- [1] J. Buttlar *et al.*, *Tutorium Genetik*. Springer, Berlin, Heidelberg, 2020 (cit. on pp. 1, 4).
- [2] R. F. Schmidt *et al.*, *Physiologie des Menschen*. Springer, Berlin, Heidelberg, 2007, vol. 30 (cit. on pp. 1–5, 10–12, 15, 16, 21, 23).
- [3] J. Rettinger *et al.*, *Elektrophysiologie*. Springer, Berlin, Heidelberg, 2018 (cit. on pp. 2, 3, 5, 6, 8–10, 12, 18, 19, 21, 22).
- [4] G. P. Rédei, *Encyclopedia of Genetics, Genomics, Proteomics and Informatics*. Springer, Netherlands, 2008 (cit. on pp. 2, 4, 5).
- [5] C. L. Hill and G. J. Stephens, An Introduction to Patch Clamp Recording, M. Dallas and D. Bell, *Patch Clamp Electrophysiology*, Springer Nature, New York, pp. 1–20, 2021 (cit. on pp. 5, 18–22).
- [6] H. Pfützner, *Angewandte Biophysik*. Springer-Verlag, Wien, 2012, vol. 2 (cit. on pp. 6, 8–10).
- [7] G. Adam *et al.*, *Physikalische Chemie und Biophysik*. Springer, Berlin, Heidelberg, 2009, vol. 5 (cit. on pp. 6–11).
- [8] C. Miller, An overview of the potassium channel family, *Genome Biology*, vol. 1, 2000 (cit. on pp. 7, 14, 94).
- [9] V. Schünemann, *Biophysik*. Springer, Berlin, Heidelberg, 2005 (cit. on p. 10).
- [10] S. P. H. Alexander *et al.*, THE CONCISE GUIDE TO PHARMACOLOGY 2021/22: Ion channels, *British Journal of Pharmacology*, vol. 178, pp. 157–245, 2021 (cit. on pp. 12, 13, 35, 52, 53, 64–66, 109, 110).
- [11] F. H. Yu *et al.*, Overview of Molecular Relationships in the Voltage-Gated Ion Channel Superfamily, *Pharmacological Reviews*, vol. 57, pp. 387–395, 2005 (cit. on p. 13).

- [12] Q. Kuang *et al.*, Structure of potassium channels, *Cellular and Molecular Life Sciences*, vol. 72, pp. 3677–3693, 2015 (cit. on p. 14).
- [13] M. S. Sansom *et al.*, Potassium channels: structures, models, simulations, *Biochimica et Biophysica Acta (BBA)*, vol. 1565, pp. 294–307, 2002 (cit. on p. 14).
- [14] S. D. Buckingham *et al.*, Structure and function of two-pore-domain K⁺ channels: contributions from genetic model organisms, *Trends in Pharmacological Sciences*, vol. 26, pp. 361–367, 2005 (cit. on p. 14).
- [15] R. MacKinnon, Determination of the subunit stoichiometry of a voltage-activated potassium channel, *Nature*, vol. 350, 1991 (cit. on p. 14).
- [16] D. A. Doyle *et al.*, The Structure of the Potassium Channel: Molecular Basis of K⁺ Conduction and Selectivity, *Science*, vol. 280, 1998 (cit. on p. 14).
- [17] W. J. Brackenbury, Ion Channels in Cancer, *Ion Channels in Health and Disease*, pp. 131–163, 2016 (cit. on pp. 16, 30–32, 85).
- [18] T. E. DeCoursey *et al.*, Voltage-gated K⁺ channels in human T lymphocytes: a role in mitogenesis? *Nature*, vol. 307, pp. 465–468, 1984 (cit. on p. 16).
- [19] S. C. Lee *et al.*, Increased Voltage-Gated Potassium Conductance during Interleukin 2-stimulated Proliferation of a Mouse Helper T Lymphocyte Clone, *Journal of Cell Biology*, vol. 102, pp. 1200–1208, 1986 (cit. on p. 16).
- [20] D. J. Blackiston *et al.*, Bioelectric controls of cell proliferation: Ion channels, membrane voltage and the cell cycle, *Cell Cycle*, vol. 8, pp. 3527–3536, 2009 (cit. on pp. 16, 17, 30, 31).
- [21] D. Urrego *et al.*, Potassium channels in cell cycle and cell proliferation, *Philosophical Transactions of the Royal Society B: Biological Sciences*, vol. 369, 2014 (cit. on pp. 16, 17, 30).
- [22] H. G. Sachs *et al.*, Changes in membrane potential during the cell cycle, *Experimental Cell Research*, vol. 83, pp. 362–366, 1974 (cit. on p. 17).

- [23] M. Bachmann *et al.*, Voltage-Gated Potassium Channels as Regulators of Cell Death, *Frontiers in Cell and Developmental Biology*, vol. 8, 2020 (cit. on pp. 17, 30, 32).
- [24] M. J. Rosendo-Pineda *et al.*, Role of ion channels during cell division, *Cell Calcium*, vol. 91, 2020 (cit. on p. 17).
- [25] T. Akita *et al.*, Patch-Clamp Techniques: General Remarks, Y. Okada, *Patch Clamp Techniques*, Springer, Tokyo, pp. 21–42, 2012 (cit. on pp. 18–20).
- [26] H. Yawo, Whole-Cell Patch Method, Y. Okada, *Patch Clamp Techniques*, Springer, Tokyo, pp. 43–69, 2012 (cit. on p. 20).
- [27] C. Compton, *Cancer: The Enemy from Within*. Springer, Scottsdale, 2021 (cit. on pp. 22–26, 28).
- [28] D. Hanahan and R. A. Weinberg, The Hallmarks of Cancer, *Cell*, vol. 100, pp. 57–70, 2000 (cit. on pp. 23, 25–27).
- [29] D. Hanahan and R. A. Weinberg, Hallmarks of Cancer: The Next Generation, *Cell*, vol. 144, pp. 646–674, 2011 (cit. on p. 26).
- [30] E. J. Watkins, Overview of breast cancer, *Journal of the American Academy of PAs*, vol. 32, pp. 13–17, 2019 (cit. on p. 28).
- [31] S. E. Burdall *et al.*, Breast cancer cell lines: friend or foe? *Breast Cancer Research*, vol. 5, pp. 89–95, 2003 (cit. on pp. 28, 29).
- [32] G. Kaur and J. M. Dufour, Cell lines, *Spermatogenesis*, vol. 2, pp. 1–5, 2012 (cit. on p. 28).
- [33] X. Dai *et al.*, Breast Cancer Cell Line Classification and Its Relevance with Breast Tumor Subtyping, *Journal of Cancer*, vol. 8, pp. 3131–3141, 2017 (cit. on pp. 28, 29).
- [34] S. Comsa *et al.*, The Story of MCF-7 Breast Cancer Cell Line: 40 years of Experience in Research, *Anticancer Research*, vol. 35, pp. 3147–3154, 2015 (cit. on p. 29).
- [35] Y. Qu *et al.*, Evaluation of MCF10A as a Reliable Model for Normal Human Mammary Epithelial Cells, *PLoS ONE*, vol. 10, 2015 (cit. on p. 29).

- [36] H. D. Soule *et al.*, Isolation and Characterization of a Spontaneously Immortalized Human Breast Epithelial Cell Line, MCF-10, *Cancer Research*, vol. 50, pp. 6075–6086, 1990 (cit. on p. 30).
- [37] L. A. Pardo *et al.*, Oncogenic potential of EAG K⁺ channels, *The EMBO Journal*, vol. 18, pp. 5540–5547, 1999 (cit. on p. 30).
- [38] K. Lansu and S. Gentile, Potassium channel activation inhibits proliferation of breast cancer cells by activating a senescence program, *Cell Death and Disease*, vol. 4, 2013 (cit. on p. 30).
- [39] H. Wang *et al.*, HERG K⁺ Channel, a Regulator of Tumor Cell Apoptosis and Proliferation, *CANCER RESEARCH*, vol. 62, pp. 4843–4848, 2002 (cit. on p. 30).
- [40] A. Arcangeli *et al.*, A novel inward-rectifying K⁺ current with a cell-cycle dependence governs the resting potential of mammalian neuroblastoma cells. *The Journal of Physiology*, vol. 489, pp. 455–471, 1995 (cit. on p. 31).
- [41] W. F. Wonderlin *et al.*, Changes in Membrane Potential During the Progression of MCF-7 Human Mammary Tumor Cells Through the Cell Cycle, *Journal of Cellular Physiology*, vol. 165, pp. 177–185, 1995 (cit. on pp. 33, 34).
- [42] H. Ouadid-Ahidouch *et al.*, Changes in the K⁺ Current-density of MCF-7 Cells During Progression Through the Cell Cycle: Possible Involvement of a h-ether.a-gogo K⁺ Channel, *Receptors and Channels*, vol. 7, pp. 345–356, 2001 (cit. on pp. 33–35, 53, 65, 66).
- [43] S. Berzingi *et al.*, Altering bioelectricity on inhibition of human breast cancer cells, *Cancer Cell International*, vol. 16, 2016 (cit. on pp. 33–35).
- [44] H. Ouadid-Ahidouch *et al.*, Functional and molecular identification of intermediate-conductance Ca²⁺-activated K⁺ channels in breast cancer cells: Association with cell cycle progression, *Am J Physiol Cell Physiol*, vol. 287, pp. 125–134, 2004 (cit. on pp. 34, 108).
- [45] M. Abdul *et al.*, Activity of Potassium Channel-blockers in Breast Cancer, *Anticancer Research*, vol. 23, pp. 3347–3352, 2003 (cit. on p. 35).

- [46] K. A. Woodfork *et al.*, Inhibition of ATP-Sensitive Potassium Channels Causes Reversible Cell-Cycle Arrest of Human Breast Cancer Cells in Tissue Culture, *Journal of Cellular Physiology*, vol. 162, pp. 163–171, 1995 (cit. on pp. 35, 107).
- [47] G. A. Gutman *et al.*, International Union of Pharmacology. LIII. Nomenclature and Molecular Relationships of Voltage-Gated Potassium Channels, *Pharmacological Reviews*, vol. 57, pp. 473–508, 2005 (cit. on pp. 35, 39, 53, 61, 64–66).
- [48] H. Ouadid-Ahidouch *et al.*, KV1.1 K⁺ Channels Identification in Human Breast Carcinoma Cells: Involvement in Cell Proliferation, *Biochemical and Biophysical Research Communications*, vol. 278, pp. 272–277, 2000 (cit. on pp. 35, 36, 52, 53, 64, 65, 85, 94).
- [49] J. Roy *et al.*, Pharmacological separation of hEAG and hERG K⁺ channel function in the human mammary carcinoma cell line MCF-7, *Oncology Reports*, vol. 19, pp. 1511–1516, 2008 (cit. on pp. 35, 65, 66, 85).
- [50] J. Liu *et al.*, Expression of KCNA5 Protein in Human Mammary Epithelial Cell Line Associated with Caveolin-1, *The Journal of Membrane Biology*, vol. 249, pp. 449–457, 2016 (cit. on pp. 35, 36, 66, 94).
- [51] F. Collman, *abfload.m*, matlabcentral/fileexchange/22114-fcollman-abfload, 2022 (cit. on p. 40).
- [52] D. Sterratt *et al.*, *Principles of Computational Modelling in Neuroscience*. Cambridge University Press, 2011 (cit. on pp. 42, 43, 87).
- [53] S. Langthaler *et al.*, “Modeling of ion channels – A side by side comparison between Hodgkin Huxley and Hidden Markov approach of Kv1.1,” 2021 (cit. on pp. 42, 56, 86, 88).
- [54] S. Langthaler *et al.*, A549 in-silico 1.0: A first computational model to simulate cell cycle dependent ion current modulation in the human lung adenocarcinoma, *PLoS Computational Biology*, vol. 17, 2021 (cit. on pp. 42, 44–47, 49, 50, 52, 94).
- [55] D. Linaro and M. Giugliano, Markov Models of Ion Channels, D. Jaeger and R. Jung, *Encyclopedia of Computational Neuroscience*, Springer, New York, 2014 (cit. on pp. 43–45).

- [56] A. Destexhe and J. R. Huguenard, Modeling Voltage-Dependent Channels, *E. D. Schutter, Computational Modeling Methods for Neuroscientists*, MIT Press, pp. 107–138, 2009 (cit. on pp. 43, 46).
- [57] R. Mazhari *et al.*, Molecular Interactions Between Two Long-QT Syndrome Gene Products, HERG and KCNE2, Rationalized by In Vitro and In Silico Analysis, *Circulation Research*, vol. 89, pp. 33–38, 2001 (cit. on pp. 44, 45, 63, 68).
- [58] A. Salari *et al.*, Modeling the Kinetic Mechanisms of Voltage-Gated Ion Channels, *A. Korngreen, Advanced Patch-Clamp Analysis for Neuroscientists*, Springer, New York, pp. 267–304, 2016 (cit. on p. 45).
- [59] G. Schratter *et al.*, GIRK1 triggers multiple cancer-related pathways in the benign mammary epithelial cell line MCF10A, *Scientific Reports*, vol. 9, 2019 (cit. on pp. 47, 48, 110).
- [60] S. M. Mikki and A. A. Kishk, *Particle Swarm Optimization: A Physics-Based Approach*. Springer, Switzerland, 2022 (cit. on p. 52).
- [61] J. Tytgat *et al.*, Effect of fluoxetine on a neuronal, voltage-dependent potassium channel (Kv1.1), *British Journal of Pharmacology*, vol. 122, pp. 1417–1424, 1997 (cit. on p. 56).
- [62] I. Watanabe *et al.*, Glycosylation affects rat Kv1.1 potassium channel gating by a combined surface potential and cooperative subunit interaction mechanism, *Journal of Physiology*, vol. 550, pp. 51–66, 2003 (cit. on pp. 56, 57).
- [63] I. Michaelievski *et al.*, Interaction of syntaxin with a single Kv1.1 channel: a possible mechanism for modulating neuronal excitability, *Pflügers Archiv - European Journal of Physiology*, vol. 454, pp. 477–494, 2007 (cit. on p. 56).
- [64] R. Ågren *et al.*, Closed and open state dependent block of potassium channels cause opposing effects on excitability – a computational approach, *Scientific Reports*, vol. 9, 2019 (cit. on p. 56).
- [65] S. Langthaler *et al.*, Ion Channel Modeling beyond State of the Art: A Comparison with a System Theory-Based Model of the Shaker-Related Voltage-Gated Potassium Channel Kv1.1, *Cells*, vol. 11, 2022 (cit. on pp. 56, 57, 68, 88).

- [66] S. J. Goodchild *et al.*, Basis for allosteric open-state stabilization of voltage-gated potassium channels by intracellular cations, *Journal of General Physiology*, vol. 140, pp. 495–511, 2012 (cit. on pp. 57, 58, 68).
- [67] R. Ranjan *et al.*, A Kinetic Map of the Homomeric Voltage-Gated Potassium Channel (Kv) Family, *Frontiers in Cellular Neuroscience*, vol. 13, 2019 (cit. on pp. 58, 88, 89).
- [68] I. G. Ishida *et al.*, Voltage-dependent gating and gating charge measurements in the Kv1.2 potassium channel, *Journal of General Physiology*, 2015 (cit. on p. 58).
- [69] *IUPHAR/BPS Guide to Pharmacology*, accessed on 26.11.2022. [Online]. Available: www.guidetopharmacology.org (cit. on pp. 58, 62).
- [70] P. Hou *et al.*, Physiological Role of Kv1.3 Channel in T Lymphocyte Cell Investigated Quantitatively by Kinetic Modeling, *PLoS ONE*, vol. 9, 2014 (cit. on pp. 59, 68).
- [71] S. Grissmer *et al.*, Expression and chromosomal localization of a lymphocyte K⁺ channel gene, *Proceedings of the National Academy of Sciences*, vol. 87, pp. 9411–9415, 1990 (cit. on p. 59).
- [72] J. Almquist *et al.*, Modeling the Effect of Kv1.5 Block on the Canine Action Potential, *Biophysical Journal*, vol. 99, pp. 2726–2736, 2010 (cit. on p. 59).
- [73] N. Ellinwood *et al.*, Revealing kinetics and state-dependent binding properties of IKur-targeting drugs that maximize atrial fibrillation selectivity, *Chaos: An Interdisciplinary Journal of Nonlinear Science*, vol. 27, 2017 (cit. on pp. 60, 68).
- [74] E. Honoré *et al.*, External blockade of the major cardiac delayed-rectifier K⁺ channel (Kv1.5) by polyunsaturated fatty acids, *Proceedings of the National Academy of Sciences*, vol. 91, pp. 1937–1944, 1994 (cit. on p. 60).
- [75] M. Pusch *et al.*, Activation and Inactivation of Homomeric KvLQT1 Potassium Channels, *Biophysical Journal*, vol. 75, pp. 785–792, 1998 (cit. on pp. 60, 61, 68).
- [76] P. Hou *et al.*, Inactivation of KCNQ1 potassium channels reveals dynamic coupling between voltage sensing and pore opening, *Nature Communications*, vol. 8, 2017 (cit. on pp. 60, 61).

- [77] V. Garg *et al.*, Tuning of EAG K⁺ channel inactivation: Molecular determinants of amplification by mutations and a small molecule, *Journal of General Physiology*, vol. 140, pp. 307–324, Sep. 2012 (cit. on pp. 61, 62, 68).
- [78] G. C. L. Bett *et al.*, Models of HERG Gating, *Biophysical Journal*, vol. 101, pp. 631–642, 2011 (cit. on pp. 62, 63).
- [79] J. I. Vandenberg *et al.*, HERG K⁺ channels: Structure, function, and clinical significance, *Physiological Reviews*, vol. 92, pp. 1393–1478, 2012 (cit. on p. 62).
- [80] J. Kiehn *et al.*, Pathways of HERG inactivation, *American Journal of Physiology-Heart and Circulatory Physiology*, vol. 277, H199–H210, 1999 (cit. on pp. 62, 63).
- [81] S. Wang *et al.*, A quantitative analysis of the activation and inactivation kinetics of HERG expressed in *Xenopus* oocytes, *The Journal of Physiology*, vol. 502, pp. 45–60, 1997 (cit. on p. 63).
- [82] J. Kiehn *et al.*, Molecular Physiology and Pharmacology of HERG, *Circulation*, vol. 94, pp. 2572–2579, 1996 (cit. on p. 63).
- [83] J. Liu *et al.*, Expression and properties of potassium channels in human mammary epithelial cell line MCF10A and its possible role in proliferation, *Acta Physiologica Sinica*, 2010 (cit. on pp. 64, 66, 86).
- [84] B. L. vanTol *et al.*, Contribution of KCNQ1 to the regulatory volume decrease in the human mammary epithelial cell line MCF-7, *Am J Physiol Cell Physiol*, vol. 293, pp. C1010–C1019, 2007 (cit. on pp. 65, 85).
- [85] S.-z. Chen *et al.*, HERG K⁺ channel expression-related chemosensitivity in cancer cells and its modulation by erythromycin, *Cancer Chemotherapy and Pharmacology*, vol. 56, pp. 212–220, 2005 (cit. on p. 66).
- [86] *Channelpedia*, *Blue Brain Project (EPFL) 2005-2022, Switzerland*, accessed on 26.11.2022. [Online]. Available: <https://channelpedia.epfl.ch/> (cit. on p. 67).
- [87] M. Oeggerli *et al.*, Role of KCNMA1 in Breast Cancer, *PLoS ONE*, vol. 7, 2012 (cit. on pp. 94, 108).

- [88] P. Zhang *et al.*, Inhibition of SK4 Potassium Channels Suppresses Cell Proliferation, Migration and the Epithelial-Mesenchymal Transition in Triple-Negative Breast Cancer Cells, *PLoS ONE*, vol. 11, 2016 (cit. on pp. 94, 108).
- [89] E. Klimatcheva and W. F. Wonderlin, An ATP-Sensitive K⁺ Current that Regulates Progression Through Early G₁ Phase of the Cell Cycle in MCF-7 Human Breast Cancer Cells, *Journal of Membrane Biology*, vol. 171, pp. 35–46, 1999 (cit. on p. 108).
- [90] H. Ouadid-Ahidouch *et al.*, Cell-cycle-dependent expression of the large Ca²⁺-activated K⁺ channels in breast cancer cells, *Biochemical and Biophysical Research Communications*, vol. 316, pp. 244–251, 2004 (cit. on p. 108).
- [91] G. Coiret *et al.*, 17-beta-Estradiol activates maxi-K channels through a non-genomic pathway in human breast cancer cells, *FEBS Letters*, vol. 579, pp. 2995–3000, 2005 (cit. on p. 109).
- [92] S. P. Fraser *et al.*, Voltage-Gated Sodium Channel Expression and Potentiation of Human Breast Cancer Metastasis, *Clinical Cancer Research*, vol. 11, pp. 5381–5389, 2005 (cit. on p. 109).
- [93] F. H. Mohammed *et al.*, Blockade of voltage-gated sodium channels inhibits invasion of endocrine-resistant breast cancer cells, *International Journal of Oncology*, vol. 48, pp. 73–83, 2015 (cit. on p. 109).
- [94] J. T. Taylor *et al.*, Selective blockade of T-type Ca²⁺ channels suppresses human breast cancer cell proliferation, *Cancer Letters*, vol. 267, pp. 116–124, 2008 (cit. on p. 109).
- [95] J. T. Taylor *et al.*, Calcium signaling and T-type calcium channels in cancer cell cycling, *World Journal of Gastroenterology*, vol. 14, pp. 4984–4991, 2008 (cit. on p. 109).
- [96] T. Ohkubo and J. Yamazaki, T-type voltage-activated calcium channel Cav3.1, but not Cav3.2, is involved in the inhibition of proliferation and apoptosis in MCF-7 human breast cancer cells, *International Journal of Oncology*, vol. 41, pp. 267–275, 2012 (cit. on p. 110).
- [97] A. Guilbert *et al.*, Evidence that TRPM7 is required for breast cancer cell proliferation, *American Journal of Physiology-Cell Physiology*, vol. 297, pp. C493–C502, 2009 (cit. on p. 110).

- [98] C. Li *et al.*, Piezo1 forms mechanosensitive ion channels in the human MCF-7 breast cancer cell line, *Scientific Reports*, vol. 5, 2015 (cit. on p. 110).
- [99] Y.-W. Huang *et al.*, Chloride channel involved in the regulation of curcumin-induced apoptosis of human breast cancer cells, *Asian Pacific Journal of Tropical Medicine*, vol. 11, pp. 240–244, 2018 (cit. on p. 110).

7 Appendix

7.1 Voltage Pulse Protocol

Time	Value
-	ms
t_0	0
t_1	30
t_P	80
t_2	1600
t_3	1700
t_E	2000

Table 8: Timing of voltage pulse protocol

V_C	Value
-	mV
V_0	0
V_1	-60
V_P	-120, -110,..., 110
V_2	-60
V_3	0

Table 9: Clamping potentials of voltage pulse protocol

7.2 Further Ion Channels in MCF-7

7.2.1 Potassium Channels

Based on experiments with different channel inhibitors and overlapping target channels it was shown that MCF-7 cells can be arrested in Go/G1-phase by quinidine, glibenclamide and linogiride. By using an exclusion principle on targeted channels it was concluded that MCF-7 cells not only functionally express ATP-sensitive potassium channels (K_{ATP}) but also get arrested in Go/G1-phase by specifically blocking these channels using the mentioned antagonists. [46]

A further study supported these findings by clustering the current of a whole-cell patch-clamp experiment. The ATP-sensitive current was modelled as a linear, hyperpolarizing potassium current, required for progression through G₁ phase and sensitive to intracellular ATP and Ca²⁺. [89]

It was reported a long time ago that MCF-7 cells express Ca²⁺-activated potassium channels and that the expression levels of these channels correlate with cell growth [Wegman et al. A 23-pS calcium-activated potassium channel in MCF-7 human breast carcinoma cells: an apparent correlation of channel incidence with the rate of cell proliferation. 1991 quoted in 44].

One study found a Ca²⁺-sensitive potassium channel with functional properties similar to the hIK₁ channel. This hIK₁-like channel (term used in the publication) showed an mRNA expression profile that correlates with cell cycle progression in MCF-7 cells. Currents maintained by these specific channels were also shown to be closely related to cell cycle progression. Blocking the hIK₁-like channel with CLT resulted in a significant inhibition of proliferation. Econazole (blocker of Ca²⁺-activated intermediate potassium channels) resulted in a slight inhibition in proliferation. [44]

This intermediate conductance calcium-activated hIK₁-like channel might be equivalent to the SK₄ channel and another publication can be correspondingly linked to this by assuming so. In harmony with the stated points, expressions of both channel protein and mRNA of SK₄ channels were explicitly confirmed in MCF-7 cells [88].

Another study determined the cell cycle dependent expression of BK potassium channels in MCF-7 cells. As experimentally determined, the expression of this channel was highly dependent on the cell cycle and reached a maximum in G₁-phase. In harmony with these observations, MCF-7 cells showed a relatively high, r-IbTX-sensitive (potent blocker of BK channel) outward current at the end of G₁-phase. [90]

Another research group identified mRNA of KCNMA₁ in MCF-7 as well, confirming the results of previous publications. It has also been elaborated that BK currents are present and that knocking down the KCNMA₁ gene reduced proliferation of MCF-7 cells. Blocking BK channels using paxilline reduced proliferation significantly as well. [87]

Based on experiments using channel blockers and by performing an exclusion principle it could be determined that the steroid hormone 17- β -Estradiol (E2) is able to activate BK (named maxi-K in the publication) channels. Furthermore, E2 was also shown to be capable of increasing proliferation of MCF-7 cells. [91]

7.2.2 Sodium Channels

A previous study suggested the absence of sodium currents in MCF-7 as whole-cell patch-clamp experiments in corresponding measurement arrangements showed no significant inward currents for membrane potentials between -60 mV and +60 mV. In contrast, mRNA expressions of subunits for Na_V1.5, Na_V1.6 and Na_V1.7 were detected in MCF-7 cells. Compared to the concerning mRNA expressions in MDA-MB-231, the overall expression levels in MCF-7 were reported to be low. [92]

Above mentioned findings were confirmed by another study, reporting the absence of Na_V-currents. In this study, the cells were held at -120 mV and depolarized in a range from -80 mV to +30 mV. [93]

7.2.3 Calcium Channels

It was reported that MCF-7 cells express two T-type Ca²⁺-channels. Western blot analysis revealed the presence of the corresponding proteins α_{1G} and α_{1H} . The expression of the concerning mRNA was determined as well. The channel blocker NNC-55-0396 has been shown to be capable of significantly decreasing T-type calcium currents in MCF-7. [94]

These findings are outstanding, since non-excitabile tissues usually do not express Ca_V-channels [95]. The corresponding genes of the voltage-gated calcium channels, reported by [94], were assumed to be CACNA1G (Ca_V3.1) and CACNA1H (Ca_V3.2) using the nomenclature defined in [10] for guidance on this. By assuming this to be correct, a subsequent study revealed further correlations between these channels and MCF-7 cells.

For example, silencing the $\text{Ca}_V3.1$ gene significantly stimulated cell proliferation, while silencing the $\text{Ca}_V3.2$ gene did not show any effects on proliferation at all. Blocking $\text{Ca}_V3.1$ with ProTx-I (relatively selective) stimulated cell proliferation and overexpression of $\text{Ca}_V3.1$ was shown to enhance apoptosis. [96]

7.2.4 Others

RT-PCR from a previous study showed that TRPM6 and TRPM7 mRNA transcripts are expressed in MCF-7 cells [97].

TRPM7 is permeable for Ca^{2+} and was suggested to contribute to the Ca^{2+} homeostasis regulation, thereby influencing MCF-7 cell growth. Silencing TRPM7 in MCF-7 cells resulted in enhanced cell death in the observed colony. Cell growth was additionally shown to be obstructed when the external calcium concentration was lowered. [97]

A study from 2015 reported that mechanosensitive channels were expressed in patches of MCF-7 cells. Channel activation could be observed when mechanical stress was applied. The channels were shown to be activated at negative pressures and Piezo1 was suggested to be a component of them. [98]

Piezo1 denotes a mechanically activated ion channel and refers to both channel name and encoding gene (PIEZO1) [10].

Serving as an additional annotation, a study from 2018 investigated chloride currents in MCF-7 cells in context with curcumin [99]. Furthermore, a publication from 2019 reported mRNA expression of GIRK1-channels in MCF-7, but subsequent Western blotting was not able to reliably detect the corresponding protein [59].